Transport Dynamics and Fluctuations in Active Bulk Heterojunction Polymer Solar Cells

A Thesis

Submitted for the Degree of

DOCTOR OF PHILOSOPHY

by

MONOJIT BAG

CHEMISTRY AND PHYSICS OF MATERIAL UNIT
JAWAHARLAL NEHRU CENTRE FOR ADVANCED SCIENTIFIC RESEARCH
(A Deemed University)
Bangalore – 560 064

MAY 2011

This thesis is dedicated to my parents

DECLARATION

I hereby declare that the matter embodied in the thesis entitled "**Transport Dynamics and Fluctuations in Active Bulk Heterojunction Polymer Solar Cells**" is the result of investigations carried out by me at the Molecular Electronics Laboratory, Jawaharlal Nehru Centre for Advanced Scientific Research, Bangalore, India under the supervision of Prof. K. S. Narayan and it has not been submitted elsewhere for the award of any degree or diploma.

In keeping with the general practice in reporting scientific observations, due acknowledgment has been made whenever the work described is based on the findings of other investigators.

Monojit Bag

CERTIFICATE

I hereby certify that the matter embodied in this thesis entitled "**Transport Dynamics and Fluctuations in Active Bulk Heterojunction Polymer Solar Cells**" has been carried out by Mr. Monojit Bag at the Molecular Electronics Laboratory, Jawaharlal Nehru Centre for Advanced Scientific Research, Bangalore, India under my supervision and it has not been submitted elsewhere for the award of any degree or diploma.

Prof. K. S. Narayan
(Research Supervisor)

Acknowledgments

I express my heartiest gratitude to my research supervisor Prof. K. S. Narayan, for suggesting me such challenging and interesting research problems and also extending his invaluable guidance, immense support and constant encouragement throughout my research career. His friendly attitude allowed me to work freely and think of the problem in a different way. His valuable discussion helped me a lot to understand things much better and in a simpler way. His time management and passion for science will be an everlasting inspiration for me. I am also thankful to his family members for their hospitality and support during my stay in JNCASR.

I would like to thank Dr. N. S. Vidhyadhiraja for his valuable discussion and suggestions.

Its my privilege to thank my course instructors, Prof. Chandrabhas Narayana, Prof. S. K. Pati, Prof. S. Balasubramanian, Prof. Umesh Waghmare, Prof. G. U. Kulkarni, Dr. A. Sundareshan, Dr. M. Eswarmoorthy, Prof. S. Ranganathan and all other TSU and CPMU faculties for allowing me to discuss whenever I needed.

I am thankful to the academic and administrative staff for financial and technical support during my stay in JNCASR. I also thank CSIR for JRF & SRF fellowship.

I am thankful to my lab members for their support and encouragement. I would

like to acknowledge my past lab members, Dr. Dinesh Kabra for his valuable advices, Dr. Dhritiman Gupta for his constant guidance, Dr. Arun N, Shruti, Dr. Manohar Rao, Jasmeet, Hemant and Dr. Balraju. I thank my present lab members; Sachi for his support during my tough time, Vini for working together on various problems, Anshuman for sharing all his passion and knowledge of guitar and keyboard, Ravi, Satya, Arun, Vijay, Nishit, Prashant and Dr. Srinidhi for helping me out on various aspects.

I would like to thank all my friends those who are in JNCASR as well as outside for their well wishes.

Finally I am forever indebted to my parents, sister and brothers for their love, affection, support and encouragement all through the years.

Publications

- *Origin of Photocurrent Fluctuation in Bulk Hetero-junction polymer Solar Cells.* **M. Bag**, N. S. Vidhyadhiraja and K. S. Narayan, (Manuscript under preperation) (2011).

- *Studies of long-lived photogenerated carriers in low band gap polymer photodiodes.* **M. Bag** and K. S. Narayan, (Manuscript under preperation) (2011).

- *Universality in Intensity Modulated Photocurrent in Bulk-Heterojunction Polymer Solar Cells.* **M. Bag** and K. S. Narayan, *Phys. Rev. B*, **82**, 075308, (2010).

- *Deformation of metallic liquid drop by electric field foe contacts in molecular - organic electronics.* **M. Bag**, D. Gupta, N. Arun and K. S. Narayan, *Proc. R. Soc. A*, **465**, 1799, (2009).

- *Single Pixel Active Polymer Device as a Tri-color Sensor with Signals Mimicking the Retinal Cone Cells.* Vini Gautam, **Monojit Bag** and K. S. Narayan, (submitted) (2011).

- *Dynamics of Bulk Polymer Heterostructure/Electrolyte Devices.* Vini Gautam, **Monojit Bag** and K. S. Narayan, *J. of Phys. Chem. Lett.* **1**, 3227 (2010).

- *Area dependent efficiency of organic solar cells.* D. Gupta, **M. Bag** and K. S. Narayan, *Appl. Phys. Lett.* **93**, 163301 (2008).

- *Correlating reduced fill factor in polymer solar cells to contact effects.* D. Gupta, **M. Bag** and K. S. Narayan, *Appl. Phys. Lett.* **92**, 093301 (2008).

Patent: Artificial Retina Device, by K. S. Narayan, Vini Gautam and **Monojit Bag.** **Patent Application. PCT/IB2010/002170**

Contents

Preface

Bulk-heterojuction polymer solar cells (BHJ-PSCs) are promising alternatives for conventional inorganic solar cells with relatively low manufacturing complexity. The network morphology and the optimized gradients of the appropriate phases at the electrodes in these BHJ-PSCs have been observed to play an important role in determining the properties of these devices. Studies on dynamics of the electrical transport of the photo-generated carriers are valuable to understand the processes prevailing in the system. The initial part of the thesis deals with the response of BHJ-PSCs to intensity modulated light sources. A universal feature in the intensity modulated photocurrent spectroscopy (IMPS) is observed in these BHJ-PSCs, in the form of a photocurrent peak in the frequency range of 5 - 10 kHz. A simplistic model arising from the macroscopic circuit parameters and microscopic processes is used to describe the photocurrent feature. Additional experiments were carried out to understand the effect of temperature, composition, efficiency, background CW light and the intensity of the modulated light source. Intensity modulated photocurrent measurements were also carried out on dye sensitized solar cells (DSSCs) and bi-layer polymer solar cells, where the IMPS feature was absent in the 5 - 10 KHz range. The origin of photo-current peak feature is attributed to the characteristic combination of correlated fundamental processes occurring over multiple time scales.

Following the frequency dependent studies, the noise patterns of the BHJ-PSCs

in active working condition were probed. The complex sequence of generation, separation and transport of the photo-generated carriers manifests in the form of characteristic noise signal. The power spectral density (PSD) of the short circuit current fluctuation takes a gaussian form in the 10 kHz to 90 kHz frequency regime. The noise studies were carried out under different experimental conditions; namely temperature, light intensity and efficiency of the devices. In general, the magnitude of the photo-current fluctuation reduces with decreasing temperature. The photo-current fluctuation amplitude is observed to increase with increasing light intensity. The origin of the photo-current fluctuation is attributed to the density of trap states present in the device.

Low band gap polymer are very promising alternatives for high efficiency solar cell where significant photocurrent is observed even at NIR regime. This opens up an additional avenue for polymer photo-detector application in telecommunication systems. The device characterization is done under different temperature and different reverse bias condition in NIR spectral range. The responsivity and switching speed of the detector increase as magnitude of the reverse bias increases. The devices were also tested under CW background light with variable intensity.

Last part of the thesis deals with Electrohydrodynamic instability of a conducting liquid surface in a strong electric field (EF) and its application in molecular and organic electronics. The deformation of conducting liquid surfaces using low temperature metal-alloys opens up options for controlled contact formation with fundamental implications in studying electrical transport in soft systems and applications in printable electronics. Polymer based solar cells and light emitting diodes are fabricated with these low melting temperature alloy cathodes. These device performances carried out in ambient condition are comparable to the devices fabricated by conventional physical-vapor deposition method.

List of Figures

List of Tables

List of abbreviation

Bulk heterojunction	BHJ
Charge transfer complex	CTC
Circuit transfer function	CTF
Density of states	DOS
Dye sensitized solar cells	DSSCs
Electric field	EF
External quantum efficiency	EQE
Fast Fourier transform	FFT
Gaussian disorder model	GDM
Highest occupied Molecular orbital	HOMO
Indium tin oxide	ITO
Intensity modulated photocurrent spectroscopy	IMPS
Kinetic Monte Carlo	KMC
Lowest unoccupied molecular orbital	LUMO
Near infra red	NIR
Noise equivalent power	NEP
Occupied density of states	ODOS
Polymer light emitting diode	PLED
Polymer solar cells	PSCs
Power spectral density	PSD
Scher and Montroll	SM
Transparent conducting oxide	TCO

SECTION 1

Introduction

1.1 Historical background

Abundant and economical energy in its different forms is the life blood of modern civilizations. Natural gas, coal and oil provides almost 85% of the total energy consumption. However world's leading geologists have suggested that the consumption of oil has already reached its peak [1]. As the energy demand is increasing day by day (13 terawatts (TW) continuous world energy consumption in 2005 to 30 TW projected demand in 2050), the depletion of oil and other natural resources will create a gap of 17 -20 TW. This is a wakeup call to the global civilization to think of an alternative, renewable energy resources to make up the demand. Solar energy source is a clean alternative that can meet some of these challenges. Scaling up the solar energy efforts is needed to make it a viable alternative.

Solar energy: Facts & Trivia

- 120,000 TW global theoretical potential.
- 600 TW available incident solar power.
- 60 TW technically feasible generated power based on 10% conversion efficiency.
- 20 TW based on usage of just 0.16% of global land area and 10% conversion efficiency.

Since the early discovery of the photoelectric effect by Becquerel, silicon based photovoltaic cells represent the most efficient devices to harvest solar energy. In

recent years the development of new inorganic materials with a low energy band gap which encompasses a large part of the solar spectra shows a promise towards high efficiency solar cells. State-of-the-art inorganic solar cells have a record power conversion efficiency of close to 39% [2], whereas commercially available solar panels have significantly lower efficiency of around 15-20%. Hence the cost per unit power ($/W) [3] is much higher compared to the conventional energy sources. The main challenge in the utility of solar cells still is the lack of cost-effective, large-area fabrication methods. In this direction, the choice of polymers and organics as active materials in large area solar cell offers huge potential. Solar cells based on thin polymer films are particularly attractive because of their low cost solution process, mechanical flexibility and roll-to-roll printing on a large area substrate. Additionally their material properties can be tailored by modifying the chemical structures, resulting in greater opportunities than traditional technologies allow.

The field of organic photovoltaics can be dated to as early as 1959 when Kallmann and Pope proposed and demonstrated that anthracene can be used to make a solar cell [4]. The first generation organic solar cell proposed by Kallmann was so-called homojunction solar cell based on single organic materials. The open circuit voltage recorded was only 0.2 V and the current density was low. Relatively high binding energy (200 - 400 meV) [5–7] of coulombically bound electron-hole pair (exciton) in the low dielectric constant (2 - 4) organic materials were the main drawbacks for the low efficiency solar cell. In 1986, C. W. Tang and Kodak demonstrated a solar cell based on two layers of conjugated organic materials [8]. One of them is electron donating (donor) and other is electron accepting (acceptor) material forming a heterojunction at the bilayer interface. The photogenerated exciton then can easily get dissociated to free carriers at the bilayer interface due to built-in field. Relatively low interfacial area of donor-acceptor polymer leads to lower

generation of charge carriers. Hence the efficiency of these organic based solar cells were also very low. A major breakthrough in the field arrived only after a decade later when Alan. J. Heeger and collaborators came up with a concept and demonstrated that an interpenetrating network of donor-acceptor materials increases the interfacial area between donor and acceptor molecules. This type of device with multitude of hetero-structures is termed as Bulk-hetero-junction (BHJ) [9]. The efficiency reached $\sim$ 5% within a few years [10–12]. These solution processable polymer based devices can be spin casted, drop casted or printed on glass, plastic or any other flexible substrates especially for large area applications. Polymer based devices are also used in photo-detectors [13], color-sensors [14], multicolor display, light emitting FETs and all polymer integrated circuits [15]. These trends in organic electronics are rapidly growing and complement the existing inorganic and Silicon technology in offering solutions to various applications in display and sensor technologies.

Conjugated polymers are fundamentally different to saturated insulating polymers in terms of electronic properties. Conjugated means alternative double bonds ($\sigma + \pi$) and single bonds (σ) in the polymer backbone. The simplest conjugated polymer is synthesized from acetylene $(CH)_x$ known as polyacetylene (PA) [16]. The polymer backbone may have two conformational isomers, armchair configuration (cis-PA) or zig-zag configuration (trans-PA) and the electronic properties differ significantly. In 'trans' configuration delocalized π-electrons along the backbone of the polymer chain forms a quasi 1D metal. However, the non-uniform spacing between the successive atoms leads to a dimerization. This dimerization gets stabilized by opening up an energy gap (in the visible range from 1.4 eV to 3.5 eV) at the Fermi surface by lowering the energy of the occupied states. Polymer semiconductors are widely used materials in the field of organic electronics.

In general, polymers are structurally and electronically disordered materials. Hence, charge conductivity in polymer materials is significantly lower than the inorganic materials. In order to increase the conductivity, excess number of quasi particles in the polymer backbone need to be generated. This can be achieved by doping, a chemical redox reaction that involves partial addition or removal of electrons from the conjugated backbone. There are mostly three ways to introduce the excess carriers in conjugated polymer backbone. (i) Chemical doping; an electron donating or electron withdrawing moiety is chemically attached to the backbone. Electronic structure of the polymer also gets modified by the chemically attached moiety. The band gap may increase or decrease depending on the type of functional group attached to the polymer backbone. (ii) Photogeneration; carriers are generated upon photoexcitation. This will be discussed in section 1.3.1 in more detail (iii) Carrier injection; depends on the polymer/electrode interface that can be a Schottky barrier or an ohmic contact. Photogenerated or the injected charge carriers can be transported through the disordered network. There is no unified framework to depict the charge transport mechanism upon introducing the excess carriers through disordered polymeric semiconductors. A brief summary of some existing models based on pristine polymers is mentioned in the next section. It is to be noted that only topics pertinent to the results in the thesis are included. The topics introduced are not comprehensive, but bring out the essential points needed in the discussion section of the thesis.

1.2 Charge carrier transport through disorder semiconductor

Organic semiconductors are highly disordered in nature. Unlike inorganic semiconductors, there are localized states in the band gap region and the transport is dominated by hopping of the charge carriers. In a broad sense, hopping is a phonon assisted quantum mechanical tunneling which depends on the energetic disorder as well as spatial disorder [17]. According to variable range hopping (VRH) charge carriers can hop upwards or downwards between two energetic states either by absorbing or emitting phonons respectively. Charge carriers can hop over larger distances with very low activation energies or they can hop to a nearest neighbor with very high activation energies. At low temperature, the probability of hopping over a large distance with low activation energy is higher than hopping over smaller distance with high activation energy. The temperature dependent carrier transport is dependent on the localized states as proposed by Mott [18] where the conductivity varies as $exp[-(T_0/T)]^{1/(1+d)}$. d is the device dimension. Characteristic temperature T_0 depends on the density of states (DOS) at the Fermi level and the localization length. Miller and Abraham [19] proposed another theory where the hopping rate between site i and j depends on two parameters: energetic barrier $(\varepsilon_j - \varepsilon_i)$ and distance (r_{ij}) as shown in the equation 1.1

$$\nu_{ij} = \nu_0 \exp\left(-2\gamma a \frac{r_{ij}}{a}\right) \times \begin{cases} exp\left(-\frac{\varepsilon_j - \varepsilon_i}{k_B T}\right) & \text{for } \varepsilon_j > \varepsilon_i, \\ 1 & \text{for } \varepsilon_j < \varepsilon_i \end{cases} \tag{1.1}$$

The frequency pre-factor ν_0 is called the attempt-to-hop frequency, r_{ij} is the jump distance between site i and j (normalized to the intersite distance a). $2\gamma a$ con-

trols the electronic coupling among the hopping sites through exchange interaction. There are numerous attempts to find out the DOS for disorder organic semiconductors [20, 21]. There are several models to explain the disorder in the system such as positional disorder described by Scher and Montroll (SM), but the most commonly used model is Gaussian Disorder Model (GDM) [22–24] where energetic disorder has also been considered in the transport model.

1.2.1 Scher and Montroll (SM) model

Polymeric semiconductors have many similarities with the amorphous inorganic semiconductor. Therefore SM model, when applied to disordered polymeric system, could explain many of the transient photocurrent features. The electrical transport properties of such materials depends on the carrier's average mobility (μ). A common method to measure μ from the photocurrent transient is time of flight (TOF) measurement [25] as shown in the figure 1.1. The TOF mobility measurement technique will be discussed briefly to correlate disordered transport to the transient photocurrent features observed in organic semiconductors.

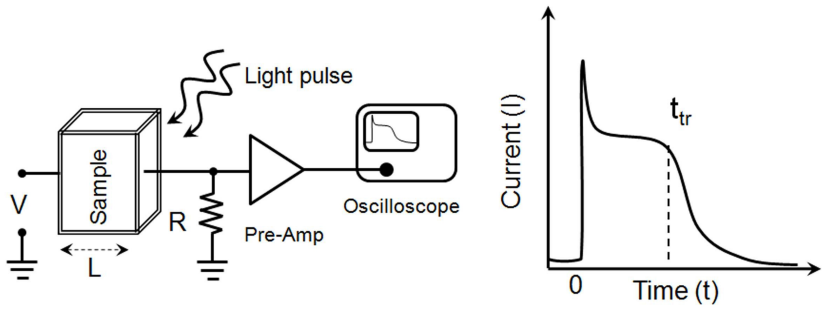

Figure 1.1: *(a) Experimental setup for the Time of Flight (TOF) mobility measurement. (b) Ideal transient photocurrent response.*

A thick film (thickness L of the order of μm) of the material is sandwiched

between two electrodes (one of them should be transparent). A sheet of charge carrier is generated at the front electrode by illuminating a short laser pulse. L should be such that $\alpha L >> 1$ where α is the absorption coefficient (cm^{-1}). The sheet of charge carriers then gets swept away towards counter electrode by a voltage pulse (V) that follows the light pulse. The resultant photocurrent transient shows a photocurrent 'spike' at the onset of light pulse due to the displacement current. This is followed by a steady state 'plateau', where the sheet of charge carriers moves uniformly under the electric field (V/L) and a long decay 'tail' indicating the charge carrier extraction at the electrode is observed. The transit time (t_{tr}) is defined as the onset of tail state as shown in the figure 1.1 and mobility is given by the equation 1.2

$$\mu = \frac{L^2}{t_{tr}V} \tag{1.2}$$

For a non-dispersive transport, t_{tr} is well defined. This happens due to the dominant contribution of the constant drift velocity of the carriers under constant electric field. However, the presence of delocalized states reduces the drift velocity of some of the carriers and hence transient photocurrent tends to become featureless. In 1975, H. Scher and E. W. Montroll [26] proposed a model for transport in a-As_2Se_3 as well as trinitrofluorenone-polyvinylecarbazoles to explain this anomaly. In a non-dispersive transport, the Gaussian charge packet remains Gaussian ($\psi(t) \sim e^{-t/\tau}$) till it reaches the electrode, whereas for a dispersive transport some of the photogenerated carriers get trapped in the localized states and others move non-uniformly. Scher and Montroll described this in terms of time-dependent random walk of the charge carriers in presence of an electric field. The time-dependence of random walk is governed by the hopping time distribution $\psi(t)$. The dispersion of the hopping time is proposed to follow inverse power law as given

by the equation 1.3.

$$I(t) \quad \sim \text{const} \times \begin{cases} t^{-(1-\alpha)} & \text{for } t/t_{tr} < 1 \\ t^{-(1+\alpha)} & \text{for } t/t_{tr} >> 1 \end{cases} \tag{1.3}$$

with $0 < \alpha < 1$ as a dispersion parameter. The assumption originated from the fact that there is a large distribution of hopping sites due to positional disorder. Hence the distribution of waiting time between two successive hopping is quite large. As a result, mean carrier velocity decreases with time as it gets separated from the peak which remains fixed at the point of origin. The distribution of mean carrier propagation can be characterized by two parameters: mean partial displacement and the peak position. In case of a Gaussian charge packet, $\sigma_x/\langle l \rangle = \text{const}$, $\sigma_x^2 = \langle (x - \langle x \rangle)^2 \rangle$ is the variance and $\langle l \rangle$ is the mean displacement. In case of a dispersive transport $\sigma_x/\langle l \rangle \approx t^{-(1+\alpha)}$. In order to extract t_{tr}, photocurrent transient can be plotted in a log-log scale as shown in figure 1.2. The transient photocurrent then

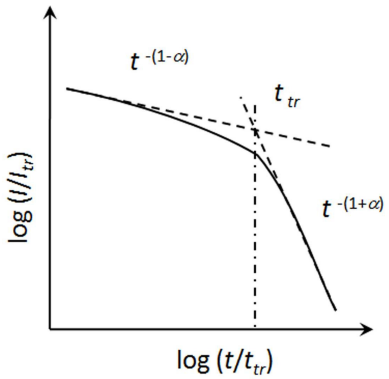

Figure 1.2: *Transient photocurrent response of a dispersive transport plotted in log-log plot. Intersection of the two asymptote represents the* t_{tr}

can be modeled as given by the equation 1.3. In the log-log plot the intersection of two slopes is the estimated t_{tr}. The plot can be temperature and field invariant if it

is normalized with the applied field (V/L) and t_{tr}. This invariance is designated as 'universality' by Scher and Montroll [26]. The 'universality' was first demonstrated quantitatively by Scharfe *et. al.* in their study on amorphous arsenic triselenide [27]. This is also experimentally observed by Bos *et. al.* in Polyvinylecarbazole [28].

In all the cases, inherent disorder in materials generally gives rise to dispersive transport. However SM model does not take into account the fluctuation in the site energy or the 'energetic disorder' and does not explain the temperature dependence of the dispersive transient photocurrent as observed in many disordered solids. Deviation from the 'universality' has been observed in many systems depending on the temperature variation [29, 30]. The 'tail' broadening parameter, W, (equation 1.4) of the TOF signals which is the measure of the degree of dispersion also revealed the interesting properties at different temperature. W is defined as,

$$W = \frac{t_{1/2} - t_0}{t_{1/2}} \tag{1.4}$$

where $t_{1/2}$ is the time for the transient photocurrent to decay to half of its plateau value and t_0 is the time defined by the intersection of the two slopes (asymptotes). Borsenberger *et. al.* related the dispersion W of a non-dispersive TOF signal to the energetic disorder parameter (σ_E/k_BT) of the material. The functional form of W on the film with a thickness L undergoes a characteristic change from $W \propto L^{-1/2}$ (at lower value of σ_E/k_BT) to $W =$ constant (at larger value of energetic disorder σ_E/k_BT >4). Experimentally, the constant behavior was observed at low temperature (<180 K) whereas at high temperature (room temperature) it follows inverse square root dependence [31]. This inconsistency prompted to think of another model for energy distribution like the Gaussian disorder model.

1.2.2 Gaussian disorder model (GDM)

The temperature dependent TOF photocurrent transient in molecular solid was explained by Bässler *et. al.* [22, 30, 32] using a model for charge transport using Gaussian distribution of localized states (figure 1.3). The energy of hopping sites was derived from the Gaussian distribution of standard deviation σ_E as shown in the equation 1.5

$$\rho(\varepsilon) = (2\pi\sigma_E^2)^{-1/2} exp\Big(-\frac{\varepsilon^2}{2\sigma_E^2}\Big) \tag{1.5}$$

The experimental value of energetic disorder σ_E lies between 70 - 150 meV

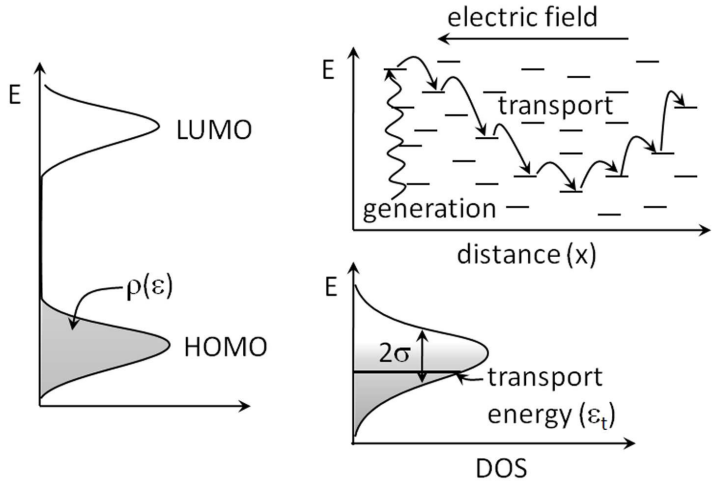

Figure 1.3: *Gaussian Density of States with a disorder parameter σ_E ranging between 70 - 150 meV. There is a characteristic energy level (ε_t) bellow which the states are localized and carrier has to hop upward to take part in the transport, also known as mobility edge.*

($\sigma_E/k_BT \sim 3-6$ at room temperature). Such disorder formalism is known as diagonal disorder. However, if site i interacts with the site j, the wave function overlap parameter $2\gamma a$ in the equation 1.1 takes a form of $\Gamma_{ij} = \Gamma_i + \Gamma_j$. The variance of Γ_{ij} is called the off-diagonal disorder. The energy required by carriers to participate in the transport (transport energy) is located at -$(5/9)\sigma_E^2/k_BT$ [22, 33].

This gives rise to temperature dependent mobility in the form of equation 1.6,

$$\mu(T) = \mu_0 exp\Big[-\Big(\frac{2\sigma_E}{3k_BT}\Big)^2\Big] \tag{1.6}$$

where μ_0 is the temperature independent zero field mobility. Under any applied field the electrostatic energy will reduce the activation barrier for charge transport. As a consequence mobility increases. The field and temperature dependent mobility of disorder system is given by the equation 1.7,

$$\mu(F,T) = \mu_0 exp\Big[-\Big(\frac{2\sigma_E}{3k_BT}\Big)^2\Big] \times exp[C_0(\sigma_E^2 - \Sigma^2)\sqrt{F}] \tag{1.7}$$

where C_0 is a numerical constant which depends on the material. At high electric field, mobility tends to saturate. In 1970 Pai *et. al.* [34] demonstrated that at high electric field, mobility of photogenerated holes in poly (N-vinylecarbazole) (PVK) can be explained by Poole-Frenkel effect [35].

$$\mu_h(F) = \mu_0 exp\Big(-\frac{\Delta}{k_BT}\Big) exp(\gamma\sqrt{F}) \tag{1.8}$$

In 1972 Gill proposed an empirical relation for the temperature dependence of γ

$$\gamma = B\Big(\frac{1}{k_BT} - \frac{1}{k_BT_0}\Big) \tag{1.9}$$

The constant $B = 2.7\times10^{-5} eV(V/m)^{-1/2}$ and $T_0 = 520$ - 660 K for PVK. Equation 1.9 also predicts that at $T > T_0$ the field dependence of mobility becomes negative.

The GDM could explain most of the temperature dependent transport measurement. The disorder concept relies on the fact that the transport of the charge carriers takes place in an empty DOS. If the bottom sates are filled, then the

occupied density of states (ODOS) changes and the activation energy decreases. This is consistent with the result that the FET mobility is much higher than TOF mobility (2-3 orders of magnitude) [36, 37]. It is demonstrated that the mobility is constant for a carrier density $< 10^{16}$ cm^{-3} and increases with a power law for density $> 10^{16}$ cm^{-3}. However, excess doping of charge may reduce the mobility again. Some of these concepts can be further modified and applied to the electrical transport processes in organic solar cell devices which are the central focus of this thesis report. The specific ideas, materials and different phenomena pertaining to organic solar cells are introduced in the next section.

1.3 Donor-Acceptor Polymer Solar Cells

State of the art solar cells based on conjugated polymers with appropriate band gap have been shown to exhibit high efficiency ($\sim 8\%$) [38–40]. These developments of polymer solar cells have resulted from a combination of optimized factors which include appropriate molecules, processing methods to yield desirable morphology, device architecture and encapsulation methods. An initial step in this cycle is the design and synthesis of macromolecules with large absorption or low band-gap semiconductor such as cyclopentadithiophene based PCPDTBT, Poly(N-alkyl-2,7-carbazole) derivative PCDTBT which has been shown to exhibit much higher external quantum efficiency (EQE) up to 900 nm. Tuning the highest occupied molecular orbital (HOMO) and lowest unoccupied molecular orbital (LUMO) of the donor and acceptor is also important in order to achieve an open circuit voltage as high as possible [41]. The other crucial device parameters of fill factor and current density are also known to depend on a variety of factors [42, 43]. A brief introduction to these various processes prevalent in BHJ-PSC is discussed in the

following sections. The processes described follows a chronological order beginning with the photoexcitation and exciton dissociation stages.

1.3.1 Photogeneration of charge carriers

The optically active donor component of the solar cells typically has a band gap of 1.4 eV to 3.5 eV and is the primary source for photocarriers. Upon photoexcitation, the photoexcited state has an 'exciton' character which consists of columbically bound singlet electron-hole pair. The dielectric constants of the polymer are low ($\epsilon_r \sim 2$ - 4) compared to inorganic semiconductors ($\epsilon_r \sim 12$). Hence, binding energy of Frenkel type excitons is 0.2 - 1 eV [44] depending of the materials and intra and inter-chain coupling. The coulomb radius is $r_c \sim 1$ nm as compared to inorganic counterpart where it is mostly Mott-Wannier excitons of $r_c > 10$ nm. These singlet exciton can dissociate at the donor acceptor (D-A) heterojunction of LUMO-LUMO offset more than 0.5 eV [45]. Singlet excitons can also give rise to triplet states by a non-radiative inter-system crossing (ISC) [46]. The transition from excited triplet states to ground state is spin forbidden [47, 48]. Hence excited triplet states do not dissociate to free carriers, rather thermally decay back to ground states. This transition is possible by increasing spin orbit coupling by doping the polymer matrix with heavy transition metal.

1.3.2 Exciton dissociation at the interface

The photogenerated excitons with reasonable binding energy ($> k_BT$ at room temperature) do not thermally dissociate. In order to increase the dissociation and promote charge separation, it was suggested that introductions of acceptor molecules in the donor matrix with appropriately positioned LUMO level can form

D-A heterojunction. Hence a typical organic solar cell consists of two types of materials know as Donor (p-type) and Acceptor (n-type) with an energy band offset 0.3 to 0.5 eV [45, 49]. Heterojunction can be classified into two types depending on relative position of HOMO and LUMO level of the materials at the interface, as shown in the figure 1.4. In case of type I heterojunction, the HOMO-LUMO of

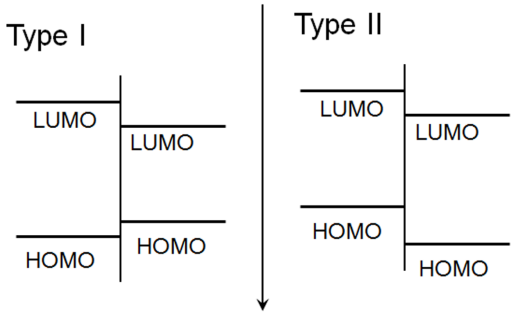

Figure 1.4: *Relative HOMO-LUMO bands in type I and type II heterojunction*

one polymer lies within the band gap of other polymer (straddling gap). In this system exciton from higher band gap polymer can be transferred non-radiatively to the low band gap polymer by the dipole-dipole coupling when photoluminescence of donor materials overlaps with the absorption of acceptor material. In type II heterojunction both HOMO and LUMO of one polymer is lower than that of the other polymer. Type II heterojunction is a prerequisite for an efficient solar cell where charge transfer is more probable than energy transfer.

The D-A heterojunction can be modeled as metal-insulator-metal picture [50], that means HOMO of the donor material and LUMO of the acceptor materials act as valance and conduction band respectively of a semiconductor and energy difference of these two level is the band gap (E_g) as shown in the figure 1.5. The generation of free charge carriers is a two step process [51]. Exciton dissociation at the D-A interface which gives rise to electron-hole pair (also known as charge

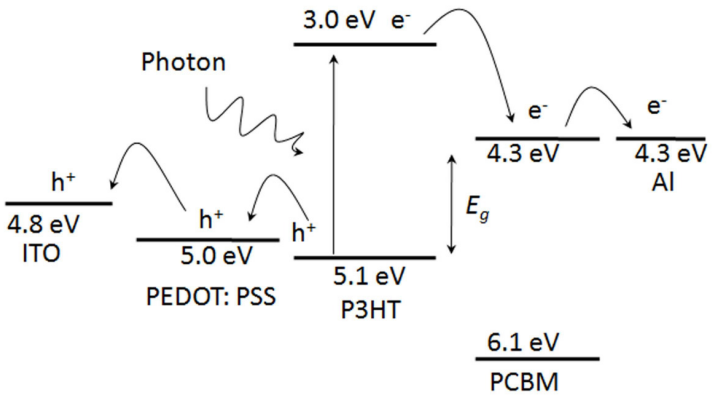

Figure 1.5: *Relative energy levels of P3HT (donor) and PCBM (acceptor) materials. Photogenerated excitons get dissociated at the interface and electrons and holes get transported to the respective electrode.*

transfer complex) and the breaking up of the electron-hole pair to free carriers. Hwang *et. al.* [52] proposed the dynamics of photogenerated carries as shown in the figure 1.6. The ultra-fast (less than 100 fs) exciton dissociation is driven by the

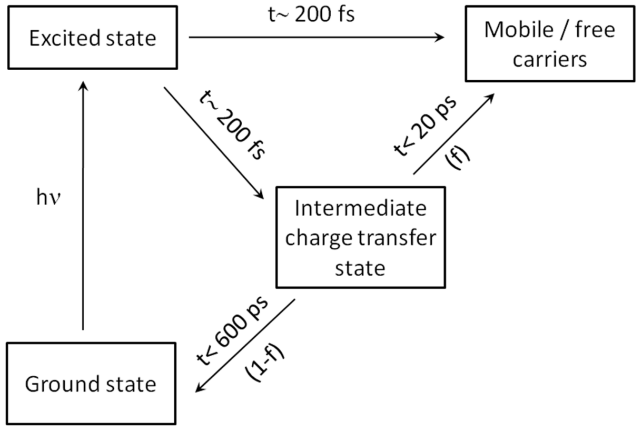

Figure 1.6: *Dynamics of photogenerated excitons proposed by Hwang et. al. [52]. There is only a fraction of photogenerated carriers (f <1) dissociates in free carriers and rest (1-f) of it decay back to ground state.*

difference between LUMO levels of the donor and acceptor materials. The exciton dissociation yield is almost unity and it is independent of electric field. Onsager

[53] first proposed the theory of geminate recombination to explain the dynamics of photogenerated carriers. According to Braun [54] the bound electron-hole pair has a finite lifetime before it decays back to ground state (k_f) or it can dissociate into free carriers. The separation into free carriers is a competition between dissociation rate constant (k_{diss}) and recombination rate constant (R). Thus the probability of exciton dissociation at a distance x under electric field F at a given temperature T is given by,

$$p(x, F, T) = \frac{k_{diss}(x, F, T)}{k_{diss}(x, F, T) + k_f(T)} \tag{1.10}$$

Braun [54] derives the dissociation rate constant (equation 1.11)

$$k_{diss}(x, F, T) = \frac{3R}{4\pi a^3} e^{-E_g/k_B T}(1 + b + b^2/3 + ...) \tag{1.11}$$

where E_B is the exciton binding energy, a is the Onsager radius and $b = q^3F/8\pi\epsilon k_B^2 T^2$, '$q$' is the elementary charge. The recombination rate is given by,

$$R = \beta(np - n_{int}^2) \tag{1.12}$$

where $n_{int} = N_c exp(-E_g/2k_B T)$ is the intrinsic charge carrier concentration with N_c being the effective density of states in the conduction band. β is the bimolecular recombination rate proposed by Langevin. In a pristine system,

$$\beta = \frac{q}{\epsilon}(\mu_e + \mu_h) \tag{1.13}$$

Since both carriers are free to move towards each other, the recombination lifetime taken is dominated by the fast moving carriers. In a blend film, electrons and holes are confined to their respective phases. Hence bimolecular recombination is

possible only at the D-A interface. The bimolecular recombination rate is modified as proposed by Braun *et. al.* [54],

$$\beta = \frac{q}{<\epsilon>} <\mu> \tag{1.14}$$

where $<\mu>$is the spatially averaged sum of electrons and holes mobility and $<\epsilon>$is the spatially averaged sum of dielectric constant. Hence in a blend system bimolecular recombination is governed by the slowest carrier [55]. The fast carrier will reach to the interface much before the slow carrier and get stuck due to energy band offset at the D-A interface. So the total time needed for both carriers to reach to the interface is dominated by the slowest carrier. Therefore in BHJ solar cell, the recombination is not expected to depend on $\mu_e + \mu_h$, but it will be close to

$$\beta = \frac{q}{\epsilon} min[\mu_e, \mu_h] \tag{1.15}$$

where 'μ_e' and 'μ_h' are electron and hole mobility respectively. The distance of between electron-hole pair is not uniform and hence it is reasonable to integrate equation 1.10 to calculate the overall dissociation rate,

$$P(a, F, T) = \int_0^\infty p(x, F, T) f(a, x) dx \tag{1.16}$$

where $f(a, x)$ is a normalized distribution function [56] given by,

$$f(a, x) = \frac{4}{\sqrt{\pi} a^3} x^2 e^{-x^2/a^2} \tag{1.17}$$

If G is the generation rate, then the rate at which electron-hole pair will get disso-

ciated is proposed by Barker *et. al.* [57]

$$\frac{dX}{dt} = G - k_f X - k_{diss} X + R \tag{1.18}$$

However, in steady state $dX/dt = 0$ and hence $G - k_f X = k_{diss} X - R$ which is same as the net generation of free carriers. The continuity equation for electron (hole) will then be

$$\frac{dn(p)}{dt} = \frac{1}{q}\frac{\partial}{\partial x} J_{n(p)} + k_{diss} - R \tag{1.19}$$

Substituting from equation 1.10 and 1.16 $k_{diss} = [P/(1-P)]k_f$. The continuity equation will be modified as,

$$\frac{1}{q}\frac{\partial}{\partial x} J_{n(p)} = PG - (1-P)R \tag{1.20}$$

It is to be noted that after bimolecular recombination, carriers are not necessarily lost. However they can again dissociate into free carriers or they can decay back to ground state, in that case carriers are lost. So the net generation rate becomes

$$U = PG - (1-P)\beta(np - n_{int}^2) \tag{1.21}$$

This formalism is used in next section to estimate the photogenerated current.

1.3.3 Basic equation of a solar cell

The solution of Poisson equation is the basic equation for solar cells given as,

$$\frac{\partial^2}{\partial x^2}\psi(x) = \frac{q}{\epsilon}[n(x) - p(x)] \tag{1.22}$$

where 'q' is the elementary charge, 'ϵ' is the polymer dielectric constant, '$\psi(x)$' is the potential at point 'x' due to electron density '$n(x)$' and hole density '$p(x)$'. The current continuity equation is given as,

$$\frac{\partial}{\partial x}J_n(x) = qU(x), \frac{\partial}{\partial x}J_p(x) = -qU(x) \tag{1.23}$$

where '$J_{n(p)}(x)$' is electron(hole) current and '$U(x)$' is the net carrier generation rate, i.e. the difference between photogenerated carriers and recombination of free carriers. In order to solve these equations there should be some equation correlating the charge carrier density and potential to the current density. Drift-Diffusion model is used to describe photogenerated current. Introducing drift and diffusion component to the current,

$$J_n = -qn\mu_n\frac{\partial}{\partial x}\psi + qD_n\frac{\partial}{\partial x}n \tag{1.24}$$

and

$$J_p = -qp\mu_p\frac{\partial}{\partial x}\psi - qD_p\frac{\partial}{\partial x}p \tag{1.25}$$

where '$D_{n,P}$' are the carrier diffusion coefficient and follows Einstein's relation,

$$D_{n,p} = \mu_{n,p}V_t \tag{1.26}$$

'$V_t = k_BT/q$' is the thermal voltage of the carrier. A unique solution of these set of equations can be achieved by introducing boundary conditions, i.e. carrier concentration and potential at both the electrodes. At top contact, $x = 0$ and at bottom contact, $x = L$ where L is the polymer thickness. Assuming an ohmic contact at both electrode, the carrier concentration can be given by the simple

Boltzmann distribution at $x = 0$,

$$n(0) = N_c, p(0) = N_c exp\Big(-\frac{\varepsilon_{gap}}{V_t}\Big) \tag{1.27}$$

and at the bottom electrode at $x = L$

$$n(L) = N_c exp\Big(-\frac{\varepsilon_{gap}}{V_t}\Big), p(L) = N_c \tag{1.28}$$

The boundary condition for the potential is given by the equation 1.29

$$\psi(L) - \psi(0) = \varepsilon_{gap} - V_{applied} \tag{1.29}$$

where '$V_{applied}$' is the applied voltage.

1.3.3.1 Photogenerated current J_{ph} & Short circuit current J_{SC}

The solution $J_{n,p}$, a measure of photogenerated current, can be computed by iterative methods. We will look at the steady state photocurrent. At high reverse bias, photocurrent tends to saturate. This indicates that all the photogenerated carriers are extracted from the device, provided the drift length of electrons and holes ($L_{e,h}^{drift}$) become equal or larger than the device thickness (d). Saturated photocurrent is $J_{ph}^{sat} = qGd$ assuming no recombination is taking place. Photocurrent would be space charge limited if one or both of the carriers drift length is smaller than the thickness of the film. In case of a imbalanced transport ($\mu_e\tau_e \neq \mu_h\tau_h$) of electrons and holes, charge carriers get accumulated near one of the electrode and photocurrent becomes field dependent [58] as given by the equation 1.30

$$J_{ph} = qG[(\mu\tau)_{slowcarrier}]^{0.5}V^{0.5} \tag{1.30}$$

where $V = V_{applied} - V_{built-in}$. Comparing J_{ph} to standard space charge model [$J_{SCL} = (9/8)\epsilon_0\epsilon_r\mu(V^2/d^3)$] [58], photogenerated current $J_{ph} \propto G^{3/4}$. Tessler *et. al.* performed a detail numerical analysis of J_{ph} over a wider intensity range [59]. It is found that at high intensity of light, photocurrent could be space charge limited even though carrier mobilities are comparable.

The device parameters play a significant role to describe the current-voltage (J-V) characteristics of a solar cell based on a diode model. An organic photovoltaic device can also be described by a Shockley equivalent circuit [60] as conventional p-n junction solar cell and J-V characteristic [61] can be approximated by

$$J(V) = \frac{1}{1 + R_s/R_{sh}}\Big[J_0\Big\{exp\Big(\frac{V - J(V)R_sA}{nk_BT/q}\Big) - 1\Big\} - \Big(J_{ph} - \frac{V}{R_{sh}A}\Big)\Big] \quad (1.31)$$

'J_{ph}' is the saturated photocurrent given by the equation 1.30. Here 'R_s' and 'R_{sh}' represent two parasitic series and shunt resistance respectively. 'A' is the area of the device. 'J_0' represents the dark saturated current and 'n' is the ideality factor. Thus at $V = 0$, short circuit current J_{SC} is estimated as

$$J_{SC} = J(0) = \frac{1}{1 + R_s/R_{sh}}\Big[J_0\Big\{exp\Big(\frac{-J(0)R_sA}{nk_BT/q}\Big) - 1\Big\} - J_{ph}\Big] \quad (1.32)$$

Fill factor of a solar cell depends on parameters R_s and R_{sh} which can be extracted from the experimentally obtained $J(V)$ curve. Series resistance R_s represents the charge extraction resistance whereas shunt resistance R_{sh} represents the carrier recombination loss. Hence lower R_s and higher R_{sh} is expected for an efficient BHJ solar cells.

1.3.3.2 Origin of open circuit voltage V_{OC}

The open circuit voltage V_{OC} is an important parameter for performance of solar cell as well as to understand the charge generation and separation phenomena. The relevant band diagram of a bulk heterojunction solar cell is presented in figure 1.5. Two different energy levels which can govern the V_{OC} are the effective band gap E_g corresponding to the energy of the polaron pair after exciton dissociation, and the difference of the work functions of anode and cathode. However the band bending at the D-A interface may result in reduced V_{OC} as proposed by Cheyns *et. al.* [62]

$$V_{OC} = \frac{E_g}{q} - \frac{k_B T}{q} ln\Big(\frac{N_D N_A}{pn}\Big) \tag{1.33}$$

where 'N_D' and 'N_A' donor and acceptor effective density of states and 'p' and 'n' are the hole and electron concentration at the interface respectively. Koster *et. al.* proposed another model where V_{OC} depends on light intensity and hence the generated photocarriers [63]

$$V_{OC} = \frac{E_g}{q} - \frac{k_B T}{q} ln\Big[\frac{(1-P)\beta N^2}{PG}\Big] \tag{1.34}$$

'N' is the effective density of states, 'β' is Langevin recombination rate. Later Vandewal *et. al.* [64] showed that V_{OC} is proportional to effective bandgap and is given by an empirical relation $V_{OC} = E_{g(effective)} - 0.43$ V. Effective bandgap depends on the polaron pair energy. Hence V_{OC} also depends on materials properties and can be optimized by reducing the energy gap between donor-LUMO to acceptor-LUMO without affecting the back electron transfer rate.

1.3.4 Solar cell architecture

Polymer solar cell consists of photo-active polymer materials sandwiched between two different work function materials which enables the charge separation at the polymer electrode interface. But in most of the cases, work function difference is not sufficient enough to dissociate strong columbically bound electron-hole pair. To achieve high efficiency device it is mandatory to have a Donor-Acceptor heterojunction to break up high binding energy excitons. This leads to different types architecture of polymer based solar cells (i) planar (bi-layer) heterojunction (ii) ordered (finger like) heterojunction and (iii) bulk heterojunction as shown in the figure 1.7.

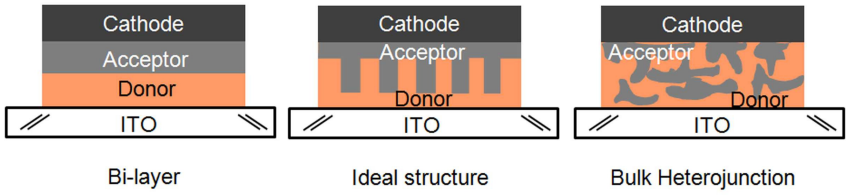

Figure 1.7: *Three different architecture, bilayer, finger like(ideal) and bulk heterojunction solar cells.*

In case of planar heterostructure, photogenerated excitons get dissociated only at the bi-layer interface (exciton diffusion length <10 nm). The photocarrier generation occurs only at the D-A interface although photoabsorption is within the bulk. The choice of solvent plays an important role to form a bilayer structure. Recently, Wang *et. al.* [65] showed the effect of solvent at the bilayer interface where donor polymer with acceptor material forms a graded structure [66].

An ideal structure proposed in the literature for obtaining high efficiency is the interdigitated ordered periodic structure where photogenerated exciton in the donor materials encounters an acceptor interface within 10 nm. Such solar cell architecture can be formed by infiltrating polymer into the nano-structured oxide

layers. Titania (TiO_2) template with a mesoporous structure (pore size should be of the order of exciton diffusion length) can be made by several techniques [67–69]. The thickness of the nanostructure titania film is in the range of 300 - 500 nm. The polymer infiltrated TiO_x is covered with a thin layer of polymer film to avoid direct contact between TiO_x and hole collecting electrode and hence reducing the dark current magnitude. In this geometry TiO_x acts as the electron acceptor and can be grown or spin casted on indium tin oxide (ITO) or fluorine doped tin oxide (FTO). Gold (Au) or silver (Ag) acts as anode. However, efficiency observed is not significantly high [70–72]. Heeger *et. al.* demonstrated that TiO_x can be used as optical spacer [73] and as a protective layer as well [74].

Bulk heterojunction approach is popular as it is least complex in implementation. The approach involves mixing of donor and acceptor materials in a common solvent followed by deposition on the substrate where it forms intimately entangled network of donor and acceptor phases. The length scale (order of nm) at which the phase separation happens depends on the various processing parameters as well as the starting materials. Ideally, the domain size of each phase should be the same as exciton diffusion length so that the photogenerated exciton can find an interface within the diffusion length. The transport through the bicontinuous network depends on the morphology of the devices. Numerous techniques such as solvent assisted annealing, thermal annealing, use of additives, are used to optimize the device morphology. Recent report on vertical phase segregation of P3HT and PCBM by Nelson group [75] also suggests the importance of appropriate phase separation.

1.3.5 Physical processes in BHJ-PSCs: Efficiency limit

The sequence of processes present in the BHJ polymer solar cells are as follows; (i) photon absorption (η_A), (ii) exciton dissociation (η_{ED}), (iii) charge transport (η_{CT}) and (iv) charge collection (η_{CC}). The power conversion efficiency (η_{IPCE}) depends on all the factors listed above and it is given by the equation 1.35

$$\eta_{IPCE} = \eta_A \eta_{ED} \eta_{CT} \eta_{CC} \tag{1.35}$$

Since conjugated polymers have higher absorption coefficient ($\alpha \sim 10^5$ cm^{-1}) in the visible range, thin films of $\sim$ 100 nm thickness are necessary to absorb most of the incident photon flux. However, solar spectrum contains significant NIR component ($\sim$ 45%) as compared to visible range ($\sim$ 47%). Due to the wide band gap of the organic semiconductor most of the NIR photons are not harvested. In recent years, development of low band gap polymers ($\epsilon_g \sim 1.5$ eV) [76–78] has led to a better absorption till 900 nm (Fig. 1.8). The absorption efficiency can be calculated from the Beer-Lambert law taking into consideration that the reflectivity from the surface is R and thickness of the polymer film is d,

$$\eta_A = (1 - R)(1 - e^{-\alpha d}) \tag{1.36}$$

Absorption efficiency can be improved by using an antireflection coating [79–81] on top of the solar cell, using an optical spacer to increase the electric field [82–84] intensity of incident photon in the polymer film, introducing micro and nanostructure to increase the plasmonic effect [85–87] and hence the absorption efficiency.

The exciton binding energy is more than the thermal energy ($k_BT \sim 25$ meV at room temperature). The exciton dissociation can happen only at the D-A het-

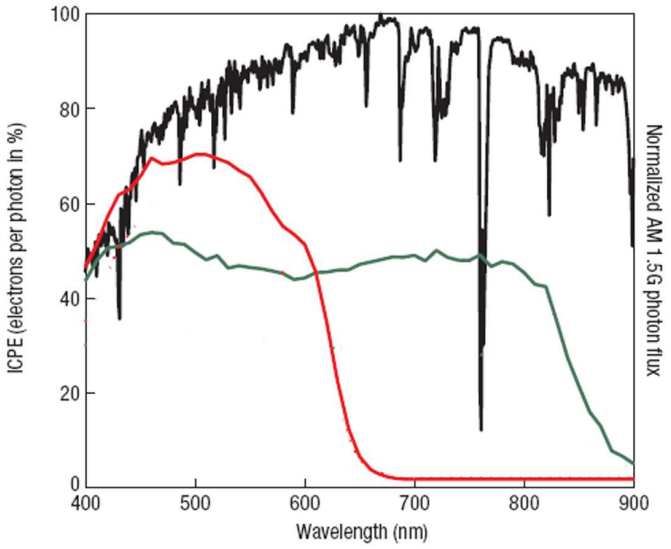

Figure 1.8: *Black line indicates the solar cell spectrum. Red line is the photocurrent spectrum of P3HT:PCBM blend polymer solar cell and green line is the photocurrent spectrum of of PCPDTBT:PCBM polymer solar cell. Figure is adopted from the reference [76].*

erojunction. The exciton diffusion length L_D in conjugated polymer is reported 5 - 20 nm [88]. Because of much smaller diffusion length scale efficiency of a bilayer device is limited by the photogenerated carriers. This limitation is shorted out by the introduction of BHJ concept where an exciton generated in the photoactive donor materials always finds an interface within 10-20 nm. The efficiency of the exciton dissociation (η_{ED}) depends on the binding energy of the exciton and the energy offset at the D-A interface. Detail of exciton dissociation is discussed in Section 1.3.2.

The charge transport in the BHJ-PSCs is one of the most complicated processes to understand. After the exciton dissociation the free carriers (electrons in acceptor materials and holes in donor materials) get transported through the percolating pathways. Carrier mobility of electron and hole play a significant role to the device

current-voltage (I-V) characteristic. The mobility lifetime product ($\mu\tau$) of electron an hole in the acceptor and donor materials respectively should be equal for high efficient devices [89]. In pristine PCBM the electron mobility ($\mu_e = 2.0 \times 10^{-3}$ cm^2/Vs) [90] was found to be 4000 times higher than the hole mobility in pure MDMO-PPV ($\mu_h = 5.0 \times 10^{-7}$ cm^2/Vs) [91]. In the blend film, mobility gets modified. In PPV:PCBM blend film, hole mobility gets enhanced [92] in the field effect transistor measurement. However in solar cell or light emitting diode (LED) structure mobility is always lower than the field effect mobility due to the low concentration of charge carriers. [93]. Recently Blom *et. al.* have shown that the hole mobility in MDMO-PPV:PCBM blend (1:4 by wt. ratio) is enhanced by more than two orders of magnitude compared to pristine MDMO-PPV film [94]. This enhancement in the mobility upon blending with the acceptor materials is not well understood. However the addition of PCBM may enhance the packing of the MDMO-PPV morphology and make it favorable for hole transport. There are other reports on nano-phase separated morphology and higher crystallinity of the polymer which play a significant role to improve the charge transport efficiency (η_{CT}).

Effect of polymer/electrode interface on device performance is also reported in the literature. The charge carrier collection (η_{CC}) at the polymer electrode interface mostly depends on the work function of the electrodes and the HOMO-LUMO band of the polymer. In a classical metal-insulator-metal (MIM) model, open circuit voltage is defined by the work function difference between two electrodes, provided the Fermi levels of two electrodes are within the band gap of the polymer. However, when polymer makes an ohmic contact with the electrode, charge transfer from metal to semiconductor takes place in order to align the Fermi level. Hence electrode work function gets pinned to the HOMO/LUMO level of the semi-

conductor [95], consequently V_{OC} is defined by the band gap of the semiconductor. In BHJ structure, band gap is defined by the difference of donor-HOMO level to the acceptor-LUMO level. The origin of V_{OC} in BHJ-PSCs is described by Brabec *et. al.* [96]. Recently it is found that η_{CT} also depends on the polymer/electrode interface properties. Gupta *et. al.* [89] have reported that the process of cathode material deposition play an important role to determine the fill factor of the devices. Relatively slow deposition of Al electrode on polymer film leads to a conformal coating which is necessary for higher charge collection rate. Verification of this argument was carried using metallic alloy and the details of this approach are discussed in section 5.5.1.1.

1.4 Materials

Materials used for solar cells are broadly classified into two categories: (i) active polymer semiconductors, (ii) conducting materials as electrodes and buffer layer materials. Active polymer matrix absorbs light and creates free charge carriers which should be efficiently collected by the top and bottom electrode.

1.4.1 Polymer semiconductors for solar cells

The polymer semiconductors are mostly donor type because of higher air stability, although there are very few report on acceptor type air stable polymers [97]. In this section, some of the donor type (Fig. 1.9) and acceptor (Fig. 1.10) type polymers and macromolecules which are extensively used in polymer solar cells will be discussed. Their optical and electrical properties are also mentioned in brief.

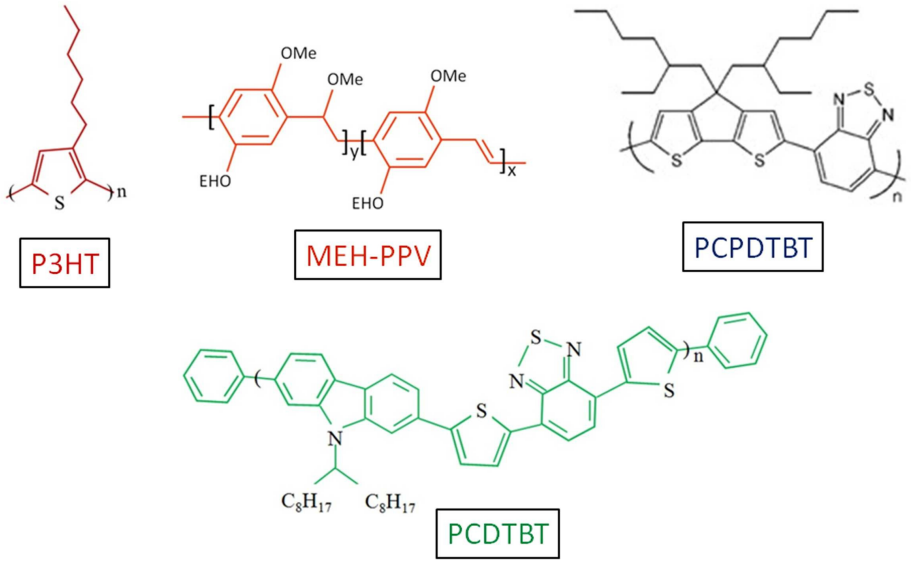

Figure 1.9: *Very commonly used electron donating (donor) materials for high efficiency solar cells.*

1.4.1.1 P3HT

One of the most common polymer in the area of polymer electronics is poly-[3-hexylthiophene] (P3HT) with sufficient thermal stability (T_g >150 °C). P3HT belongs to the group of alkyl-substituted thiophene compound with optical band gap 1.9 eV [98]. The conjugation of thiophene ring can have different kinds of orientation called HH (Head-Head), TT (Tail-Tail) and HT (Head-Tail) or the combination of H & T. The optical and electrical properties of P3HT depend on the polymer conjugation length. Hence P3HT is broadly classified as RR-P3HT (regioregular) and RRa-P3HT (regiorandom) where electrical characterization shows different responses [99]. It is evident from crystallographic study that P3HT film starts aggregating in a stacked interlocking comb-like structure. A XRD peak is observed in a thin P3HT film and is assigned to (100) plane due to lamellar layer structure [100]. Crystallinity of P3HT also depends on the molecular weight [101, 102] and

the conjugation length.

1.4.1.2 PCPDTBT

Poly[2,6-(4,4-bis-(2-ethylhexyl)-4H-cyclopenta[2,1-b;3,4-b']-dithiophene)-*alt*-4,7-(2,1,3-benzothiadiazole)] (PCPDTBT) is one of the most promising low band gap polymer ($E_g \sim 1.5$ eV) first reported by Brabec *et. al.* [103]. In this system cyclopentadithiophene unit is used as donor block in the polymer backbone. It shows increased charge transport properties as well as optimum energy level with a broad absorption spectrum ranging from 300 nm to 900 nm. From the cyclic voltammetry (CV) test, the HOMO and LUMO of this polymer were calculated at ca. 5.3 and 3.57 eV with a band gap of 1.73 eV. However, from optical absorption study the band gap is expected to be lower than the band gap from CV measurement. PCPDTBT absorption spectrum in the solution and in the film form shows $\sim$ 70 nm red shift. Such kind of shift is expected for a rigid conjugated polymer with a strong interchain interaction due to a $\pi - \pi$ stacking.

1.4.1.3 PCDTBT

Poly(N-alkyl-2,7-carbazole) derivative poly[N-9'-heptadecanyl-2,7-carbazole-alt-5,5-(4',7'-di-2-thienyl-2',1',3'-benzothiadiazole)] (PCDTBT) is a low band gap, air stable polymer with high mechanical stability (T_g >130 °C). The detailed synthesis of this polymer is reported in the literature [104]. PCDTBT shows relatively high molecular weight (number average $M_n = 37$ and weight average $M_w = 73$ kDa). This polymer shows excellent thermal stability (5% degradation at 430 °C).

All three polymers discussed above are electron donating polymers. There are other types of donor polymer generally used for BHJ devices. Polyphenylene

vinylene (PPV) derivatives such as; poly[2-methoxy-5-(3,7-dimethyloctyloxy)-p-phenylene vinylene] (MDMO-PPV) [105] and poly[2-methoxy-5-(2-ethylhexyloxy)-1,4-phenylenevinylene] (MEH-PPV) [106], polyfluorene based polymer like [poly(9,9'-dioctylfluorene-co-bis-N,N'-(4-butylphenyl)-bis-N,N'-phenyl-1,4-phenylenediamine)] (PFB) and [poly(9,9'-dioctyl fluorene-co-bis-N,N'-(4-butylphenyl) diphenylamine)] (TFB) polymers are reported in the literature [107].

There are very few electron accepting polymers, like polyfluorene based [poly(9,9'-dioctyl fluorene-co-benzothiadiazole)] (F8BT) [108], PPV based Cyano-Polyphenylene vinylene (CN-PPV) Polymers. But most commonly used electron acceptors are the C_{60}, and its derivatives. Optical properties of all materials are listed in the table 1.1

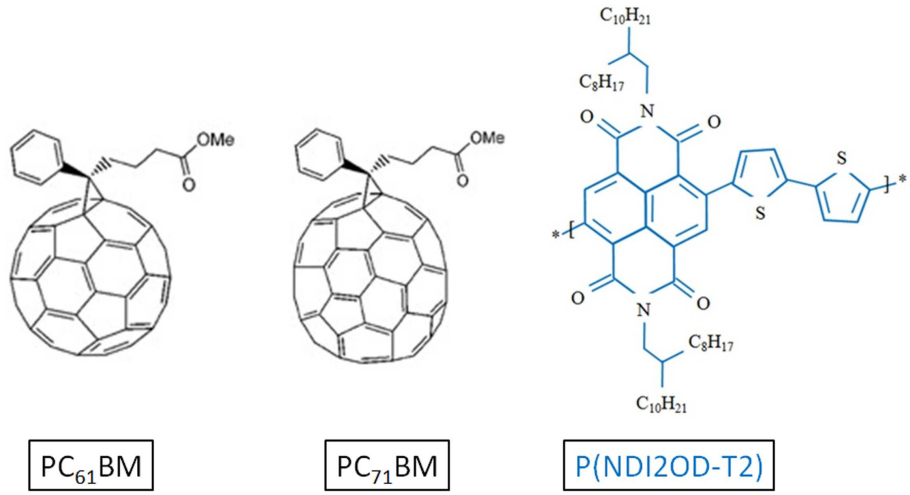

Figure 1.10: *Very commonly used electron accepting (acceptor) materials for high efficiency solar cells.*

1.4.1.4 PCBM

[6,6]-phenyl-C61-butyric acid methyl ester (PCBM) is a soluble derivative of buckminsterfullerene. Functionalized fullerene has found many applications in the area

of optoelectronics and it is extensively used in organic solar cells. High electronegativity of C_{60} makes this a wonderful acceptor material. The detailed material chemistry of PCBM has been discussed by López *et. al.* [109]. PCBM shows high UV absorption (350 nm) compared to visible range due to symmetry forbidden first excited state (S_1) and emission at 700 nm [110]. PCBM can take more than one electron even in excited state. The charge transfer rate is very fast (order of femtosecond) whereas back transfer (recombination) rate is much slower as expected for acceptor materials. The use of C_{70} based PCBM in BHJ-PSCs is more efficient [111] than C_{60} based PCBM as C_{70} is more non-centrosymmetric than C_{60}.

1.4.1.5 P(NDI2OD-T2)

Poly[N,N'-bis(2-octyldodecyl)-naphthalene-1,4,5,8-bis(dicarboximide)-2,6-diyl]-*alt*-5,5'-(2,2'-bithiophene) [P(NDI2OD-T2)] is a NDI-based electron transporting polymer, first reported by Yan *et. al.* in 2009. This is also commercially available with Polyera ActivInk, USA, commonly known as N2200. N2200 is a air stable, low band gap ($E_g \sim 1.5$ eV) photoactive (absorption peak at 700 nm) n-type polymer with a mobility of 0.45 - 0.85 $cm^2V^{-1}S^{-1}$ under ambient condition [97]. N2200 has been used extensively for n-channel FETs [112, 113], but is hardly any report where N2200 has been used as electron acceptor materials in a BHJ solar cells.

Table 1.1: *Optical properties of solar cell materials*

Materials	**HOMO**	**LUMO**	**Optical band gap**
P3HT	5.1 eV	3.0 eV	1.9 eV
PCPDTBT	5.3 eV	3.57 eV	1.46 eV
PCDTBT	5.6 eV	3.6 eV	1.9 eV
N2200	5.6 eV	4.0 eV	1.5 eV
PCBM	6.1 eV	4.3 eV	$\sim$ 2.0 eV

1.4.2 Conducting electrode materials and buffer layer materials

There are other materials such as electrodes, electron as well as hole conducting/blocking layer materials or sometimes optical spacer materials to increase the light absorption. They are very essential to determine the overall device performance. Here we list necessary materials for solar cell fabrication.

1.4.2.1 Transparent conducting oxide (TCO)

Transparent conducting oxides (TCOs) are employed as transparent electrodes in flat-panel displays, light-emitting diodes, electrochromic windows, and solar cells [114–116]. Although there are important secondary requirements for such transparent electrodes (e.g., interfacial properties, chemical stability, etc.), the primary requirements are high electronic conductivity and good visible transparency (in thin film form). In addition, band alignment matching with the active absorber components is important. For organic conductors, the band alignment at the TCO interface is expected to depend directly on TCO work function [117, 118]. TCOs are mostly wide bandgap (3 - 5 eV) n-type semiconductors. Conductivity of these oxides depends on the doping level. Typically used TCOs in solar cell application are Indium tin oxide (ITO) ($E_g \sim 2.8$ eV), Fluorine doped tin oxide (FTO) ($E_g \sim 3.6$ eV) and Zinc oxide (ZnO) ($E_g \sim 3.3$ eV). The work function ($\phi_f = E_{VAC} - E_F$) of these TCOs depends on the doping concentration. It is observed that the UV-ozone treatment on ITO increases ϕ_f. This is due to the reduction of carbon atoms and the formation of the Sn deficient and O-rich surface by the treatment [119]. Hence solar cell efficiency increases [120].

1.4.2.2 Conducting polymer PEDOT:PSS as buffer layer

In all the solar cell devices a thin buffer layer of conducting polymer poly(3,4-ethylenedioxythiophene)/poly(4-styrenesulfonic acid) [PEDOT:PSS] is used to increase the charge collection efficiency. This conducting polymer is a good electron blocking hole transporting layer. PEDOT:PSS is a water soluble dispersion of colloidal particles containing PEDOT and PSS-Sodium. PEDOT alone is found to

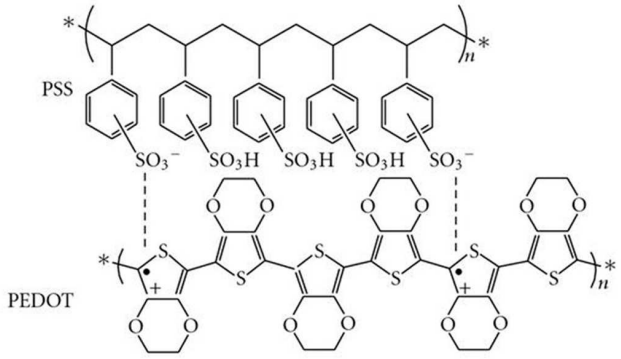

Figure 1.11: *Chemical structure of a PEDOT:PSS. The 'dot' and 'plus' represent the unpaired electron and positive charge on the PEDOT chain, respectively.*

be insoluble in water. The solubility problem was solved by adding a water soluble PSS as charge balancing dopant during polymerization to yield PEDOT:PSS [121, 122]. The conductivity of PEDOT:PSS film can be modified by doping and proper annealing conditions [123]. For solar cells PEDOT:PSS is used on top of ITO ($\phi_f \sim 4.8$ eV) coated glass substrate. ITO/PEDOT:PSS composite works as hole collecting layer ($\phi_f \sim 5.1$ eV) as it forms more ohmic contact with the polymer HOMO level. This has been observed in electroabsorption spectroscopy [124].

1.4.2.3 Hole blocking layer and cathode materials

In general, low work function metals like Al (ϕ_f=4.3 eV), or Ca (ϕ_f=2.9 eV) are used as cathode materials to match with the LUMO level of the acceptor materials. Ca is highly reactive material. Hence after deposition of Ca, a thick layer of Al deposition is necessary to encapsulate the device. A thin layer (5-10 nm) of LiF is used as hole blocking layer [11] to improve the charge collection at the polymer/electrode interface. The use of pentacene as hole blocking layer is also reported in the literature [125]. Recently Reinhard *et. al.* have reported that solution processed CsF increases V_{OC} by 0.3 V in an inverted geometry [126]. In case of inverted structure, a thin nano-structured oxide layer (ZnO, TiO_2) is introduced between bottom electrode ITO and polymer. These oxides act as hole blocking electron conducting layer and improve the efficiency of inverted organic solar cells.

1.5 Polymer solar cell measurements

Solar cells characterization is necessary to estimate device performance. The current-voltage (J-V) measurement is carried out under white light illumination (Xe lamp, typically 80 - 100 mW/cm^2) as well as under dark condition from +1 V to -1 V range. J-V characteristic under dark essentially indicates a diode signature with high rectification. The light I-V curve in the fourth quadrant (Fig. 1.12) is a representation of device efficiency where the diode is operating in 'injection' mode. The current at V = 0 V represents the short circuit current (J_{SC}) where the recombination loss is minimum. The voltage at which current is zero is open circuit voltage (V_{OC}) where recombination is same as the carrier generation rate. The product of $V_{OC} \times J_{SC}$ is the pseudo power. The actual power output is

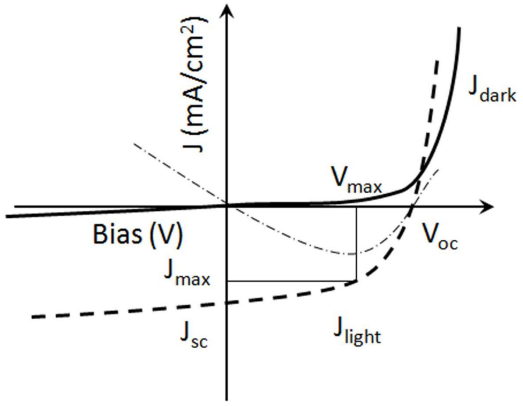

Figure 1.12: *Current-voltage characteristic of a polymer solar cells. Black solid line indicates the dark J-V curve, dashed line indicates the J-V curve under light illumination, dashed-dotted line represents power output.*

$V_{max} \times J_{max}$. The ratio of actual (maximum power) output to that of the pseudo power output is the fill factor (FF). The power conversion efficiency is calculated using the expression $\eta = FF \times V_{OC} \times J_{SC}/P_{in}$ where P_{in} is the incident optical power density (in mW/cm^2).

Other type of measurement is related to the external quantum efficiency (EQE) where EQE is a function of incident photon wavelength. The photocurrent responsivity $S(\lambda)$ (mA/W) follows the absorption spectrum of the polymer. An empirical relation can be used to estimate the EQE,

$$EQE(\eta_{IPCE}) = \frac{S(\lambda) \times 124}{\lambda}\% \tag{1.37}$$

where λ is in nm. The factor 124 comes from hc/q where 'c' is velocity of light and 'h' is the Planck's constant.

Understanding of BHJ devices is necessary to improve the device performance. Hence there are several other characterization and measurement techniques commonly used for solar cells. Intensity modulated photocurrent measurement is one

of them to understand various photophysical processes involved in an active device. The frequency dependent modulated current analysis and phase shift analysis gives the energy distribution of localized states [127, 128]. AC impedance measurement under white light illumination as well as in dark is necessary to estimate the device photocapacitance and resistance and its effect on solar cell performance.

1.6 Thesis outline

In the field of organic electronics, solar cells have undergone tremendous improvement in terms of efficiency in the last decade. Considerable emphasis has been put on the early stages of the charges separation process in a BHJ. The secondary processes of electrical transport accompanied by trapping and recombination events are also equally important. The present work focuses on the events in this regime (> 1 μs) in these BHJs. Even though there are reports on light intensity modulated photocurrent spectroscopy (IMPS) and phase shift analysis to understand the transport in Dye Sensitized Solar Cells (DSSCs), these IMPS based methods have not been applied BHJ-PSCs. In this thesis, modified IMPS is used to understand the carrier dynamics in an active device. It is observed that the modulated photocurrent spectrum of a BHJ-PSC shows a universal feature in the frequency range 5 to 10 kHz in terms of a peak. The origin of photocurrent peak is modeled in terms of exciton generation and dissociation, free carrier transport and recombination, trap kinetics and charge extraction at the polymer electrode interface. The activation energy for the charge carriers has been estimated from the temperature dependent modulated photocurrent measurement. The fine features especially at low frequency range have been closely observed and analyzed where morphology and composition play a significant role. The modified IMPS is also

carried on bilayer polymer solar cells and DSSCs where photo-physics is completely different from BHJ-PSCs. The photocurrent peak at 5-10 kHz is absent in these above mentioned cases. AC impedance measurement in dark as well as under white light illumination is also carried out on the same sample to estimate resistance and capacitance values. The frequency dependent capacitance and resistance under white light with different bias voltage show some crossover at frequency range of 3-4 kHz. The anomaly in the loss angle measurement shows local minima in the 5 kHz frequency range.

Following the frequency dependent studies, the noise patterns of the BHJ-PSCs in active working condition are probed. The complex sequence of generation, separation and transport of the photogenerated carriers manifests in the form of characteristic noise signal. The power spectral density (PSD) of the short circuit current fluctuation takes a Gaussian form in the 10 kHz to 90 kHz frequency regime. The noise studies were carried out under different experimental conditions; namely temperature, light intensity and efficiency of the devices. In general, the magnitude of the photocurrent fluctuation reduces with decreasing temperature. The photocurrent fluctuation amplitude is observed to increase with increasing light intensity. The origin of the photo-current fluctuation is attributed to the density of trap states present in the device.

Polymer photodetectors are other promising areas of research and technology. Ease of fabrication on flexible substrate made them more attractive in the areas of curved image sensor and detectors. With the development of low band gap polymers, the absorption tail is extended upto 900 nm. The optimum composition of low band gap donor blended with acceptor materials is used to fabricate photodetector especially at near infra-red (NIR) regime. The characterization is done under different experimental conditions such as temperature dependent study, bias

dependent transient response measurement and transient under white background illumination. The effect of trap filling and detrapping of charge carriers on the device response time is observed.

Electric field induced instability has been studied on dielectric visco-elastic materials in a thin film ($\sim \mu m$) form. It has also been noticed that conducting liquid surface deforms under the external electric filed. The deformation dynamics of a small conducting liquid drop under electric field is closely investigated in this thesis. There are two distinct regimes: at low electric field the growth of a droplet is linear with the applied voltage, whereas at high field regime, the system becomes unstable. The deformation of droplet at low field regime is utilized to fabricate organic electronics devices such as polymer light emitting diodes (PLEDs) and polymer solar cells (PSCs) with efficiency comparable to device with conventionally deposited electrode. This technique also provides a vacuum free low temperature electrode deposition for enabling fill factor limiting studies.

SECTION 2

Impedance Spectroscopy: Intensity modulated photocurrent (IMP) features of BHJ solar cells

2.1 Introduction

Intensity modulated photocurrent spectroscopy (IMPS) is a valuable complementary approach for transient measurements to study charge carrier-relaxation processes. This technique involves measurement of photocurrent in response to a superimposition of small sinusoidal perturbation in presence of larger CW illumination (bias-offset). The technique has been traditionally used for Gratzel cells [129, 130] and disordered a-Si cells [131, 132] to highlight the relaxation mechanisms related to carrier life time, transit time and recombination dynamics. The use of relatively small modulation amplitudes has an advantage that the diffusion coefficient of electrons is primarily determined by the CW illumination intensity. Phase shifts in modulated photocurrent measurements in absence of a CW background have also been utilized to extract density of trap states [133, 134]. However in bulk heterojunction polymer solar cells (BHJ-PSCs), intensity modulated photocurrent has not been studied extensively. In this section, utilizing a modified IMPS approach, the effect of various processes in BHJ-PSCs has been studied. All polymer based BHJ devices show a common feature in modulated photocurrent

spectrum.*

Bulk-heterojuction polymer solar cells (BHJ-PSCs) are promising alternatives for conventional inorganic photovoltaic with relatively low manufacturing complexities. Efficiency (η) in the range of $\sim 8\%$ has been achieved [38, 39] for bulk heterojunction polymer/fullerene solar cell. The general approach to improve these devices has been to explore novel compatible electron donor (D)-acceptor (A) systems which covers a wide absorption region [104, 135] over the solar spectrum, along with minimizing losses in the different photophysical processes involving charge transfer and separation [136]. The network morphology [137, 138] and the optimized gradients of the appropriate phases at the electrodes [139] in these BHJ-PSCs have also been observed to play an important role in determining the properties of these devices. There are growing options for the donor component of the BHJs, with a range of materials having desired energy levels to facilitate the ultrafast photoinduced charge transfer processes [9, 140]. A common set of features in these systems includes the existence of ultrafast photoinduced charge transfer across the D-A interface, and open circuit voltage (V_{OC}) related to difference in the D-HOMO level and the A-LUMO level [141]. We observe an additional universal feature in the BHJ-PSCs in form of a local feature in modulated photocurrent (I_{ph}) and attribute it to a characteristic combination of correlated fundamental processes occurring over multiple time scales. This feature was studied in all variety of BHJ systems. All the necessary measurement details were also carried out. Model was constructed to simulate the results.

*Based on these studies, paper has been published in *Phys. Rev. B* **82**, 075308 (2010).

2.2 Device fabrication & measurement details

Polymer solar cells in sandwich configuration were fabricated using standard protocol: (i) cleaning of ITO glass substrate (ii) spin casting of PEDOT:PSS layer on top of ITO and subsequent annealing (iii) preparation of donor-acceptor blend in an appropriate solvent (iv) spin casting of polymer blend on top of PEDOT:PSS and finally (v) controlled and uniform deposition of cathode materials by physical vapor deposition technique. The cleaning of ITO glass substrate plays a vital role to determine the device efficiency as well as the reproducibility. ITO glass substrates were thoroughly cleaned with a soap water, ethanolamine, isopropyl alcohol and acetone (1:1) mixture and finally rinsed with distilled water. Substrates were further cleaned using RCA protocol: a mixture of hydrogen peroxide (H_2O_2), ammonium hydroxide (NH_4OH) and water (1:1:5 by volume) and boiled at 80 °C for 15 minutes. PEDOT:PSS was filtered through 40 μm filter paper and subsequently spin casted ($\sim$ 80 nm) onto the ITO glass substrates at 2000 rpm for 60 seconds. Substrates were then annealed at 120 °C for 30 minutes. Polymer blend with appropriate donor-acceptor ratio in appropriate solvent (typically 20 mg/ml concentration, stirred overnight and filtered through 0.22 μm filter) was then spin casted on top of PEDT:PSS film inside a nitrogen filled glove box ($<$ 1 ppm O_2 and $<$ 1 ppm H_2O) at 1000 rpm speed for 60 seconds. Devices were heated at 80 °C for 30 minutes to remove the solvent. The counter electrode (Al or Ca/Al cathode) was deposited (40-60 nm) by physical vapor deposition through shadow mask at a base pressure of 10^{-6} mbar. Sometimes devices were encapsulated inside the glove box using glass coverslip and epoxy resin to increase the stability.

The set of BHJ-PSCs were based on donor type polymers such as P3HT and PCPDTBT [76] blended with acceptor either PCBM macromolecule [142] or P(NDI2OD-

T2), (Polyera ActivInk N2200) polymer [97]. P3HT (98.5% regioregularity) was obtained from Sigma-Aldrich, USA. PCPDTBT was obtained from KONARKA, USA. C_{60} based PCBM was obtained from Sigma-Aldrich. P(NDI2OD-T2) was obtained from Polyera ActivInk, USA.

The typical value of I_{SC} (responsivity) and V_{OC} were in the range of 20-30 mA/W and 0.55-0.6 V respectively in all the solar cells studied. A modified IMPS technique was used for photocurrent measurement. A fast LED (GaN based white LED) was connected to a frequency generator (Tektronix, Model AFG320) and was driven by modulated voltage output. Depending on the DC voltage, LED output (L_{ac}) was controlled not only the intensity but the duty cycle also (Fig. 2.1). For background CW illumination (L_{dc}) an additional white LED was used with a constant voltage source. The CW background intensity was varied from 0 to L_{ac} of the modulated probe intensity.

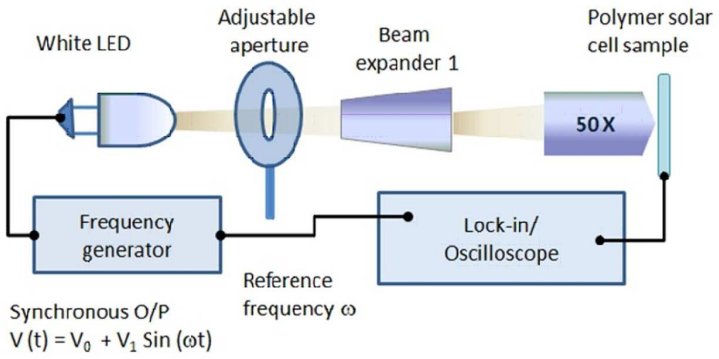

Figure 2.1: *Experimental setup for the intensity modulated photocurrent measurement. White GaN based LED is used as the light source driven by sinusoidal voltage of frequency varying from 10 Hz to 100 kHz. LED intensity depends on the V_0 (1 V) and V_1 (2.0 - 3.0 V). Spot size varies from 160 µm diameter to broad illumination depending on the sample to objective lens distance.*

Modulation frequency of the incident light was varied from 10 Hz to 100 kHz on the logarithmic scale. Optical arrangement was made to increase the intensity

along with a spot size varying from 160 μm to 1.7 mm. However, in general the experiments were done under broad light illumination. The photocurrent was measured either by Lock-in technique (Stanford Research System Inc. Model SR830 DSP) or by an oscilloscope (LeCroy, Model Wave Runner 6100A) as shown in the figure 2.2. Device was fixed on XY translation stage to adjust the position of the

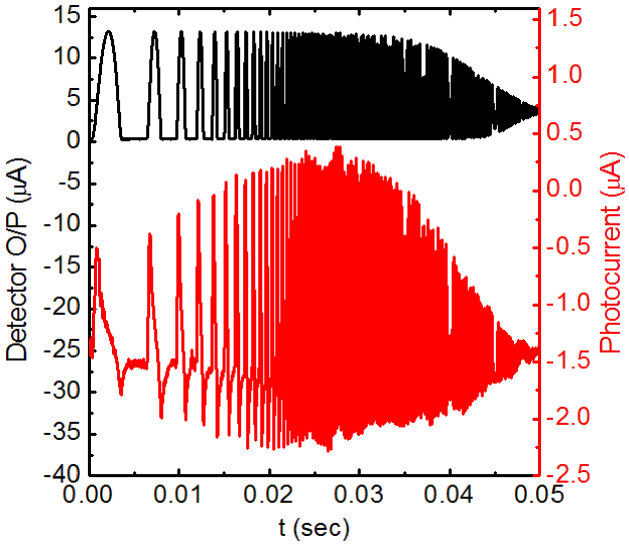

Figure 2.2: *Frequency response of LED and solar cell device. Frequency sweep is done from 100 Hz to 100 kHz. Detector output shows steady response of the LED up to 10 kHz. Bottom red curve is solar cell photocurrent.*

light spot for focused illumination on the overlap region as well as away from one of the electrode. Possibilities of error from the source as well as instruments have been eliminated by measuring average power output for different modulation frequencies [Fig. 2.3(a)] with different types of photodetectors [Fig. 2.3(b).]

A universal photocurrent feature was observed in all polymer solar cells [Fig. 2.4] tested in the laboratory. Light source (L_{ac} ~1 mW/cm^2) incident on the PSCs, was modulated at a frequency ranging from 10 Hz to 100 kHz. Photocurrent response can be classified into three distinct regimes;

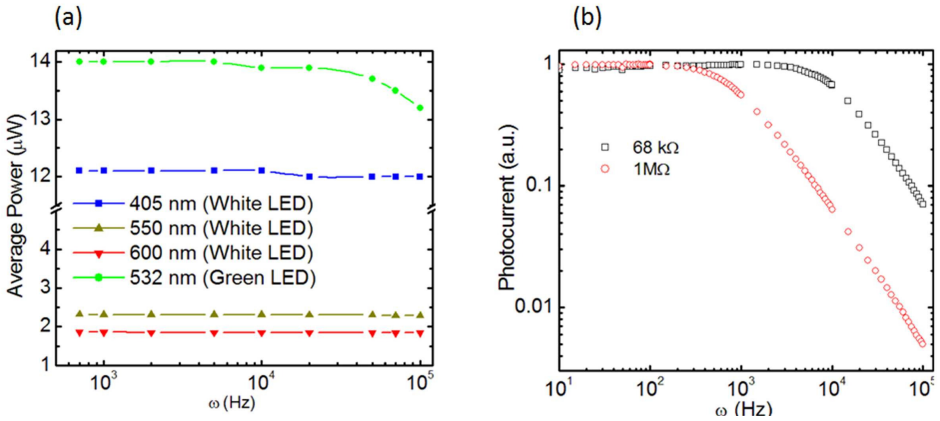

Figure 2.3: *(a) Average power out from two LED sources (White LED & Green LED) was measured by a power meter COHERENT (Model FIELDMASTER) for different wavelength. (b) Modulated photocurrent frequency response of PerkinElmer PMT (Model MP962) detector measured by Stanford Research System (Model SR830 DSP) shows featureless behavior till 10 kHz frequency for smaller resistance value. Resistance of 1 MΩ or 68 kΩ is used across the PMT and the voltage across the load resistance has been measured.*

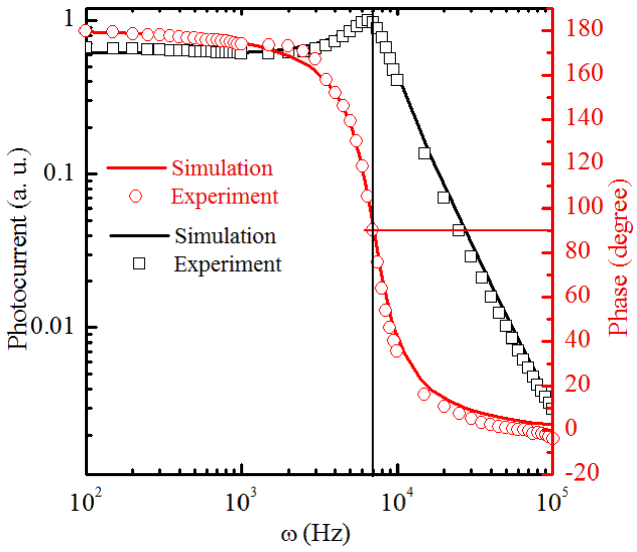

Figure 2.4: *Modulated photocurrent amplitude (□) and phase (○) plot of a P3HT:PCBM devices. Simulation (black line for photocurrent and red line for phase) data matches with the experimental values.*

- $I_{ph}(\omega)$ magnitude marginally changed from the $\omega = 0$ value and was relatively ω-independent at low frequencies (ω<1 kHz).

- For ω>1 kHz, $I_{ph}(\omega)$ increased with ω and a distinct maximum of $I_{ph}(\omega)$ was observed in the range of 5 kHz <ω_{max}<10 kHz.

- Beyond 10 kHz, $I_{ph}(\omega)$ decreased and followed a power-law decay $I_{ph}(\omega) \propto \omega^{-\gamma}$ with an exponent $\gamma \sim$2.

The phase (ϕ) of a typical $I_{ph}(\omega)$ response indicates a singularity ($[d\phi(\omega)/d\omega]_{\omega_{max}} = \infty$) at ω_{max}. Phase component of modulated photocurrent can also be plotted in real and imaginary axis in a cole-cole plot. Modulted photocurrent from a simple RC circuit represented in a cole-cole plot results in semicircle. The cole-cole representation of this data set reveals this feature in the form of a distorted circle. The magnitude of $I_{ph}(\omega)$ scales with probe light intensity and the wavelength (λ). In the entire range of intensity, the ω dependence with respect to these external parameters was preserved for all the efficient devices tested in our laboratory. The uniform presence of the response for all the combinations of donors and acceptors in BHJ-PSCs points to a set of common dominant underlying processes in this class of systems.

The feature of local frequency maxima in the 5 - 10 kHz range was found to be prevalent in all efficient BHJ solar cells for various donor-acceptor compositions. The position (frequency) of local maxima was maintained as the temperature was varied over a wide range (100 K - 300 K). The position of local maxima was maintained for different intensity and wavelength of the modulated light. This interesting universal feature appears to be a characteristic signature of BHJ-PSCs. It is instructive to model the frequency dependent photocurrent response as a product of two independent transfer functions consisting of a circuit component and

a microscopic component. In the next section circuit model as well as microscopic model is introduced and discussed in details.

2.3 Model to describe dynamics in BHJ-PSCs

There have been tremendous efforts to understand the mechanism of charge transport in polymer BHJ solar cells. The processes consist of ultrafast photoabsorption and exciton generation, followed by charge dissociation, geminate and non-geminate recombination, trapping kinetics and charge carrier extraction at the interface. The understanding of each process may be essential to find out the rate limiting processes in the device. Amplitude as well as frequency modulation techniques are useful tools to probe the dynamics and transport of charge carriers. There are several reports on photoinduced absorption where absorption depends on the modulation frequency especially at higher frequencies [143, 144]. Frequency dependent photocurrent is also predicted by Epshtein *et. al.* [145].

2.3.1 Circuit Model

Ideal photovoltaic cells can be represented as a constant current source (I_L) with a diode connected in parallel. However in case of polymer solar cell there are two parasitic resistances [146, 147] R_s and R_{sh} as shown in the Figure 2.5. R_s represents the charge extraction resistance at the polymer electrode interface where as R_{sh} represents the leakage resistance. In case of AC impedance measurement one should take into account bias dependent junction capacitance and frequency as well as bias dependent bulk diffusion capacitance. Combining these two capacitances with a equivalent parallel capacitance C_p the equivalent circuit is modified. The series and shunt resistances may vary from short circuit to open circuit condition. The

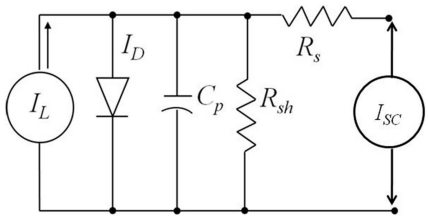

Figure 2.5: *Equivalent circuit diagram of a solar cell. R_s and R_{sh} are two parasitic resistances arising from charge extraction process and leakage current. C_p represents the combination of bulk diffusion capacitance and junction capacitance. I_L and I_{SC} are the photo generated and measured short circuit current respectively.*

measured short circuit current (I_{SC}) can be estimated by solving the circuit model. The circuit transfer function (CTF) takes the form as given the equation 2.1

$$CTF = \frac{I_{SC}(\omega)}{I_L(\omega)} = \frac{R_{sh}}{[R_{sh}R_sC_pi\omega + (R_{sh} + R_s)]} \tag{2.1}$$

Polymer blend is a leaky dielectric with a dielectric constant ~ 3.2 and hence C_p decreases with frequency. From the AC impedance measurement C_p can be modeled as $C/(ai\omega + 1)$ where C represents the geometrical capacitance and a represents the dielectric relaxation time constant. So the CTF is modified as equation 2.2 where $q = R_{sh}/(R_{sh}+ R_s)$

$$CTF = \frac{q(ai\omega + 1)}{[(a + qR_sC)i\omega + 1]} \tag{2.2}$$

The effect of circuit parameters on modulated photocurrent spectrum will be discussed later. The CTF is necessary but not sufficient to describe the origin of photocurrent peak.

2.3.2 Estimation of photo-generated current

Photo generated current I_L can be estimated from the microscopic model of a BJH-device. The basic prevailing microscopic kinetic processes of carrier generation, recombination and charge carrier trapping along with associated rate constants (Fig. 2.6) form the microscopic $I_L(\omega)$. In this model surface recombination rate has been taken as very high compare to other microscopic processes. Experiments were carried out with relatively low intensity light. In this model space charge effect on the extracted current also been neglected for low generation rate, and hence generated photocurrent is proportional to the free carriers present at the polymer electrode interface. Details of the model are discussed bellow. Microscopic

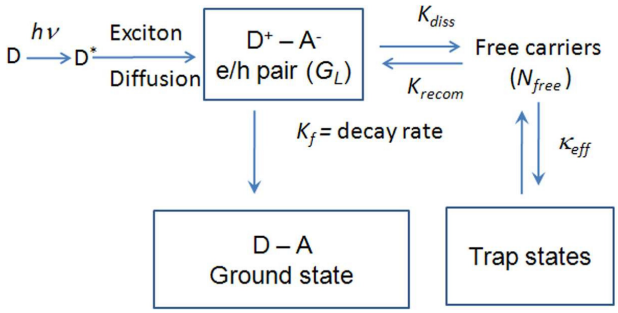

Figure 2.6: *Schematic diagram of microscopic processes involved in an organic solar cell. K_{diss} and K_{recom} are the exciton dissociation rate constant and free carrier recombination rate constant. κ_{eff} represents effective rate of trapping rate constant of the charge carriers to thermally inaccessible states ($\gg$ 25 meV). G_L and N_{free} represent total number of excitons and free carriers at any instant of time.*

processes span over multiple time scales (femto - millisecond). Photon absorption occurs at femto-second scale. So it is almost instantaneous and internal quantum efficiency $\sim$ 100%. However decay of photo generated excitons $g_L(t)$ depends on two processes. Excitons get dissociate at the D-A interfaces, and the rate at which it dissociates is inversely proportional to the average life time of the excitons and proportional to the number of excitons at any instant. At the same time it can

be generated from the free carriers n_{free}(t) at a rate constant K_{recom}. Assuming average life time of the excitons τ_1 we can write decay equation in the form of equation 2.3

$$\frac{dg_L(t)}{dt} = -\frac{g_L(t)}{\tau_1} + K_{recom} n_{free}(t) \tag{2.3}$$

Free charge carrier (n_{free}) can decay through several pathways. One of them is the charge carrier trapping at the deep trap states (>> thermal energy). There will be a significant detrapping. However, overall loss of carrier can be given by the equation 2.4 where κ_{eff} is the effective trapping rate,

$$Q_{trap} = \int \kappa_{eff} n_{free}(t) dt \tag{2.4}$$

So the rate equation of free carriers can be written as shown below.

$$\frac{dn_{free}(t)}{dt} = -\frac{n_{free}}{\tau_2} - K_{diss} g_L(t) - Q_{trap} \tag{2.5}$$

substituting equation 2.4 in the equation 2.5

$$\frac{dn_{free}(t)}{dt} = -\frac{n_{free}(t)}{\tau_2} - K_{diss} g_L(t) - \int \kappa_{eff} n_{free}(t) dt \tag{2.6}$$

Where K_{diss} is the excitons dissociation rate constant and τ_2 is the life time of the free carriers. Combining equations 2.3 and 2.6 the relation between $g_L(t)$ and $n_{free}(t)$ could be written as

$$\frac{d^2 n_{free}(t)}{dt^2} + \frac{1}{\tau_2}\frac{dn_{free}(t)}{dt} + (\kappa_{eff} - K_{recom} K_{diss}) n_{free}(t) = -\frac{K_{diss}}{\tau_1} g_L(t) \tag{2.7}$$

or,

$$K_1 \frac{d^2 n_{free}(t)}{dt^2} + K_2 \frac{dn_{free}(t)}{dt} + n_{free}(t) = -K_3 g_L(t) \tag{2.8}$$

where $K_1 = 1/(\kappa_{eff}\text{-}K_{recom}K_{diss})$,

$K_2 = 1/[\tau_2(\kappa_{eff}\text{-}K_{recom}K_{diss})]$

and $K_3 = K_{diss}/[\tau_1(\kappa_{eff}\text{-}K_{recom}K_{diss})]$.

Equation 2.8 can be written in frequency (ω) domain upon Fourier transformation as shown below

$$N_{free}(\omega) = \frac{-Q}{[-K_1\omega^2 + K_2 i\omega + 1]} G_L(\omega) \tag{2.9}$$

Photogenerated current is proportional to the free carriers and hence equation 2.9 can be rewritten as

$$I_L(\omega) = \frac{P}{[-K_1\omega^2 + K_2 i\omega + 1]} G_L(\omega) \tag{2.10}$$

where P depends on the carrier mobility, exciton life time and exciton dissociation-recombination rate and the trapping kinetics. So the microscopic transfer function (TF) is given by the equation 2.11

$$TF = \frac{P}{[-K_1\omega^2 + K_2 i\omega + 1]} \tag{2.11}$$

The overall transfer function is the product of two transfer functions. Combining equation 2.2 and 2.11 we get a complete transfer function as shown in equation 2.12 apart from the constant.

$$TF_{total} = \frac{(ai\omega + 1)}{[(a + qR_sC)i\omega + 1][-K_1\omega^2 + K_2 i\omega + 1]} \tag{2.12}$$

This expression for TF is utilized to fit the experimental results assuming a set of realistic constants [Table 2.1].

The model fit relies essentially on the two parameters (K_1 and K_2) describing

Table 2.1: *Parameters used for modulated photocurrent simulation for a P3HT:PCBM blend (1:1 by weight ratio) solar cells.*

Parameters	**Value**
Series resistance R_s	800 Ω
Leakage resistance R_{sh}	50 kΩ
Capacitance C_p	38 nF
Dielectric relaxation parameter a	0.0016
Fitting parameter K_1	2.0×10^{-9}
Fitting parameter K_2	9×10^{-5}

the Lorentzian in the denominator and is independent of other variables. It is noticed that the ω_{max} feature is less sensitive to the circuit parameters R_s, R_{sh} and C_p. It should be noted that the proposed model (equation 2.12) can be further validated by solving it in the time domain and comparing it with the experimentally obtained transient $I_{ph}(t)$ for the same set of parameters (K_1 and K_2). The frequency dependent magnitude and phase of the transfer function also agree reasonably well with the experimentally obtained $I_{ph}(\omega)$ magnitude and the corrected phase (ϕ) [Fig. 2.4].

The representation of the complex frequency response largely as Lorentzian transfer function identifies the source for the maximum in $I_{ph}(\omega)$. The analogy with a damped driven oscillator system where the transfer function has a similar form is useful. Photocarrier generation can be taken as a driving term whereas the trapping and recombination terms are the loss mechanisms of the system. Another possible scenario is that the invariant ω_{max} feature can originate from the dimensions, organization and coupling of the nanoscale phase separated regions [Fig. 2.7]. Geometrical factors as a source for a characteristic ω then can also discount the dependence on the external factors.

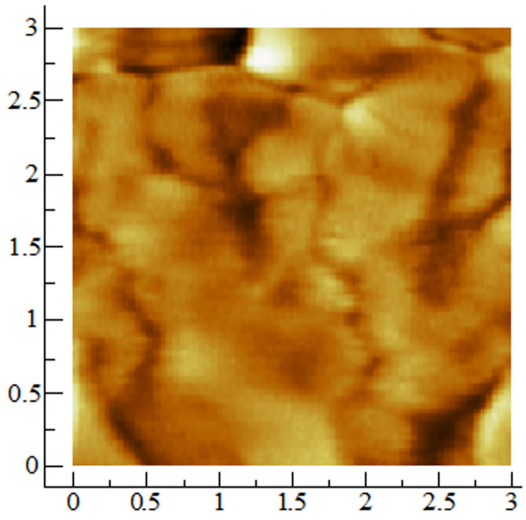

Figure 2.7: *Near field scanning optical microscope (NSOM) image (excitation 532 nm laser) of a P3HT:PCBM (1:1 by weight ratio) blend polymer solar cell. Bright spots represent P3HT rich areas where as dark spots represents P3HT:PCBM blend or only PCBM rich areas. Grain size depends on the annealing condition where over annealing increases the grain size. X and Y scale are in μm.*

2.4 Parameters affecting photocurrent response

In the model it is seen that the photocurrent peak mainly originates from the Lorentzian transfer function $1/[-K_1\omega^2 + K_2 i\omega + 1]$. The other circuit parameters only modify the photocurrent spectrum at low frequency regime. In the simulation the parameters K_1 and K_2 were varied to fit with the experimental data. It is also possible to find out K_1 from the photocurrent maxima where $d|I\omega|/d\omega = 0 \Rightarrow \omega_{max} \approx 1/\sqrt{K_1}$. K_2 is related to the life time τ_2 of the free carriers and the K_1 parameter ($K_2 = K_1/\tau_2$) and it could be solved from the photocurrent value at 0.7 times of its maxima. In the next section the effect of other parameters are discussed in details.

2.4.1 Temperature dependent modulated photocurrent

Temperature (T) dependent modulated photocurrent measurement was carried out to understand the trapping kinetics and its effect on the modulated current. $I_{ph}(\omega)$ decreases in an activated manner as expected [Fig. 2.8]. However the value of the ω_{max} in the response profile remains the same over the entire T range. Figure

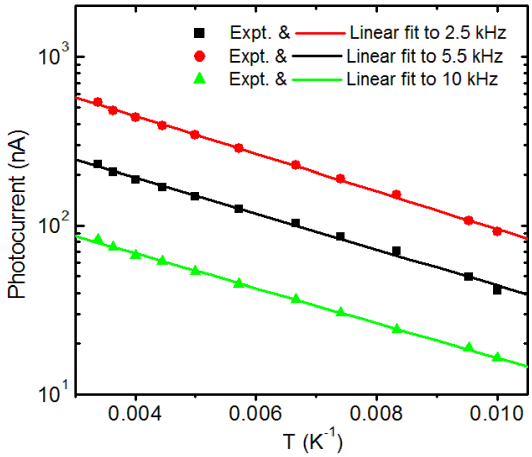

Figure 2.8: *Photocurrent I_{ph} vs T^{-1} plot for three different frequency regime. Estimated activation energy (E_a) is 23 meV*

2.9 depicts the observed temperature dependence of $I_{ph}(\omega)$. This characteristic behavior of ω_{max} with respect to T and modulated light intensity indicates the absence of a single microscopic process as a decisive factor in controlling ω_{max}. If the response originates exclusively from the long-lived relaxation mechanisms related to trap level kinetics then a shift in ω_{max} would be expected as a function of temperature and intensity. This interpretation is also consistent with the constancy of the results for different set of BHJ-interfaces where one expects a large variation in the trap state energetic and distribution.

The circuit component of the transfer function can be used in examining the T dependence closely in the low ω region (ω <1 kHz). In this range $I_{ph}(\omega)$ is

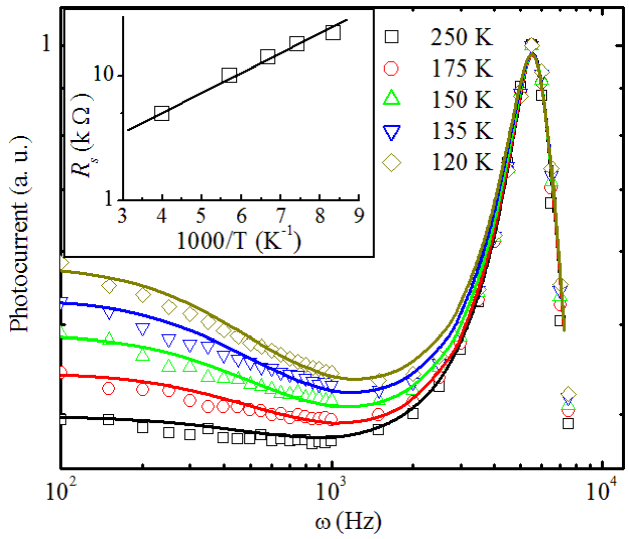

Figure 2.9: *Modulated photocurrent plot with decreasing temperature of a P3HT:PCBM device (symbol for experimental value and lines for simulation with deferent R_s value). Inset: log(R_s) vs T^{-1}*

dependent on T with $dI_{ph}(\omega)/d\omega$ <0 below room temperature. A trap-limited transport model can be used to describe the low ω region (ω <1 kHz), with the trap states exponentially distributed below the band edge. Temperature dependent R_s can take a form R_s=R_0exp[E_a/k_BT] where E_a is the activation energy for the free carriers at the polymer electrode interface. R_s increases from 5 kΩ to 22 kΩ as temperature is lowered from 250 K to 120 K [Table 2.2]. Activation energy E_a is estimated ∼30 meV from the $R_s - T^{-1}$ plot [Fig. 2.9 Inset].

Table 2.2: *Parameters used for modulated photocurrent simulation at different teperature:R_{sh}= 200 k Ω, C_p = 38 nF, a = 0.0016 and K_1 = 3.0 × 10^{-9}.*

Temperature	**Resistance (R_s)**	**Parameter (K_2)**	**life time (τ_2)**
250 K	5 kΩ	6.3 ×10^{-5}	0.48 ms
175 K	10 kΩ	6.4 ×10^{-5}	0.47 ms
150 K	14 kΩ	6.6 ×10^{-5}	0.45 ms
135 K	18 kΩ	6.8 ×10^{-5}	0.44 ms
120 K	22 kΩ	7.0 ×10^{-5}	0.43 ms

2.4.2 Probe light intensity dependence

Intensity modulated photocurrent depends on the probe intensity. Modulated photocurrent $I_{ph}(\omega)$ increases with the increasing L_{ac} as expected. However ω_{max} does not shift much (only a small shift was observed with the increasing intensity as shown in the figure 2.10). The decreasing ω_{max} with the increasing probe intensity can be understood from the recombination kinetics where increasing carrier concentration increases the recombination rate. Hence a small increase in K_1 is expected and photocurrent peak shifts towards low frequency.

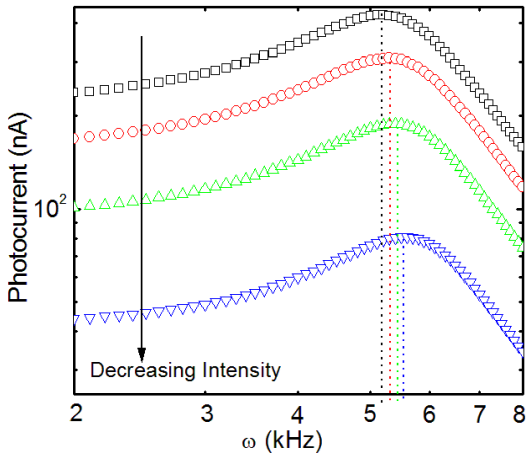

Figure 2.10: *Intensity modulated photocurrent spectrum of a P3HT:PCBM blend polymer solar cell with variable modulated intensity.*

2.4.3 Background continuous wave (CW) white light effect

The presence of CW background light results in a large shift of ω_{max}, with ω_{max} decreasing exponentially with respect to L_{dc}. As L_{dc} is increased to the probe intensity level of $\sim$1 mW/cm^2, ω_{max} decreases from 5.7 kHz to 4.5 kHz and is accompanied by a broadening of the photocurrent peak (Fig. 2.11). The CW excitation alters the trap-site occupancy and increases the carrier density in the trap

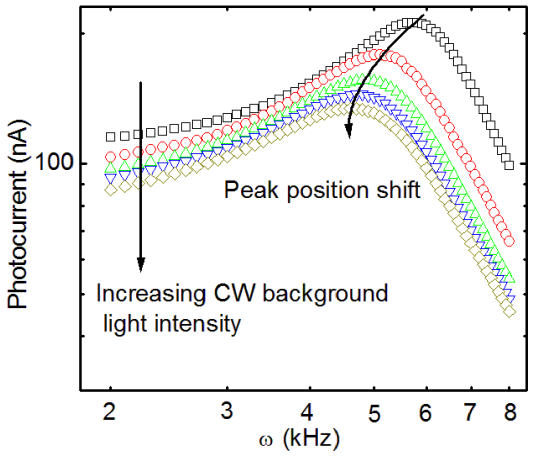

Figure 2.11: *Modulated photocurrent with variable CW background illumination keeping probe intensity constant.*

states (n_t) along with an increase in the recombination rate leading to a decrease in $I_{ph}(\omega)$. An effective increase in K_1 can be physically justified as the K_{recom} term increases along with κ_{eff} decreases, leading to a decrease in ω_{max} as per the expression for $I_{ph}(\omega)$ derived from the microscopic model. In the simulation, K_1 has been varied [Table 2.3] and modulated photocurrent agrees with the experimental value [Fig. 2.12].

Table 2.3: *Parameters used for modulated photocurrent simulation for BHJ polymer solar cells with and without background light:* $R_s = 800\ \Omega$ $R_{sh} = 50\ k\ \Omega$, $C_p = 38$ *nF,* $a = 0.0016$.

Parameters	**No background light**	**No background light**
Parameter K_1	2.8×10^{-9}	4.0×10^{-9}
Parameter K_2	8.2×10^{-5}	12×10^{-5}
Life time τ_2	0.34 ms	0.33 ms

From the impedance plot it is possible to measure the transit time (τ_D) of the free carriers. In the cole-cole plot frequency minima (f_{min} where imaginary component of the photocurrent is minimum) is measured. τ_D ($= 2\pi/f_{min}$) of the free

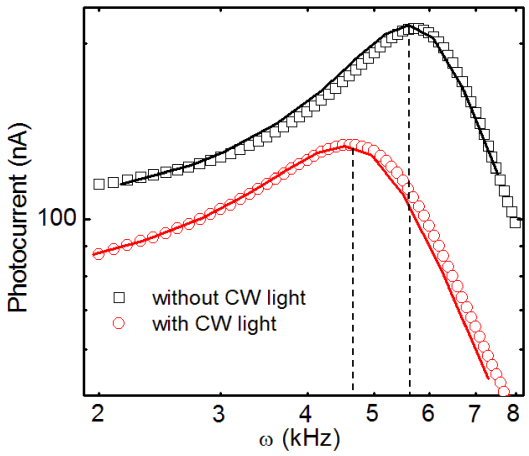

Figure 2.12: *Simulated and experimentally obtained modulated photocurrent for a P3HT:PCBM solar cell with and without background CW light. White LED is used as CW background light source with intensity L_{dc} is same as L_{ac}*

carrier increases with the increasing background CW light. From the impedance plot, [Fig. 2.13] τ_D has been estimated to be 26 μs to 30 μs.

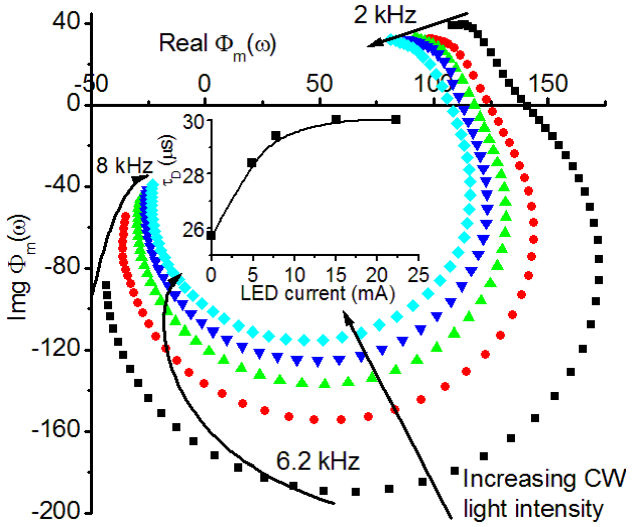

Figure 2.13: *Impedance plot for different back ground light intensity. Inset: The transit time (τ_D) of the carriers for different background light intensity.*

2.4.4 Morphology dependence on modulated photocurrent

The $I_{ph}(\omega)$ trend is also observed to be correlated to the device characteristics. For instance, it is observed that $dI_{ph}(\omega)/d\omega>0$ for low FF devices [Fig. 2.14]. This trend was verified for a large number of low FF devices which can be realized by skewed composition (D:A) ratio, incomplete annealing process, and cathode-BHJ effects [89]. It was noticed that the field dependent exciton dissociation of the charge carriers occurs for the low fill factor devices. On the other hand charge extraction is affected due to the trapped charges at the interface. These localized charge increases the recombination probability and hence a low photocurrent was observed at low frequency range. At high frequency range the deep trap states do not contribute to the modulated current as the detrapping rate is slower compared to measurement time scale.

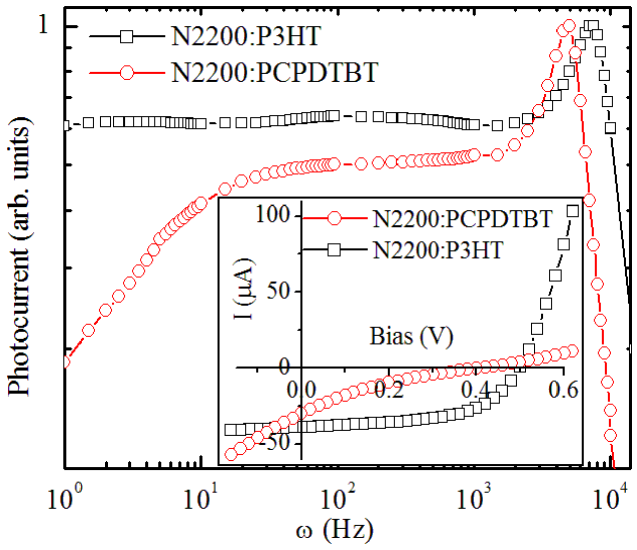

Figure 2.14: *Modulated photocurrent of N2200:P3HT and N2200: PCPDTBT. Inset: light I-V curve for N2200:P3HT and N2200:PCPDTBT showing FF 0.51 and 0.16 respectively.*

2.4.4.1 Beam spot size on modulated photocurrent

IMP was carried out for low efficiency ($\eta < 1\%$) devices, where low frequency photocurrent depends on the intensity of the light probe. The experiment was carried out using a focused light beam spot varying from 160 μm to 1.7 mm by varying objective lenses to sample distance whereas optical power was kept constant [Fig: 2.1]. With higher intensity of light (spot size 160 μm) modulated photocurrent at low frequency was relatively lower than the low intensity light (spot size 1.7 mm) as shown in the figure 2.15. However the relative photocurrent peak position does not shift much. The trapping rate as well as bimolecular recombination increases with the increasing concentration of photogenerated charge carrier, whereas exciton dissociation gets reduced because of reduced built-in field caused by the trapped charge carriers. Bimolecular recombination as well as detrapping of charge carriers is more dominating than trapping when device is under dark. Hence IMP magnitude at higher intensity of light is relatively low at low frequency regime. It is observed that at low frequency regime, IMP of a device with a lower FF depends on the light intensity (Fig 2.14). This result is consistent with the fact that at high intensity of light, FF of a low efficient device is always lower than the FF obtained at low intensity of light illumination.

2.4.4.2 Blend composition (Donor-Acceptor ratio)

Photocurrent peak position depends on the donor-acceptor composition. ω_{max} is minimum for P3HT:PCBM with optimum composition (1:1 by wt.), whereas P3HT:PCBM with 5:2 ratio shows photocurrent peak position at around 10 kHz. Pristine P3HT shows photocurrent peak position beyond 10 kHz (Fig. 2.16). High recombination rate at low frequency results in negligible low photocurrent. The

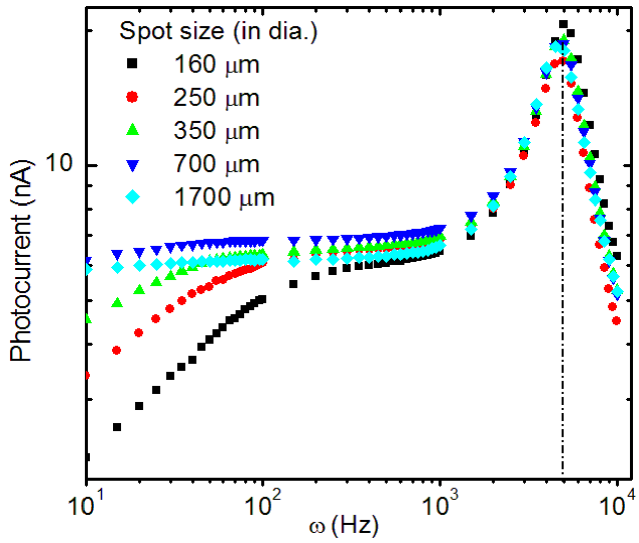

Figure 2.15: *Modulated photocurrent of a low efficient device ($\eta < 1\%$) with different spot size showing same peak photocurrent at same frequency. LED power was kept constant. Device area (9 mm^2) was larger than the beam spot size to avoid any edge effect.*

film morphology gets modified when PCBM is added to P3HT polymer because of spinoidal decomposition [148]. An optimum D-A composition leads to a grain boundary of nanometer scale between two phases. Exciton dissociation rate is much higher in the blend compared to pristine polymer film and higher magnitude of photocurrent is observed (as expected for an efficient solar cell).

2.4.4.3 Spatial dependence

IMP was carried out on P3HT:PCBM based solar cells with a point illumination (spot size 160 μm) scanning over a distance of 200 μm away from one of the electrodes. The photocurrent spectrum depends on the spot position on the devices as shown in the figure 2.17. Active area of a solar cell is defined by the top Al electrode since ITO is presents everywhere. IMP at low frequency is relatively lower when light spot is outside of the Al region. However it was noticed that the

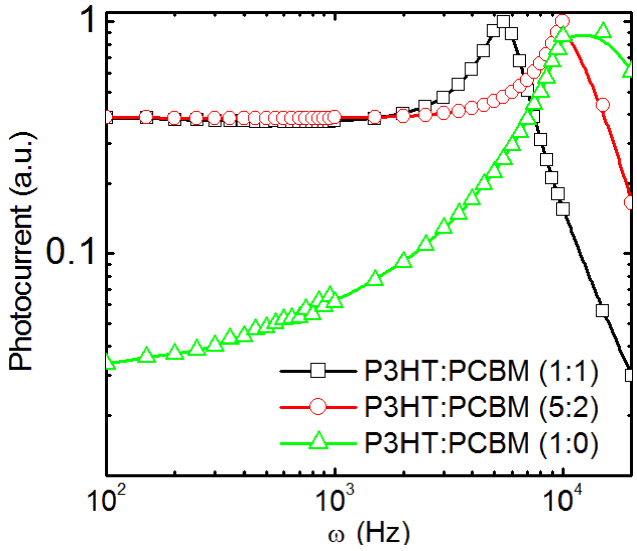

Figure 2.16: *Intensity modulated photocurrent with different ratio of P3HT and PCBM. Optimum composition (P3HT:PCBM :: 1:1 by weight ratio) shows a photocurrent peak at 5.5 kHz where as higher concentration of P3HT (5:2 by weight ratio) and pristine P3HT shows photocurrent peak beyond 10 kHz range.*

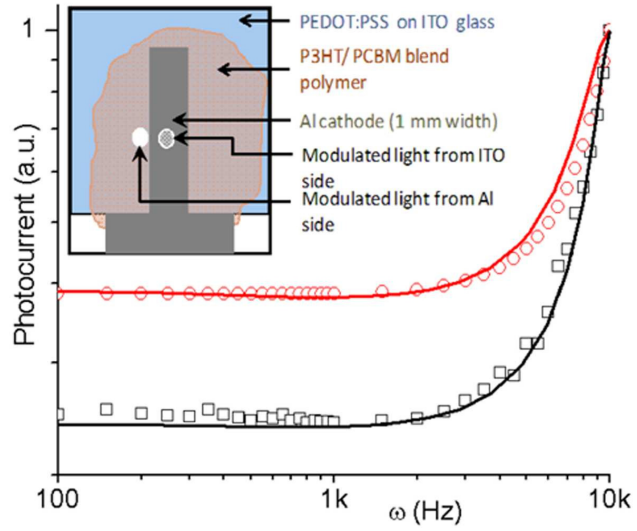

Figure 2.17: *Modulated photocurrent of a low efficiency device (5:2 P3HT:PCBM ratio with η<1) when illuminated on the overlap region (○) and outside region (□). Symbol represents experimental values whereas lines represent model fit.*

peak photocurrent did not change with the light spot position. The transport of electrons is always lateral towards the Al electrode under dark. In the model we have taken care of the shunt resistance as it decreases for high recombination loss under dark condition. Carrier average life time increases (0.25 ms to 0.4 ms from overlap to outside region) possibly due to slower lateral transport.

IMP of BHJ solar cell from different D-A materials was also carried out. The similarity in the form a nanoscale network in all the devices is reflected in the modulated photocurrent spectrum. They all show photocurrent peak in the frequency range of 5-10 kHz (Fig. 2.18(a)). A wavelength dependent study on BHJ-PSCs predicts that the response of the device is independent of the incident photon wavelength (Fig. 2.18(b)).

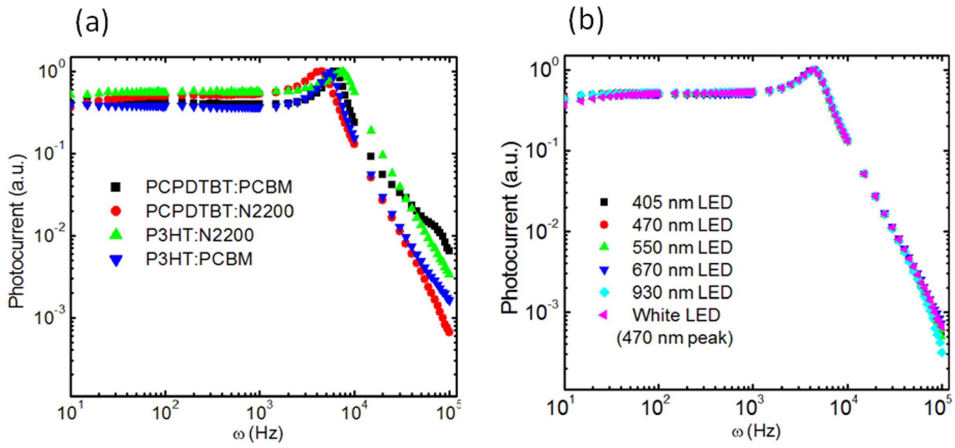

Figure 2.18: *(a) Intensity-modulated photocurrent spectrum from 10 Hz to 100 kHz for PCPDTBT:PCBM, PCPDTBT:N2200, P3HT:N2200 and P3HT:PCBM with a white LED illumination (GaN) driven by a frequency generator. (b) Modulated photocurrent of PCPDTBT:PCBM solar cell under different wavelength of light.*

2.4.5 Intensity modulated photocurrent from other solar cells

Intensity modulated photocurrent measurements were carried out on dye sensitized solar cells (DSSCs) and bilayer solar cells to compare with BHJ-PSCs modulated photocurrent response. It was observed that DSSCs and bilayer devices did not show photocurrent peak at 5-10 kHz frequency range. This gives a clear indication that the origin of photocurrent peak in the BHJ-PSC is the bicontinuous network with nanoscale morphology. In the DSSCs the charge carrier generation happens at the TiO_2 dye interface, whereas electron transport is through the nanostructured TiO_2 film. The slowness of the device comes from the transit time of the electron through the TiO_2 structure and an exponential decay of modulated photocurrent with the increasing frequency of modulated light source is observed (Fig. 2.19).

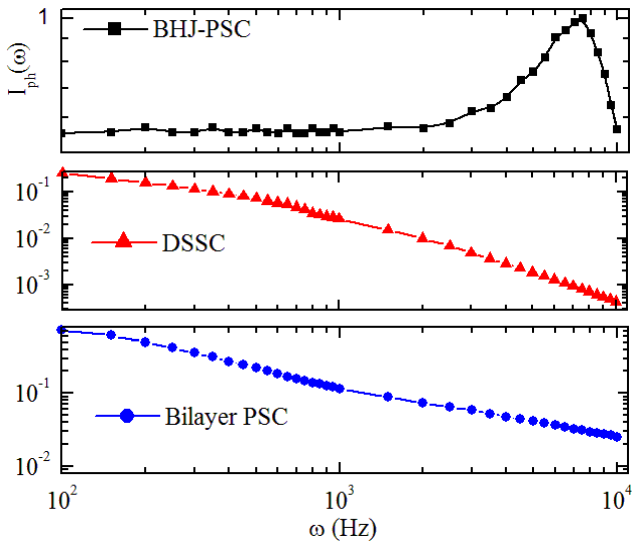

Figure 2.19: *Intensity modulated photocurrent for BHJ-PSC made of P3HT:N2200 (1:1 weight ratio) from chlorobenzene solution, dye-sensitized solar cell made of TiO_2 nano-porous structure coated with N3 dye and I_2 based quasi solid state electrolyte and Bi-layer PSC made of P3HT layer spin casted on ITO glass (20 mg/ml concentration in Chlorobenzene solvent) and PCBM layer on top (20 mg/ml concentration in dichloromethane)*

In case of bilayer solar cells structure, the photocarrier generation occurs largely around the planar D-A interface. The subsequent transport of charge carriers is through the bulk pristine polymers where holes remain in the donor materials and get transported through the donor polymer and electrons transport happens only through the acceptor layer. Hence bimolecular recombination in the bulk is considerably reduced in the bilayer geometry. Both the processes, generation of charge carriers and the transport are then completely decoupled. This set of factors can be the possible reason for the absence of photocurrent peak feature in the intensity modulated photocurrent spectrum of DSSCs and bilayer solar cells. Besides the IMPS measurement, the signature of universal feature in BHJ-PSCs is also then should then be expected to be present in other frequency dependent probe studies. Impedance measurement technique is a proven versatile method in studying variety of dynamical processes in different systems.

2.5 AC Impedance measurement

AC impedance spectroscopy is a tool to understand the devices dynamics when an ac voltage is applied as a function of frequency. With impedance measurement, it is possible to observe electrical properties of a bulk and an interface that we cannot observe by direct current (dc) method. Electrical response of each component is different in microscopic time scale. Impedance spectroscopy is used to study dye-sensitized solar cells [149–151], organic FETs [152] and organics LEDs [153]. However impedance measurement on organic solar cells is not extensively explored. A few research groups have studied the electric properties of the solar cells on the basis of the IS characteristics, providing important information on the exciton dissociation at the D-A interface, charge carrier mobility and carrier lifetime in the

organic active layer [154, 155]. Frequency dependent resistance and capacitance measurement is carried out on a BHJ solar cell. In this section we will see the effect of bias on the capacitance and resistance value under white CW light illumination.

Capacitance of a solar cell arises from the bulk as well from the polymer electrode interface. When a semiconductor forms a junction with and electrode of work function different from the electron affinity of the semiconductor, it forms a space charge layer in the semiconductor giving rise to a space charge capacitance. Capacitance of lossy dielectric materials can be represented as a function of frequency (ω), C(ω) and conductance G(ω). The dielectric loss factor is given by [156]

$$tan\delta = \frac{G(\omega)}{\omega C(\omega)}. \tag{2.13}$$

The geometrical capacitance of a polymer film sandwich between two electrode is $C = (\epsilon_0 \epsilon_r A)/d$ where 'A' is the geometrical area of the device, 'd' is the width of the space charge layer and 'ϵ_r' is the dielectric constant. As reverse bias increases, width 'd' of the space charge layer increases and the resultant capacitance decreases [157]. The slow relaxation of the polymer dielectric gives rise to frequency dependent capacitance as shown in the figure 2.20(a). However Bisquert *et. al.* proposed that the origin of frequency dependent capacitance in a bulk polymer film comes from the distribution of trap states [158]. The time scale associated with the capturing of electron to the trap states and the release of electron from the trap states depends on the energy of the states and the temperature. Strong dependence at high frequency is observed when a forward bias is applied. The loss factor measurement indicates that with the increasing forward bias, loss in the dielectric materials also increases [Fig. 2.20(b)]. Capacitance was also measured under white light illumination. Photoinduced charge carriers at the polymer/electrode interface results in

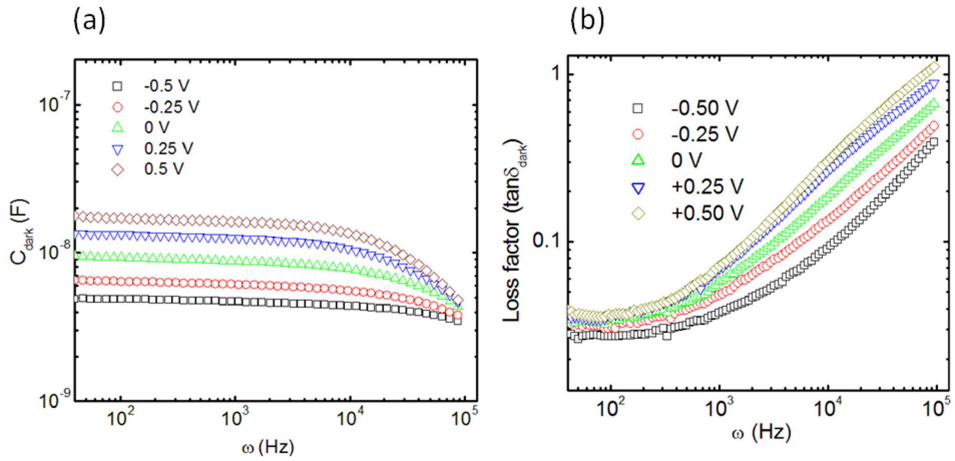

Figure 2.20: *Capacitance and Loss factor (tanδ) of a P3HT:PCBM based solar cells under dark with different bias condition. Both are monotonic function of frequency.*

a higher capacitance value than dark capacitance (Fig. 2.21). Capacitance increase

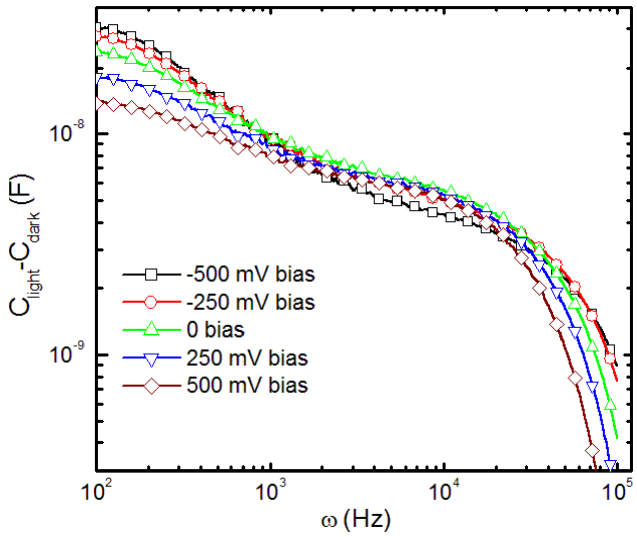

Figure 2.21: $C_{light} - C_{dark}$ *of a P3HT:PCBM based solar cells under different bias condition.*

is more dominating for reverse biased condition than that of forward bias condition. Increased charge dissociation at high reverse bias increases the photocarrier concentration at the interface and the width of the space charge layer decreases.

We observed two time constants associated with the photocapacitance. The loss angle measurement shows an anomalous feature at 3-5 kHz range where loss factor is minimum (Fig. 2.22). Although the origin of such anomalous behavior is not known, the minima at 5 kHz can be attributed to the observed intensity modulated photocurrent peak at that frequency.

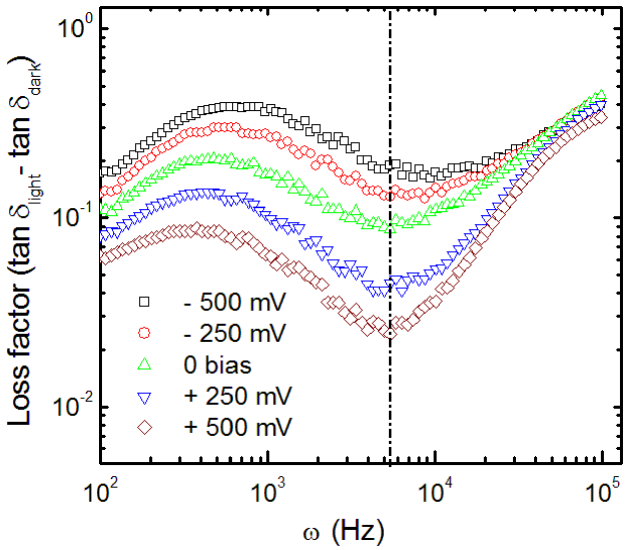

Figure 2.22: *Loss factor ($tan\delta_{light}$-$tan\delta_{light}$) of a P3HT:PCBM based solar cells with different bias condition.*

Device equivalent resistance was calculated from the equation 2.13 for different bias with light and without light (Fig. 2.23). Frequency dependent resistance was also experimentally measured. A simple model of a resistance R_d with a parallel capacitance C_d is used to represent a solar cell impedance. An external resistance R_{ext} ($< R_d/10$) is used to measure current through the device (V_{ext}/R_{ext}). Figure 2.24(a) shows the experimental set up for the resistance measurement. The voltage across the device is calculated from the phasor diagram as shown in the figure 2.24(b) where the applied voltage could be $V_{app} = V_0 + V_1\sin(\omega t)$. The equivalent

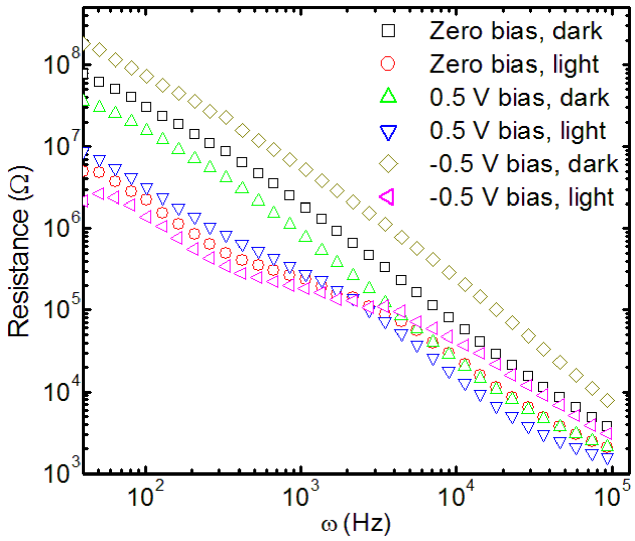

Figure 2.23: *Resistance of a P3HT:PCBM based solar cells under different bias condition. Device equivalent resistance under forward bias is smaller than the reverse bias and it decreases under light illumination. Resistance with different bias shows a crossover around 3-4 kHz frequency when illuminated with a white light source.*

resistance of the device is

$$R_{eq} = \frac{R_d + j\omega C_d R_d}{[1 + (\omega C_d R_d)^2]} \tag{2.14}$$

The estimated current is then V_d/R_{eq}. The measured current has a phase factor (ϕ). Equating capacitive current and resistive current to the measured current we can calculate resistive component as well as capacitive component of the device equivalent circuit. The estimated resistance value is of same order and the frequency dependence of it is also similar to the previous result obtained from the capacitance measurement data. Device resistance at different bias under white light illumination points towards a crossover frequency at 1-2 kHz frequency range. The frequency dependent capacitance and resistance value can be introduced in the circuit model to get a more accurate transfer function in the model to explain $I_{ph}(\omega)$.

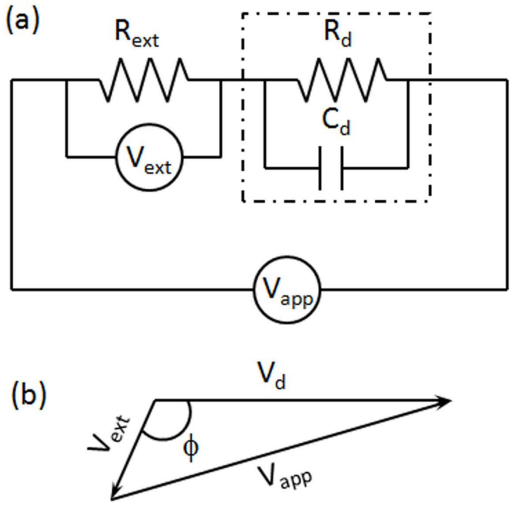

Figure 2.24: *(a) A simple resistance-capacitance model of a solar cell for AC impedance measurement. The external resistance (V_{ext}) is used to measure current through the device. $V_{app} = V_0 + V_1 sin(\omega t)$ is the applied voltage where bias voltage V_0 can be varied from -0.5 V to 0.5 V and $V_1 = 50$ mV (b) Phasor diagram of the circuit showing voltage drop across each component.*

2.6 Summary

Intensity modulated photocurrent is a compact representation of the various photophysical processes observed in the BHJ-PSCs. A universal feature in form of a photocurrent peak in the intensity modulated photocurrent measurement is observed in all polymer BHJ solar cells. Device efficiency depends on the morphology of the film. Intensity modulated photocurrent especially at low frequency regime is related to the morphology of the blend film. Relatively lower photocurrent is observed when the nanoscale phase separation is not optimum. In the I-V measurement also we see a low fill factor. The effect of trap density of trap states and the trapping detrapping rate is observed in background CW light dependent study. Independent study of AC impedance measurement is useful to analyze the modulated photocurrent data. The anomalous behavior of loss factor measurement

under white light illumination indicates a common set of observation that the photocurrent response is maximum at $\sim$ 5 kHz where the loss factor is minimum. Frequency dependent capacitance is used for the circuit analysis model. Thus the device can be well understood by using intensity modulated photocurrent measurement a relatively new, simple and inexpensive measurement technique.

SECTION 3

Photocurrent fluctuations and noise spectroscopy on BHJ solar cells

3.1 Introduction

Electrical signals are inherently accompanied by finite noise in all devices [159] and can be a limiting factor for the device performance [160]. It is important to know the possible sources of noise in such devices to improve the efficiency and performance. In general noise type is classified as (i) Johnson noise or thermal noise, (ii) Shot noise and (iii) Flicker noise (more details in section 3.2). Noise also serves as a valuable tool to investigate the device properties [161], for instance, noise spectroscopy has been used to study the transport properties in semiconductor quantum wires [162, 163], transistors [164] and MOSFETs [165]. Fluctuations in the current density at low temperature in quantum finite systems have been studied. Noise is also expected from light induced current in photodiodes and solar cells. Si based solar cells [166, 167] and Dye sensitized solar cells (DSSCs) [168] exhibit frequency dependent ($1/f^{\gamma}$) noise especially at low frequency (<10 kHz). However there are no reports yet on noise studies of organic bulk heterojunction solar cells. In the present studies, we extract the noise pattern from photocurrent, analyze and interpret the results in terms of the processes within the system.

Another practical reason to study noise is to examine the degradation mech-

anism in organic solar cells. The stability of a polymer based solar cells is a significant issue of concern. Most commonly used technique to study degradation is to study the current-voltage (J-V) under different environment at regular time interval. The decrease in current density with time is reported in several articles. The degradation could be chemical change of the polymer [169], it could be a physical degradation [170] or photodegradation [171]. The degradation of polymer cells can be expressed as the morphological changes with higher density of trap states. In this aspect noise analysis on polymer based solar cells can be a tool to probe the degradation dynamics.

3.2 Types of noise

3.2.1 Johnson Noise

Johnson noise (also known as thermal noise) originates from the thermal agitation of the charge carriers in any electrical circuit. J. B. Johnson was first to analyze this small but detectable fluctuation quantitatively. In 1928, H. Nyquist showed in his paper [172] that the problem of determining the amplitude of the noise was equivalent to summing the energy in the normal modes of electrical oscillation along a shorted transmission line connected to two resistors of resistance R. By the equipartition theory of thermodynamics, every mode contributes to energy of k_BT where k_B is the Boltzmann's constant and T is absolute temperature. If the modes are very closely spaced in a frequency range then the average power in a frequency band df can be written as $dP = k_BTdf$. The r.m.s. voltage evolved in the circuit is given by the equation $dV^2 = dI^2(2R)^2df = 4R^2dP/R = 4Rk_BTdf$. Johnson noise (or thermal noise) is independent of frequency. Thermal noise is present

in almost all electrical components like resistors, capacitors including photodiodes and detectors. However reducing the temperature of the device, thermal noise can be reduced.

> **Some example:** *Johnson noise is mostly observed in resistors and photodiodes. Thermal noise can be reduced by reducing the temperature. Therefore high sensitive detectors (like CCD, APD and PMT) need cooling.*

3.2.2 Shot noise

The current fluctuation in any electrical circuit can be due to the quantization of charge carriers. The magnitude of the current depends on average number of electrons collected, but knowing the average number of electrons which will be collected will not give the actual number collected. The actual number collected will be more than, equal to, or less than the average. Thus the current fluctuates around its mean value. The strength of the fluctuation increases if the current through the device increases. However the increase in signal is more rapid than the increase in noise fluctuation. This follows a Poisson distribution

$$S_I(\lambda, N) = \frac{\lambda^N e^{-\lambda}}{N!} \tag{3.1}$$

where 'N' is the total number of charge carriers contributing to the current.
'λ' is the expected number of carriers.
If the total number of charge carriers is very large, the distribution becomes normal (Gaussian) distribution and signal to noise ratio (SNR) increase as SNR = $\sqrt{N}$. So shot noise is dominated for small N and generally observed in finite systems like quantum wires, quantum dots and diodes at a finite DC current value.

Some example: *Shot noise is mostly observed in finite systems like quantum dots, wires, nanotube transistors, p-n junction diodes etc.*

3.2.3 Flicker noise ($1/f$ noise)

Flicker noise is also known as '$1/f$' noise due to its 1/f frequency dependence. Flicker noise is the centre of attention in the last few decades as it is present in almost all electronic devices. It is also represents the quality and reliability of a device. The origin of flicker noise is still a controversial dispute; some researchers believe that the fluctuation in the mobility of carriers causes $1/f$ noise while others consider the presence of imperfections in the device structure as the predominant source of this type of noise. The fluctuation in a semiconductor is modeled by Hooge

$$S_I(f)/I^2 = \frac{\alpha_H}{fN} \tag{3.2}$$

where '$S_I(f)$' is the fluctuation in the current,

'f' is the frequency,

'N' is the carrier concentration and

'α_H' is the Hooge's parameter,

There could be two sources of fluctuation; (1) fluctuation of carrier concentration and (2) fluctuation of carrier mobility (μ). Hooge's equation holds good for mobility fluctuation. If the carrier concentration fluctuates then Hooge's equation may not hold for a wide range of frequency. Although origin of $1/f$ noise is still not very clear to the community, it is noted that Random Telegraphic Signal (RTS) of a two level system where each level switches rapidly to the other level, shows $1/f$ like power spectrum [159]. Generation-Recombination (GR) is other type of fluctuation where signal does not change rapidly but follow a Gaussian amplitude

distribution in time domain. The power spectrum of RTS and GR is very similar in the sense that they are frequency independent at very low frequency and above a characteristic frequency they follow $1/f^{\gamma}$ where γ is usually accepted to be 0.8 to 1.2. In general the GR centre in the bulk semiconductor gives rise to flicker noise. These centers occupy certain energy level lies within the band gap of the semiconductor. If the energy levels are very close to the Fermi level then carriers can be trapped or detrapped at a given temperature range.

> **Some example:** *Flicker noise or 1/f noise has been observed in photocurrent measurements at room temperature in polycrystalline, amorphous or disordered semiconductor devices like a-Si solar cells, dye-sensitized solar cells. Even though there is no clear explanation to the origin of this behavior the results are similar to the noise features observed in injected current such as that in ZnO nanowires and thin films, and the drain source current in pentacene based thin film transistors.*

In this section the photoinduced current fluctuation observed in solar cells is discussed. The trap-limited transport through the disorder semiconductor results in $1/f^{\gamma}$ type noise spectrum in a-Si solar cells and Dye sensitized solar cells either at reverse bias or short circuit current mode. The distribution of defect states in these semiconductors is typically assumed to be exponential below the band edge. In this present study we carry out these measurements on BHJ-PSCs. The results are analyzed and discussed in the framework of disordered transport model used for BHJ solar cells.

3.3 Photocurrent fluctuation in BHJ solar cell

The origin of current fluctuation in polymer solar cell can be attributed to primarily arising from the kinetic processes like photogeneration, exciton dissociation, charge carrier recombination and transport through the disordered network. The

time scale and resolution of transport fluctuation is controlled by the distribution and occupancy of trap states. The origin of this fluctuation can be traced to the definition of photocurrent, $I_{ph}(t) = \partial Q(t)/\partial t$, where $Q(t) = q < n(t) >$, ($n(t)$ is the charge carrier concentration). A simple analysis can be done by evaluating the number of carriers reaches at a point in a given time. In the figure 3.1, a charge carrier is generated at site i. It can take different path ways to reach site j. The

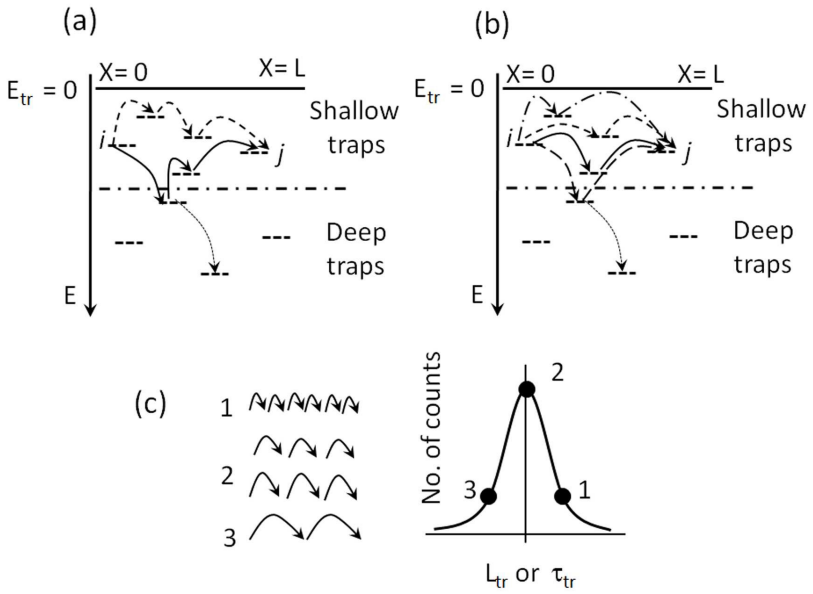

Figure 3.1: *A pictorial schematic to physically depict the source of fluctuation. The energy distribution of localized states is assumed to be Gaussian. The probability of photogenerated carriers to hop from site i to j depends on the energetic and spatial distribution of trap states.(a) carrier from site i can take two path ways to hop thrice before it reaches site j. (b) carrier can take four path ways to hop twice to reach site j. (c) The number of path ways (L_{tr}) or the time taken (τ_{tr}) to reach from site i to j takes a normal distribution for uncorrelated transport.*

time taken by the carrier (τ_{tr}) or the path length (L_{tr}) it travels, takes a form of normal distribution for totally uncorrelated transport. The ensemble average of the free carriers (n) reaching the site j will have time dependent value, that means $< n(t) >$ = constant for $t \Rightarrow \infty$ whereas $< n(t) > \neq$ constant for $t \Rightarrow 0$. The

ensemble average of $< n(t) >$ is essentially a function of temperature, intensity and the trap density of states. The expected noise in BHJ solar cells can be expected to follow a general $1/f^{\gamma}$ response.

3.4 Details of noise measurement in BHJ-PSCs

Bulk heterojunction polymer based solar cells are made with a standard laboratory protocol. Devices are fabricated on indium-tin oxide (ITO) coated glass substrates (20 $\Omega/\Box$). Poly(3,4-ethylenedioxythiophene): poly(styrenesulfonic acid) (PEDOT:PSS) (Baytron P) is spin coated ($\sim$ 80 nm) at 2000 r.p.m for 60 sec on a pre-cleaned ITO coated glass substrate and annealed at 120 °C for 30 min. Donor type polymer poly[N-9'-heptadecanyl-2,7-carbazole-alt-5,5-(4',7'-di-2-thienyl-2',1',3'-benzothiadiazole)] (PCDTBT) blended with 1-(3-methoxycarbonyl)propyl-1-phenyl-[6,6]-methanofullerene (PCBM) in chlorobenzene solvent (20 mg/ml) is spin coated ($\sim$ 100 nm) at 1000 r.p.m. inside glove box (MBRAUN, UNIlab) on PEDOT:PSS layer and cured at 80 °C over which Al (cathode) is thermally deposited at 10^{-6} mbar pressure. Devices are tested in a small vacuum chamber (10^{-2} mbar). Short circuit current fluctuation is measured with LeCroy (Waverunner 6100A,) oscilloscope after amplification with a low noise pre-amp (DLPCA-200, FEMTO Msstechnik GmbH, NEP = 43 fAHz^{-2} at 10^9 gain) with 150 Ω input impedance, AC couple with a gain 10^9, illuminated under tungsten lamp. Since the whole objective is to pick up noise, the typical averaging and filtering stages in the measurement of the short-circuit current is removed. Data was taken without any filter at 4 μs time resolution and consisted of 25k data points for each set. Hundred such sets were recorded. Liquid N_2 was used for low temperature measurements. All the neccessary precautions such as noise from the heating stages and external sources were

eliminated. The light source was powered by a clean DC battery. Pt100 sensor placed in the vicinity of the sample was used along with the device to measure the temperature.Photocurrent fluctuation was also recorded from a Si based detector which served as a standard was used to compare the noise pattern with the BHJ devices. The measurement set up has been shown in the figure 3.2.

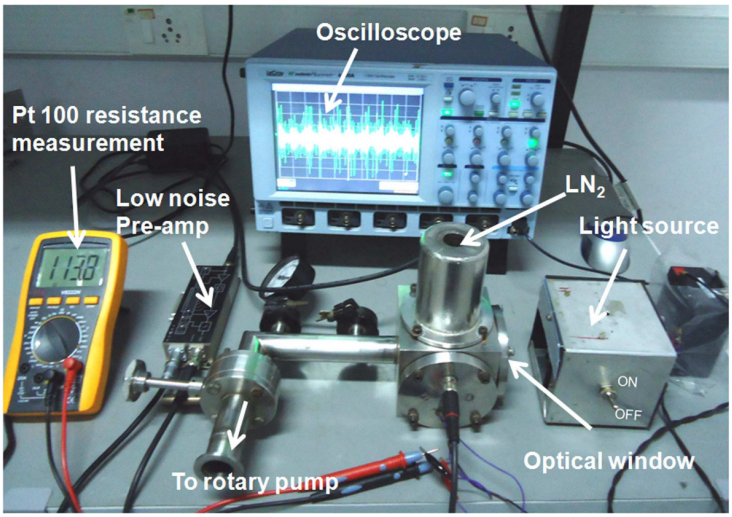

Figure 3.2: *Instruments used for noise measurement showing the vacuum chamber with liquid nitrogen port for low temperature measurement and optical window for white light illumination. 20 Watt tungsten bulb driven by 6 V sealed lead battery (4 AHr) with adjustable gain, multimeter to measure Pt 100 resistance and GHz oscilloscope to measure photocurrent are shown.*

3.5 Results & discussions

3.5.1 Time domain analysis of noise in BHJ-PSCs

The time series profile of the short circuit current in response to steady state white light illumination is shown in the figure 3.3(a). It is to be noted that the DC current was compensated by AC coupling of the digital oscilloscope. The nature

of the amplitude of the fluctuation can take a Normal (Gaussian) distribution or a deviation from it. This form is determined by the probability distribution function derived from normalized fluctuation histogram of the time series data. The most common form of the histogram is obtained by splitting the range of the data into equal-sized bins (called classes), in the figure 3.3(b), bin size = 60. Then for each bin, the number of points from the data set that fall into each bin is counted. A Gaussian fit to the fluctuation histogram was observed for light induced as well as dark current data. A distinct contribution from light induced current fluctuation is clearly observed in figure 3.3(b). In general a Gaussian probability distribution

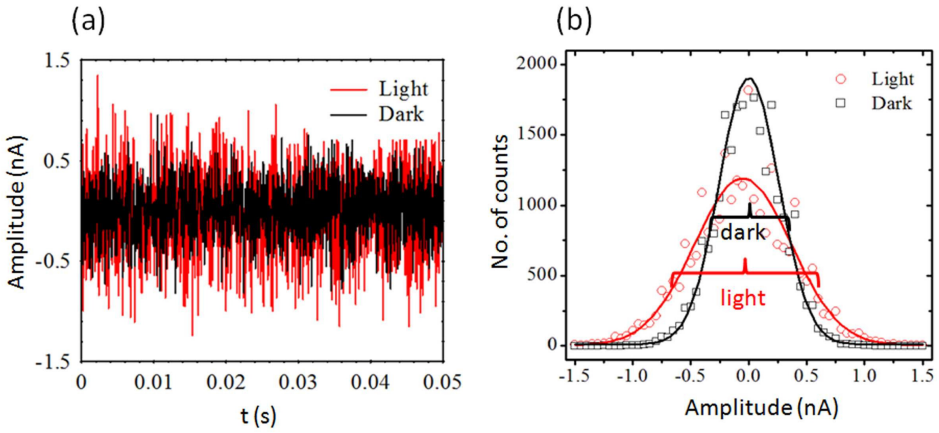

Figure 3.3: *(a)Photocurrent fluctuation in dark and under light with ac couple. Sampling rate 250 kps with an amplifier gain* 10^9*. (b) Amplitude analysis of current fluctuation under dark as wll as under steady state white light illumination.*

of the amplitude in the fluctuations can be expected for uncorrelated transport in a disordered system. However, the deviation from the Gaussian distribution of the fluctuations is observed in many low dimensional systems and finite sized systems such as single wall carbon nanotubes. It has been known that the electrical transport in organic semiconductors with energetic and spatial disorder takes up a process where the charge hopping events are correlated. The transport of

photoinjected charges in disordered organic films is often interpreted using a formula based on a Gaussian disorder model (GDM) that neglects spatial correlations due to charge dipole interactions, even though such correlations have recently been shown to explain the universal electric field dependence observed in these systems [173]. We further analyze the fluctuation of the photocurrent time series in the frequency domain where the trends are more clear and informative.

3.5.2 Frequency domain analysis

It is common practice to characterize noise by its power spectral density (PSD). If the system follows Gaussian fluctuation the spectral analysis would suffice. The variation in random telegraphic signal (RTS) arises from the trapping-detrapping of charge carriers in a single trap model. Previous studies and reports on conventional semiconductor speculate that the individual charge trapping has Lorentzian noise power spectrum and a superposition of many Lorentzian's form the origin of $1/f^{\gamma}$ noise in disorder systems. Since $1/f^{\gamma}$ is a general feature at low frequency which can arise from many factors, in the present study, we emphasize the presence of the additional distinctive feature which appears in the 30-40 kHz regime. PSD was calculated by using fast Fourier transform (FFT) [Fig. 3.4(a)] as given by the equation 3.3 on the time series data. [see Appendix II for detailed procedure].

$$S(k) = \sum_{j=1}^{N} x(j)\omega_N^{(j-1)(k-1)} \tag{3.3}$$

where $\omega_N = e^{(-2\pi i)/N}$. N is the total number of points. Apart from $1/f^{\gamma}$ type behavior at low frequency (below 1 kHz), the power spectra exhibits a Gaussian distribution in the 10 - 100 kHz frequency range. A statistical analysis of the peak

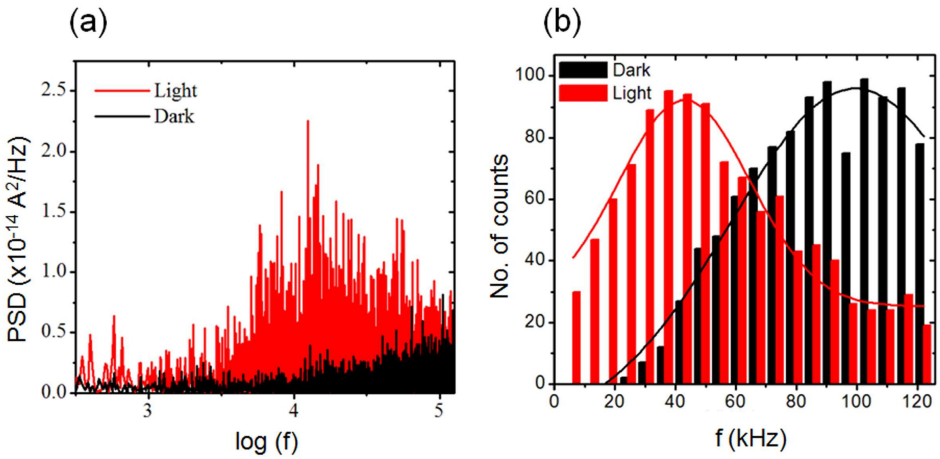

Figure 3.4: *(a) Power spectral density (PSD) of polymer solar cell under white light illumination as well as under dark condition. (b) Gaussian distribution of peak frequency of the PSD spectrum over 1000 files. Black histogram is for the background noise spectrum, whereas red histogram represents the noise spectrum under white light illumination.*

frequency distribution over a 1000 set of data files results in a broad Gaussian distribution median at 30 - 40 kHz. In the figure 3.4(b) the most probable frequency observed is $\sim$ 40 kHz.

The origin of Gaussian distribution of PSD is indicative of characteristic intrinsic processes of the polymer BHJ solar cell. It is known from the studies that the noise spectrum from disordered systems like a-Si solar cells and DSSCs manifest in $1/f^{\gamma}$ type fluctuation. There have been no reports of a local-maximum feature in these systems. The frequency maxima (f_{max}) feature in the present case for polymer BHJs provides a good handle to observe the trends as a function of different external parameters. Three independent experimental parameters were utilized to understand the origin of photocurrent fluctuation; (i) Temperature dependent fluctuation, (ii) Light intensity dependent fluctuation and (iii) device efficiency dependent fluctuation.

3.5.3 Temperature dependent fluctuation

The photocurrent fluctuations were studied at different temperature range (90 K to 318 K). It is noticed that the fluctuation under light increases with the increasing temperature. However background (dark) fluctuation does not exhibit significant variation (Fig. 3.5). At low temperature ($T < 200$ K), the difference between

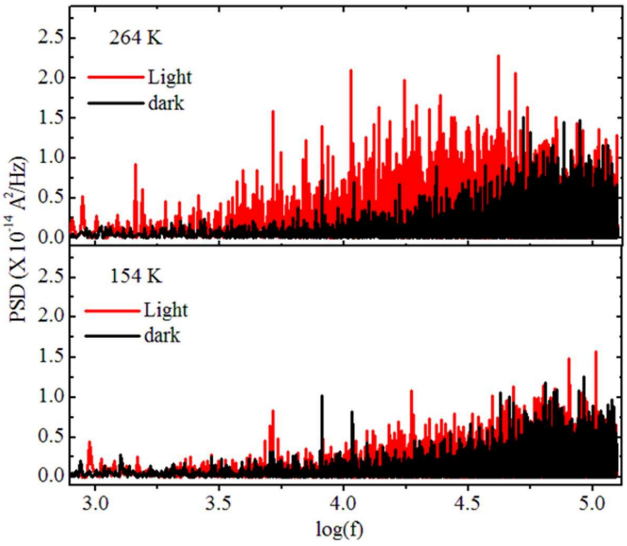

Figure 3.5: *Photocurrent fluctuation under white light illumination (red lines) and under dark (black lines) at 264K and 154K temperature.*

fluctuation in $I_{ph}(t)$ and background gets negligible. At 90 K, light and dark fluctuation merges completely. The decrease in fluctuation of $I_{ph}(t)$ is attributed to factors which lead to trapping and detrapping of the charge carriers. The dc current is constituted only by carriers close to the mobility edge. The results points out that at least as far as fluctuation is concerned, the trap states with activation energy ~ 30 meV, contribute about 30% to the overall $I_{ph}(t)$ at room temperature.

3.5.4 Light intensity dependent fluctuation

For a given disordered semiconductor the trap state occupancy can be varied by the light intensity. The intensity dependence on the trap kinetics is followed by $I_{ph}(t)$. The PSD spectrum shifts towards the high frequency regime as the intensity increases. The amplitude variation also increases with higher light intensity. A high intensity light not only populates the deeper trap states, it also increases the occupied density of trap states near Fermi energy which results in higher fluctuation in amplitude. The width of the fluctuation amplitude and the peak frequency in the PSD spectrum is plotted [Fig. 3.6(b)] against the DC current value which is proportional to the incident light intensity.

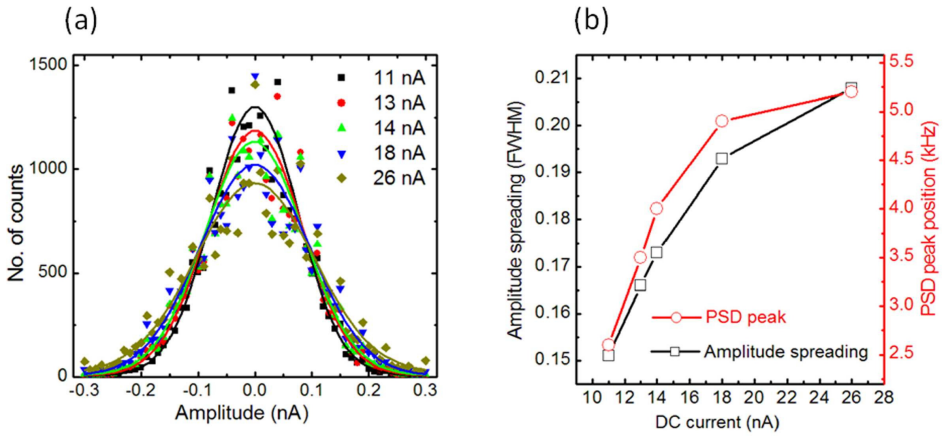

Figure 3.6: *(a) Amplitude analysis with different intensity of light. Amplifier gain was* 10^{10}*. Data is plotted with respect to DC current magnitude as current is proportional to the light intensity at low intensity of light. (b) Peak frequency in the PSD spectrum as well as full width at half maximum (FWHM) of the Gaussian fit to the amplitude is plotted with respect to DC current magnitude.*

3.5.5 Effect of atmospheric degradation (Efficiency dependence)

The photocurrent fluctuation attributed to the trap density of states is sensitive to device efficiency and it can be a probe to analyze degradation in the solar cells. The device was exposed to a white light source (tungsten bulb) in atmospheric condition and the photocurrent measurement was carried out with time over two hours. It was observed that the peak frequency of the PSD is shifted towards the lower frequency magnitude as the device efficiency gradually decreased due to degradation (Fig. 3.7). Degradation manifests as additional trap states. Consequently the density of trap states with the formation of deeper energy level increases. $I_{ph}(t)$ fluctuation due to deep trap states results in shift in PSD spectrum towards low frequency regime.

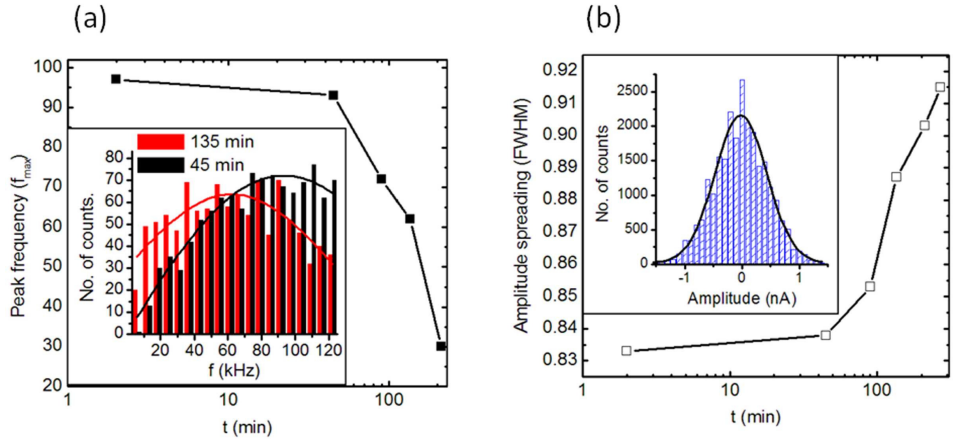

Figure 3.7: *(a)Characteristic frequency peak of a solar cell under white light illumination shifts towards low frequency as the sample gets degraded. Measured I_{ph} decreases from 70 nA to 11 nA after 270 minute exposure to air. Inset: the Gaussian distribution of peak frequency at different time interval. (b) FWHM variation of a Gaussian fit to the current amplitude with time. Inset: Gaussian fit to the current amplitude variation.*

Current fluctuation was also analyzed in different algorithm where averaging over 100 data files are taken after autocorrelation of each file as given by the

equation 3.4 [see Appendix II for more details].

$$X(i) = \sum_{j=0}^{N-1} x(j)x(j+i) \tag{3.4}$$

Discrete Fourier transform of the averaged data is consistence with the earlier results (peak frequency ∼40 kHz in the PSD spectrum). The low frequency response follows $1/f^{\gamma}$ where γ ∼1.44. We have also analyzed the PSD spectrum for a degraded sample over time. γ increases from 1.64 to 1.85 as the device gets degraded with time [Fig. 3.8].

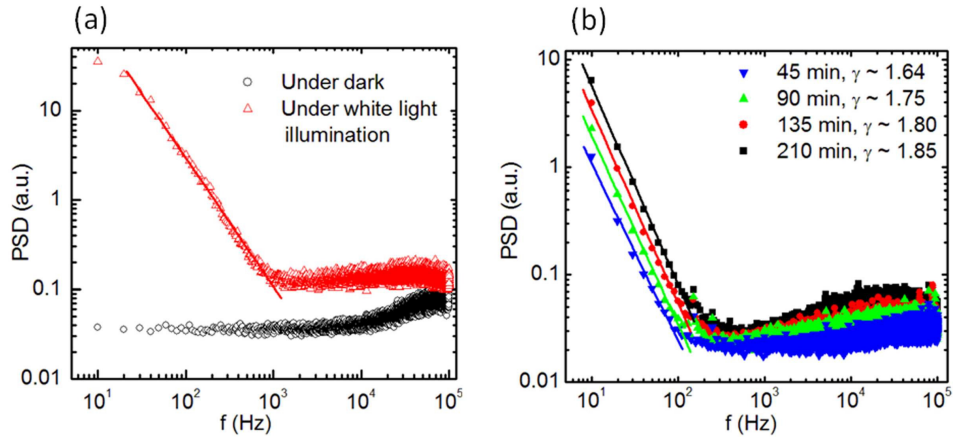

Figure 3.8: *(a) PSD spectrum of a device at room temperature after averaging out autocorrelation of 100 data files. Low frequency (< 1 kHz) follows $1/f^{\gamma}$ where γ ∼1.44 (b) PSD spectrum of a device getting degraded with time. Variation of γ from 1.64 to 1.85 is observed with time.*

In this present study we have observed the $1/f^{\gamma}$ type noise spectrum at low frequency which is expected from a disorder semiconductor device. The appearance of an additional feature at 30-40 kHz frequency range is also observed. A theoretical study has been carried out to understand the origin of photocurrent fluctuation in these devices based on Kinetic Monte Carlo (KMC) approach.

3.6 Kinetic Monte Carlo Method

The Gaussian form of the DOS in random organic system prevents close form of analytical solution of hopping transport. One of the theory available to date that retains both the energetic distribution of hopping sites and the distribution of hopping barriers is the effective medium approach (EMA) developed by Movaghar *et. al.* [174]. Higher order correlation effect appearing when summing over all paths a charge carrier can take on going from site i to site j lead to an effective reduction of the site density after each jump. It has been shown that at finite temperature the EMA provides excellent description of hopping process in disorder materials, but does not have any analytical equation to fit experimental data.

The alternative approach is kinetic Monte Carlo (KMC) simulation. It is similar to an idealized experiment carried out on a sample of arbitrarily adjustable degree of disorder and devoid of any accidental complexity. The KMC can be performed on a cubic lattice, where self energy of each site and interaction energy Γ_{ij} is chosen according to a Gaussian probability density. In this present study we have taken a 3D lattice of order 50×50×200 with 6 Å lattice spacing. The simplest model would be a single charge carrier transport. At the beginning of the simulation, a carrier is generated according to the boundary condition. Since the choice of starting condition may differ, a large number of carriers with different initial condition should be taken to simulate the actual transport. The carrier generated at site i can hop to any one of the all possible neighboring sites. The probability that a carrier will jump from site i to site j is given by the equation

$$P_{ij} = \nu_{ij} / \sum_{i \neq j} \nu_{ij} \tag{3.5}$$

ν_{ij} is the hopping rate as given by the equation 1.1. A random number x_R from a uniform distribution is chosen to specify which site the particle would jump because each site is given a length based on generated number. The time for the jump is determined from the equation

$$t_{ij} = x_{ei}\Big[\sum_{i\neq j}\nu_{ij}\Big]^{-1} \tag{3.6}$$

Here x_{ei} is taken from another exponential distribution of random number. This process repeats until the charge is collected. Flowchart of the model is given below in the figure 3.9.

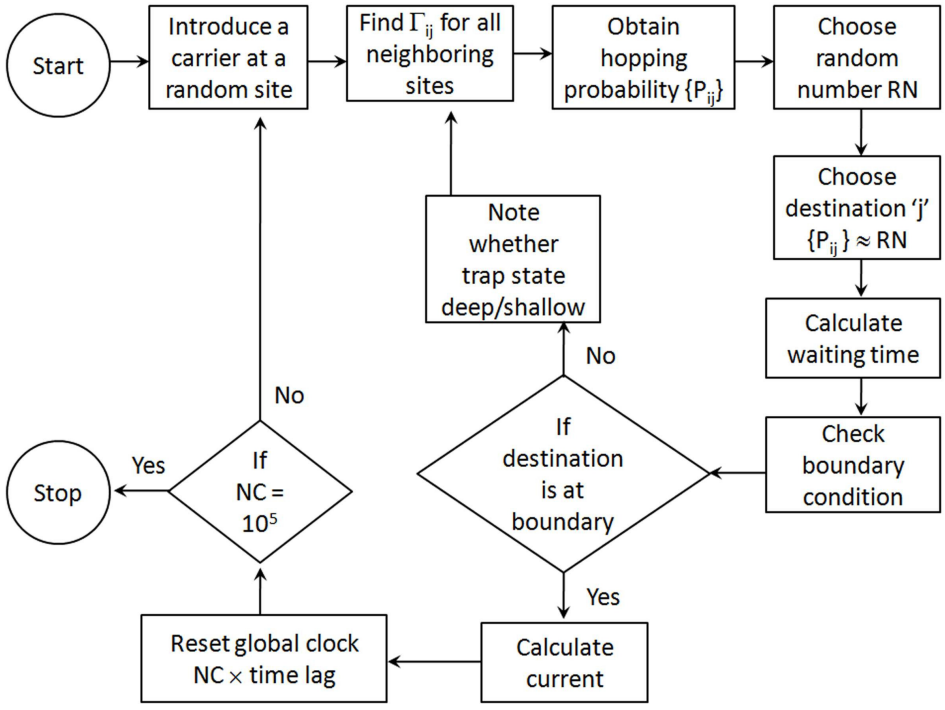

Figure 3.9: *Flowchart of KMC model, Number of carrier (NC) is* 10^5 *generated after each 1* μs *time lag. If the carrier is in deep trap state, then carrier is not counted for current measurement. Maximum number of steps is restricted to 50,000.*

The simulation is based on single carrier model, i.e. all trap states are empty.

This assumption is valid for lower density of charge carriers compared to the trap density of states. We assume a uniform photon flux ($\sim 3 \times 10^{17}$ $cm^{-2}s^{-1}$ for 100 $mWcm^{-2}$ optical power) generates photocarriers at any site in the bulk (~ 1 photon/μs). The width of the Gaussian density of states (σ) is chosen in such way that $\sigma/k_BT \sim 2$ - 4 at room temperature. In this present case the current estimation is different from the conventional KMC simulation approach where integration over all carriers in the system contributes to the current. We propose a model where waiting time for deep trap states are very large compared to the measurement time frame at room temperature and they don't contribute to the current. The energy cutoff below which the carriers are trapped and don't contribute to current can be set accordingly. It is noticed that if the energy cutoff (E_t/k_BT) is far below the transport level, density of deep trap states is very low, hence no fluctuation in $I_{ph}(t)$ is observed. At low temperature, as thermal energy (k_BT) is very small, energy cutoff would be large and negative and hence less fluctuation is expected. In figure 3.10(a) $I_{ph}(t)$ from KMC approach is plotted. The power spectral density (PSD) of current fluctuation estimated from the KMC simulation of a Gaussian disordered model follows $1/f^{\gamma}$ where γ depends on simulation condition and can vary between 1-2 as shown in the figure 3.10(b). Temperature dependent photocurrent fluctuation results are also consistent with the KMC simulation for a given set of disorder configuration parameters. However, a simple Gaussian disorder model does not capture the observed noise spectrum completely in BJH solar cells especially in the frequency regime ($>$ 10 KHz). Additional complexities such as a correlated trap model may need to be introduced to charge transport model through the disordered network. The KMC simulation with these additional input which includes correlated transport of multiple charge carriers in a given disorder configuration should lead to results which are similar to the experimentally observed characteristic noise

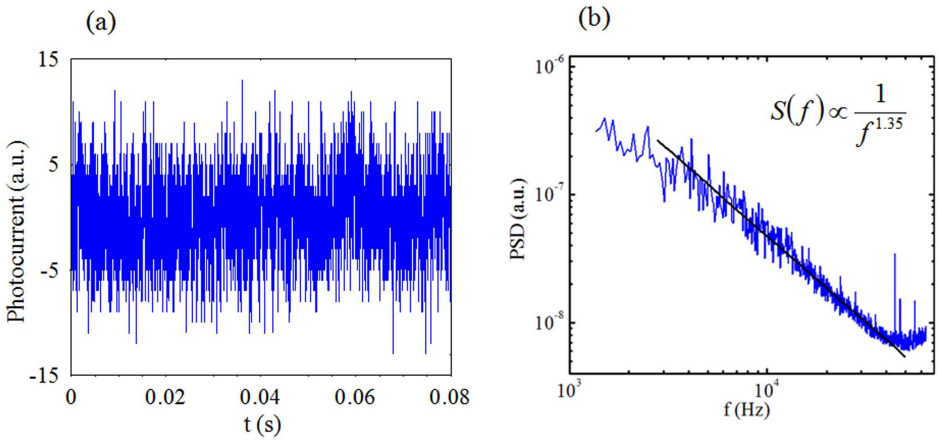

Figure 3.10: *(a) Photocurrent response obtained from KMC simulation. Width of the Gaussian density of states σ = 50 meV. The cutoff energy E_t = -50 meV, temperature = 300 K, number of carriers initially taken 10^5 released at every 1 μs time interval. Current is recorded at 10 μs time step. (b) PSD spectrum obtained from KMC simulation approach averaged over 10 set of data with different disorder configuration.*

features in BHJ solar cells.

3.7 Summary

Fluctuation in the photocurrent of BHJ solar cells provides valuable information in the mechanism and state of the device. Studies carried out as a function of temperature, light intensity and device efficiency, point to consistent trend under the framework of trap limited transport. The overall frequency dependence of the PSD has a $1/f^{\gamma}$ characteristic below 1 kHz frequency regime. Preliminary simulation studies using KMC approach validates the general trends of photocurrent fluctuation observed in BJH devices. The characteristic signature of noise fluctuation in the 30-40 kHz range appears to have origin in the defects prevalent in the active layer. This unique feature observed in case of BHJ-PSCs may represent a

characteristic distribution of the disorder which is correlated.

SECTION 4

Electrical transport studies of low band gap BHJ photodiodes for NIR applications

4.1 Introduction

The advent of interesting molecular systems which have been introduced by organic solar cell research community over the last couple of years include semiconducting donor polymer which have absorption deep into the NIR region (wavelength = 0.8 to 1.2 μm range or bandgap E_g = 1.6 eV to 1.1 eV) [78, 175]. These materials are also promising as the active element for photodetectors in this range. Photodetectors in the optical communication wavelength which corresponds to Er^{3+} transitions from excited state $^4I_{13/2}$ to ground state $^4I_{15/2}$ (in the range of 1.53 μm) [176] are typically made of InGaAs (photodiode type detector with a spectral range 0.7 - 2.6 μm), Ge (Photodiode type, spectral range 0.8 - 1.7 μm), PbS (Photoconductive material with a spectral range 1 - 3.2 μm) and PbSe (Photoconductive type, spectral range 1.5 - 5.2 μm). The availability of polymer semiconductors with advantages for which inorganic materials are not ideally suited; for example, high optical cross-sections, large and ultrafast nonlinear responses, color tunability, large active areas, mechanical flexibility or low-cost processing is important. In fact a tremendous effort has been put to develop inorganic-organic hybrid systems [177, 178] where both material properties have been exploited. Organic materi-

als are used for light source; organic light emitting diodes (OLEDs) [179, 180], organic light emitting transistors (OLETs) [181, 182] and organic semiconductor lasers (OSLs) [183, 184]. Organic materials are also used as transmission media for optical communication such as polymer optical fiber (POFs) [185, 186] made mainly from poly(methyl methacrylate) (PMMA) or perfluorinated (PF) polymers such as poly(perfluorobutenyl vinyl ether) (CYTOP) specially used for short distance transmission. An all optical device with polymer based light source, polymer based waveguides and polymer based photodetctors are ingredients for a complete polymer based optical circuits.

Optical transmitter: *In principle any light source can be an optical transmitter. However most commonly used light sources are the laser diode, light emitting diodes (LEDs) and light emitting transistors (LETs). LEDS and LETs are less expansive, wide spectral range and it emits light in all directions. Since in optical communication system the light source is expected to be collimated, LEDs are inefficient. On the other hand laser diodes are collimated light sources. They have narrow spectral range, high efficiency and they are very expansive. The light intensity is modulated electrically by modulating the forward bias current or mechanically by passing light through a mechanical chopper.*

The external quantum efficiency of organic photo-diode has reached up to 80% in the visible range [187]. Polymers are mostly wide band gap semiconductor and the spectral range mostly varies from 300 nm to 630 nm. To achieve high sensitivity in an organic photodetector device, a common underlying strategy implemented is the utilization of the BHJ concept consisting of an interpenetrating network of electron donor and acceptor materials. Photoexcitation in the vicinity of BHJ results in a charge transfer process between the donor and acceptor species within an ultrafast timescale. The devices are normally tailored to have a graded donor system where efficient energy transfer takes place prior to the charge transfer processes with the acceptor system. The charge carrier transport occurs through the network

of the donor and acceptor to the respective electrodes and the device operated in a reverse bias mode exhibits large responsivity. The pathway to low-bandgap semiconducting polymers [49, 77, 104] with deeper HOMOs has been demonstrated, and BHJ solar cells fabricated by semiconducting polymers with deeper HOMOs have successfully exhibited larger Open circuit voltage (V_{OC}).

Optical fiber communication: *With the development of low loss optical fiber in early 1970's, optical fiber communication became popular almost instantaneously. The wavelength selected for the communication system is either 1310 nm because of its low dispersion or 1550 nm wavelength for the low absorption co-efficient of the silica used as optical fiber cable materials. The core size is reduced to reduce the losses in the fiber. The main advantages of optical fiber communication over electrical communication are low loss high band width signal transmission over a long distance. Background noise is low compared to electrical communication system. There is no cross talk or electromagnetic interference in optical communication and hence can be installed alongside power lines, railway tracks, even highly lightning prone areas.*

Unlike the explosive activity in organic BHJ based solar cells, results from NIR based photodetctors are sparse [188, 189]. In 2009, Gong *et. al.* have reported high detectivity of the polymer photodiode with a spectral range varying from 300 nm to 1450 nm [190]. Apart from the spectral requirement, switching speed and noise equivalent power (NEP) are also important parameters. In the table below typical parameter of a polymer photodiode is listed (adopted from reference [191]).

Optical receiver: *Semiconductor photodetectors are used virtually all in optical communication systems. Two types of detectors are used in optical communication systems; reverse biased photo-detectors and avalanche photo-diodes. In these reverse bias photodetectors, photogenerated carriers are swept out by the reverse bias applied on photodiodes and hence it increases the quantum efficiency. Avalanche photodiode, when it is illuminated with a light source shows a voltage pulse across*

Table 4.1: *Typical parameters table of a polymer photodetector*

Parameter	**Symbol**	**Value**	**Condition**
Peak photosensitivity	S_{max}	0.34 A/W	550 nm, 0V
Ext. quantum efficiency	η	78 %	550 nm, 0V ms
Spectral range	λ	300-630 nm	$S > 10\%$ of S_{max}
Dark current	I_R	< 50 pA/mm^2	$V_R = 10$ mV
Open circuit voltage	V_o	0.55 - 0.95 V	1 mW/mm^2
Short circuit current	I_{sc}	>100 μA/mm^2	1 mW/mm^2

a coupling resistance. The avalanche break down of polymer photodiode at high reverse bias is responsible for the current pulse flowing through a coupling resistance. Avalanche photodiode are more sensitive to the low intensity photons. Generated current or voltage pulse is analyzed by the low noise pre-amp followed by demodulator.

The early process of photoinduced charge carrier generation and separation is quite rapid [52] (in sub-picoseconds regime) in these low band gap polymer photodiodes. Modification of BHJ devices with additives have recently shown to increase the carrier mobility, generation rate as well as free carrier lifetime [192]. The expected photocurrent (I_{ph}) response of these photodiodes should be in the range of nanosecond scale. However, observed transient response from a BHJ photodiode indicate a slow decay with a presence of $I_{ph}(t)$ even at millisecond range [193]. The long-lived $I_{ph}(t)$ is attributed to the presence of large number of trap states. Apart from the explanation of the slow decay in terms of trap kinetics, interpretation in terms of photoinduced gap states are also common. In the well studied model system of P3HT:PCBM, free carrier lifetime ($\tau_e \sim 300$ - 400 ns) [194] strongly depends on the carrier concentration (n) and bimolecular recombination rate (β) [195]. As n increases, τ_e decreases by a factor of $n^{-\alpha}$, where α lies within 0.95 to 1.05. β increases with the increase in carrier mobility (μ), especially of the slower carrier in a BHJ structure. It is expected that at high intensity of light, τ_e

is small enough such that there is no excess charge for storage upon terminating the photoexcitation, which can be indicated by the transient photocurrent rapidly decaying back to dark current magnitude. The electron mobility (μ_e) is higher than hole mobility (μ_h) in P3HT:PCBM system, hence is defined by $q\mu_h/\epsilon$, where ϵ is dielectric constant of the blend material. High mobility of charge carrier may result in high recombination loss and short lifetime and they don't contribute to steady state photocurrent. The ground state interaction between donor-HOMO level to acceptor-LUMO level results in the form of a charge transfer complex (CTC) which have lower energy than individual bandgap energy of each material. Direct excitation of CTC (polaronic absorption) may result in slow dissociation of charge carriers due to low thermal energy (effective free energy for polaron pair dissociation) [196]. Those low energy carriers may get trapped in the bulk and result in slower recombination rate. However, Lee *et. al.* recently demonstrated that the internal quantum yields of carrier photogeneration are similar for both excitons and direct excitation of charge transfer states [197]. The formation of CTC is a function of donor-acceptor ratio, their relative band position and processing condition like solvent assisted and thermal annealing.

In this section we characterize a low band gap polymer based BHJ photodiode in terms of responsivity, spectral sensitivity and response time. Measurements were carried out at low intensity of light at NIR wavelength to address some of the issues related to the long-lived carriers. We also demonstrate the difference of $I_{ph}(t)$ response originating from the CTC states and the photogenerated carriers from the direct excitation of donor polymer.

4.2 Materials & Methods

Low band gap donor type polymer poly [N-9'- heptadecanyl-2,7-carbazole-alt-5,5-(4',7'-di-2-thienyl-2',1',3'- benzothiadiazole)] (PCPDTBT) was used for photodetector. The band gap of these materials is around 1.5 eV with HOMO at 5.3 eV and LUMO ant 3.6 eV. It was blended with the acceptor materials such as [6,6]-phenyl-C_{61}-butyric acid methyl ester (PCBM) or C70 based PCBM. The device fabrication was done following a standard protocol of a bulk heterojunction polymer solar cell as mentioned in section 2.2. Devices were encapsulated inside a glove box (O_2 and H_2O contain <1 ppm.) by a cover slip/glass and epoxy resin. The transient measurements were carried at room temperature as well as at low temperature inside a liquid He based cryostat chamber. A 10 ns laser (EL FORLIGHT Ltd, UK) pulse was used for photoexcitation and the transient responses were recorded by a GHz (LeCroy, Model Wave Runner 6100A) oscilloscope. A ultra-fast ($<1\mu$s rise time) blue LED (470 nm) and a NIR LED (930 nm) driven by a function generator (Tektronix, Model AFG320) was used for longer duration of pulse (1 ms ON time at 100 Hz repetition). Agilent source meter was used to apply reverse bias in steps of 100 mV.

4.3 Characterization of polymer photodiode

The transient photocurrent measurement gives an opportunity to understand some of the loss mechanism. One of the most common technique is photoinduced charge extraction by linearly increasing voltage (photo-CELIV) where a ns light pulse is used followed by a ramp voltage to extract photogenerated carriers [198]. Durrant and co-workers have developed a number of transient techniques to determine the charge carrier density and carrier dynamics at V_{OC} [199, 200]. McNeill *et. al.*

[193] have reported the effect of trapping and detrapping of charge carriers on the transient response. In these studies the photocurrent response of a device to a step function of an optical excitation is analyzed. The time duration of the optical pulse is very important to understand the dynamics of charge carriers at steady state as well as under transient condition. For a longer duration of pulse a steady state condition can be established. This technique was previously used to study the response time of a detector. Apparently the switching speed of a detector depends on the transient response (rise time as well as decay time) under optical excitation. In this section we shall discuss the steady state response as well as transient response of a photodetector.

4.3.1 Steady state measurement

Steady state measurements were carried out to estimate the spectral sensitivity, quantum efficiency, detectivity and the stability of the devices. Spectral sensitivity has been recorded by a monochromator (Spectromax, 500M) and a Xe lamp source [Fig. 4.1]. The spectral sensitivity of these devices shows a significant response up to 800 nm ($\sim$ 80 mA/W) with a peak response at 775 nm ($\sim$ 110 mA/W). A discernible and measurable I_{ph} exists deep into 1 μm. The use of C70 based PCBM also enhances the external quantum efficiency (EQE) of the detector as predicted by Boland *et. al.* [111]. These devices were stable at inert atmosphere. Encapsulated device showed significant response (>80%) even after several weeks. However exposure to UV light may reduce the efficiency due to photo-degradation [201]. The performance of the device could also be gauged by the adequate response ($\sim$ mA/W) to commercial LED light source operating at 930 nm which is typically used in remote control applications.

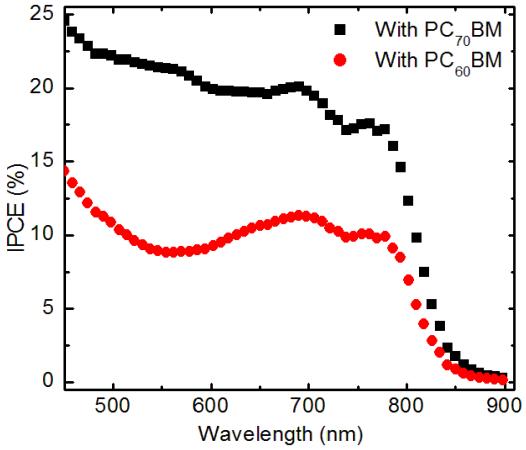

Figure 4.1: *IPCE spectrum is measured for PCPDTBT:PC60BM and PCPDTBT:PC70BM of 1:2 by weight ratio is shown. Xenon arc lamp is used as a white light source and Spectromax 500M is used as monochromator.*

Photosensitivity *The definition of photosensitivity can be of two types, it could be either device specific or material specific. The change is photoconductivity ($\Delta\sigma$) is high for some detectors, however the change in $\Delta\sigma/\sigma_0$ is more materials specific where σ_0 is the dark conductivity. The photosensitivity can be defined as*

- ***Specific Sensitivity:*** *Specific Sensitivity is a measure of the materials actual sensitivity in terms of mobility-life time ($\mu\tau$) product. This is applicable for large photosignal*

$$S^* = \Delta I d^2/\phi P m^{-2}\Omega^{-1}W^{-1} \tag{4.1}$$

  where P is the optical power input, ϕ is the applied voltage across a film thickness d and ΔI is the change in photocurrent.

- ***Detectivity:*** *This is usually applied to the low signal measurement where the photoexcited signal is measured in presence of background noise.*

$$D^* = (A\Delta\nu)^{1/2}NEP \tag{4.2}$$

  where A is the device active area, $\Delta\nu$ is the bandwidth used for measurement of noise and NEP represents the radiation power needed to produce a signal equal to noise.

- ***Photoconductivity gain:*** *Its a combination of photosensitivity and device parameters defined as the number of charge collected in the external circuit to the number of incident photon. If F is the*

total number of photon absorbed then the gain G^* is expressed as

$$G^* = (\Delta I/q)/F \tag{4.3}$$

where q is the elementary charge.

4.3.2 Transient measurement

Photocurrent transient analysis is necessary to estimate the speed of the detectors. The speed of response is inversely proportional to the rise time and decay time of the detector. The time constants not only depend on the life time of the free carriers but it depends on the density of trap states also. The speed of response decreases with the increasing density of trap states. In presence of trap states additional time dependent phenomenon occurs in terms of trap filling during photoexcitation, whereas detrapping happens with a slower rate when light is off. So the measured response time $\tau_0 = \tau(1 + n_t/n)$ (n_t is the trap density of states) can be greater or equal to the life time of the free carrier.

Rise time and fall time: *Rise time and fall time of a detector is related to the life time of the free carriers (n).*

- ***Rise time :*** *It is the time taken by output signal to reach from a specific low threshold value (generally 10%) to a specific high threshold value (90%).*
- ***Fall time / Decay time :*** *The time taken by the output signal to decay from a specific high threshold value to a specific low threshold value.*

If the generation rate is G and life time of the free carrier is τ_e the simple rate equation will be

$$\frac{dn}{dt} = G - \frac{n}{\tau_e} \tag{4.4}$$

At steady state $n = G\tau_e$. The rise time can be derived from the equation

$$n(t) = G\tau_e[1 - exp(-t/\tau_e)] \tag{4.5}$$

and the decay time can be derived from the equation

$$n(t) = G\tau_e exp(-t/\tau_e) \tag{4.6}$$

4.3.2.1 Temperature dependent transient response

The temperature (T) dependence of transient $I_{ph}(t)$ was carried using a liquid He based cryostat chamber. Short laser pulse (532 nm, 10 ns pulse at 10 kHz repetition) was used for photoexcitation and the transient responses (across 1 MΩ coupling) were recorded by a GHz (LeCroy, Model Wave Runner 6100A) oscilloscope. The magnitude of the photocurrent $I_{ph}(t)$ decreases with decreasing T as shown in the figure 4.2. The $\log(I_{ph})$ Vs. T^{-1} exhibited an activation energy $\sim$ 16 meV. The activated response is also reflected in a similar dependence of the decay time constant of $I_{ph}(t)$. The transient photocurrent decay can be reasonably modeled to a single exponential function [202] in the temperature range 200 - 300 K,

$$I(t) = A\mu_e\tau_e e_e n_t exp(-e_e t) \tag{4.7}$$

where 'A' is a constant that depends on the electric field, illuminated surface on the electrode and the penetration depth of light, 'e_e' is the trapped carrier emission rate, 'μ_e' is the carrier mobility and 'n_t' is the density of occupied trap states under light illumination. The carrier emission rate $e_e = (\tau^{-1}) = \nu_0 exp(-\varepsilon_a/k_B T)$ depends on the activation energy ε_a and the temperature T. Here ν_0 is the attempt to escape frequency [203, 204]. The dynamics represented by time constant τ estimated at different T takes on a characteristic form. At $T > 350$ K, τ is $\sim$ 1.35 μs and at

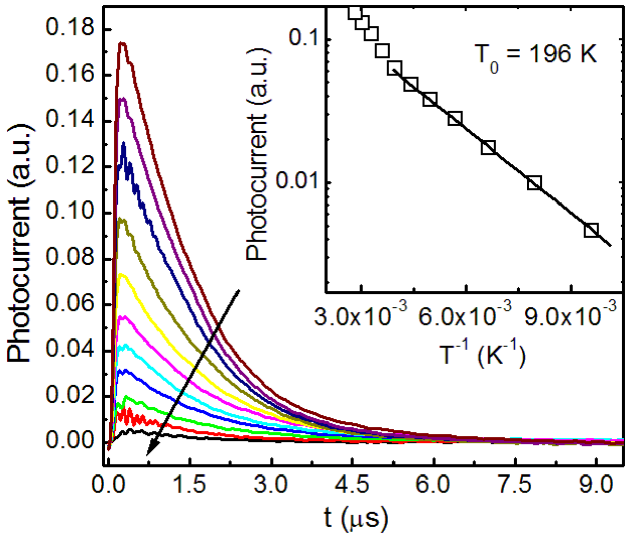

Figure 4.2: *Transient response of a BHJ polymer photodiode at different temperature range. 532 nm Laser (10 ns pulse at 10 kHz) is used. Photocurrent response decreases with the decrease in temperature (arrow indicates the decrease in temperature). Inset: log (I) vs. T^{-1} plot. Estimated activation energy at low temperature is 16 meV and at room temperature it increases to 30 meV.*

$T \sim 200$ K, τ increases to $\sim$1.65 μs. It was observed for $T < 200$ K that the measured transient $I_{ph}(t)$ takes on a biexponential decay with an appearance of an additional distinct slow time constant [Fig. 4.3(a)]. Both the components (τ_1) and (τ_2) continue to decrease upon lowering T, as indicated by the value of $\tau_1 \sim 1.1$ μs, and $\tau_2 \sim 4.7$ μs at $T \approx 125$ K. The origin of the anomalous behavior of transient photocurrent response can be attributed to the existence of different transport mechanisms operative at different T regime. At lower temperature ($T < T_0$), variable range hopping (VRH) [17, 205, 206] is dominating transport mechanism where the density of localized states near Fermi energy contributes to the transport. As temperature decreases, the activation energy also decreases as it follows $T^{3/4}$ dependence [207]. However, above a certain temperature ($T > T_0$), a band like nearest neighbor hopping (NNH) is possible where the activation energy is constant.

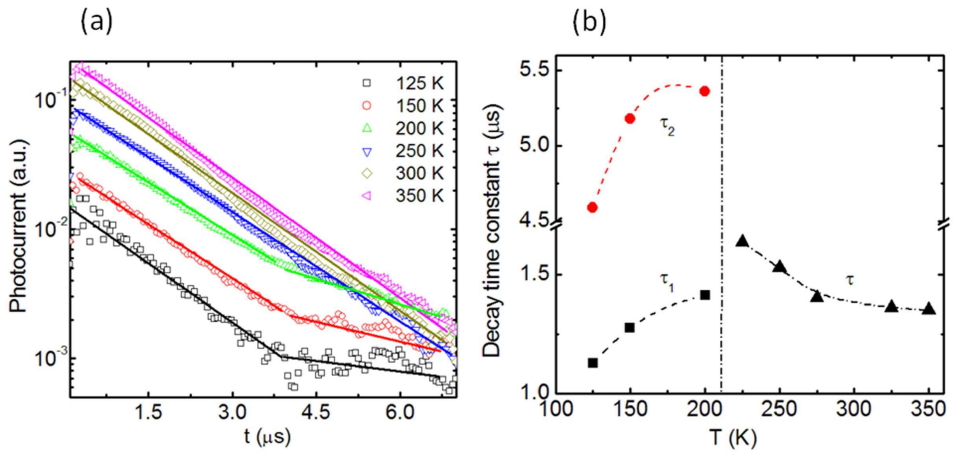

Figure 4.3: *(a) log(I) vs. t plot at different temperature. Above 200 K, transient photocurrent follows single exponential decay. Below this temperature the response shows multi-exponential decay. (b) Single exponential decay time constant for temperature > 200 K and biexponential fitting for a temperature range below 200 K.*

Detrapping rate increases with the increasing temperature hence τ decreases. If the transient dependence can be profiled by $\tau(T)$ then at $T = 200$ K, a crossover in the $\tau(T)$ is observed where both mechanism could be present to some extent giving rise to slowest response of the device as shown in the figure 4.3(b).

4.3.2.2 Bias dependent transient response

Ultra-fast (< 1 μs rise time) blue LED (470 nm) and a NIR LED (930 nm) driven by a function generator was used as a light source. Agilent source meter was used to apply reverse bias in steps of 100 mV. In order to study the slow processes a 1 ms pulsed LED at 100 Hz frequency was used. Transient response was measured at different reverse bias voltage [Fig. 4.4]. As the reverse bias ($E = V/d$) increases, mobility (μ) of the free carrier increases, subsequently the rise time of the current pulse decreases. The responsivity increases linearly with the increasing reverse bias as shown in the figure 4 inset. A simplified model based on the dynamics of

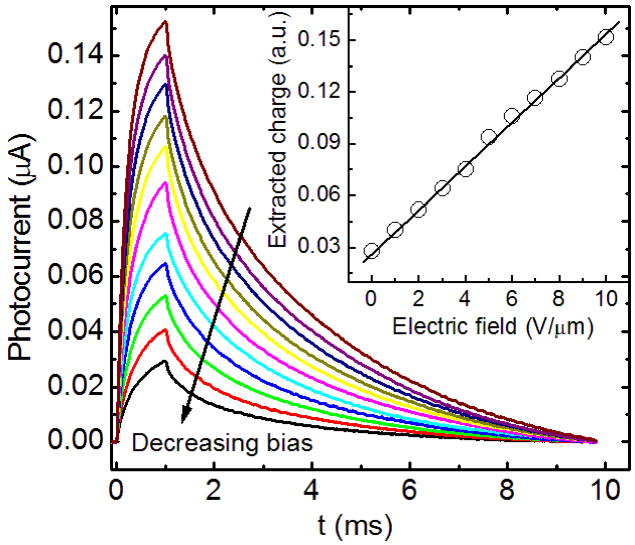

Figure 4.4: *100 nm thick device transient response under reverse bias (0 to 1000 mV). IR LED (930 nm) is used with a 1 ms pulse and 100 Hz frequency. Inset: Extracted charge linearly increases with the electric field.*

trapping and detrapping of electrons is used to explain the bias dependent response. A localized state at an energy ε measured from the bottom of the conduction band is characterized by a density of states $M(\varepsilon)$ and the occupied density of state is $m(\varepsilon)$. If the generation rate is $n_i(t)$, the rate equation for the trap density of state [127] as shown in the equation below

$$\frac{dm(\varepsilon)}{dt} = n_i(t)[M(\varepsilon) - m(\varepsilon)]v\sigma - N_c v\sigma m(\varepsilon)exp(-\varepsilon/k_BT) \tag{4.8}$$

Here 'v' is the thermal velocity of the carrier, 'σ' is the capture cross section and 'N_c' is the effective density of state in the conduction band. So the rate equation for the electrons in conduction band can be rewritten as

$$\frac{dn(t)}{dt} = n_i(t) - \int_0^{\varepsilon_d} \frac{dm(\varepsilon)}{dt} d\varepsilon - \frac{n(t) - n_d}{\tau_R} \tag{4.9}$$

where 'n_d' is the dark carrier density. 'τ_R' is the recombination rate. 'ε_d' represents the electron demarcation level above which conduction band interacts with the localized states. In this case the generation rate $n_i(t) = n_0[U(t) - U(t - T_{ON})]$ where $U(t)$ is a unit step function. The first term in the equation 4.8 represents the trapping rate present only when the light pulse is ON, and second term represents the detrapping of the charge carriers mostly dominating when light pulse is OFF. Generation of charge carrier is bias independent [208], but the traping-detraping kinetics strongly depend on bias. With the increasing reverse bias the barrier height ε will get reduced by $qE.R$ where 'R' is the distance between two hopping site. It is expected from the equation 4.8 that the trapped carrier density $m(\varepsilon)$ increases with the increasing light intensity as well as light pulse (T_{ON}) and trapping-detrapping rate gets equilibrated to a steady state value. In case of a short light pulse, the trapping and detrapping rate does not reach to equilibrium state as shown in the figure 4.5 and hence a weak bias dependent photocurrent is observed. The distribution of trap states is also very important to determine the I_{ph} and τ as deeper states contribute to the transient current when light pulse width is increased. It is seen that τ for a 10 ns pulse excitation ($\tau \sim$ 1-2 μs) is much smaller than τ for 10 μs pulse excitation ($\sim$ 30-40 μs) whereas τ for 1 ms pulse excitation is of the order of ms.

4.3.2.3 Incident photon wavelength and background light dependence

The wavelength dependence of the detector specifications is clearly brought out by the analyzing the device response to 470 nm blue LED and 930 nm IR LED which were driven to generate a 1 ms pulse and 100 Hz frequency as shown in the figure 4.6. It was observed that the response time of the device to blue light (470 nm) pulse was clearly shorter than the IR light (930 nm) pulse as shown in the

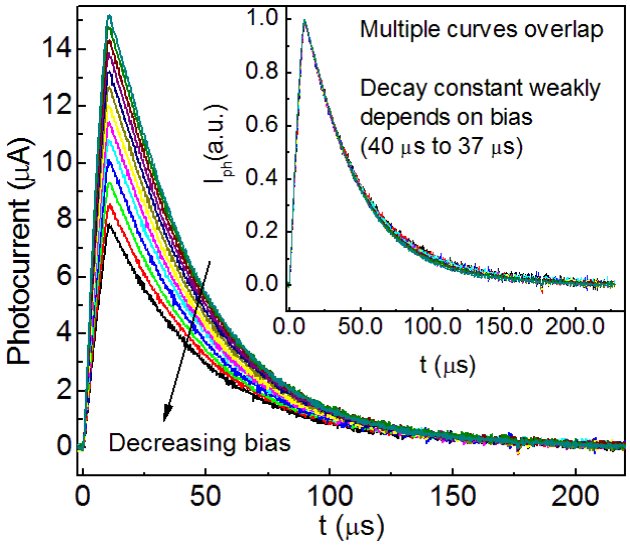

Figure 4.5: *Photocurrent transient response for a 10 μs light pulse under reverse bias varying from 0 V to 1.2 V. The magnitude of the photocurrent transient increases but the decay time constant remains almost same.*

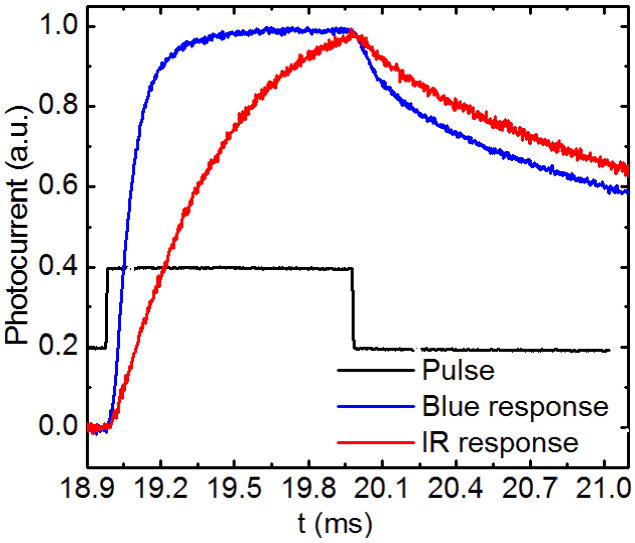

Figure 4.6: *Transient photocurrent response under blue (blue line) and IR (red line) light pulse (black line). 470 nm blue LED and 930 nm IR LED is used with a pulsed voltage source (10 % duty cycle at 100 Hz frequency).*

table. The slower and lower response to IR light can be attributed to the fact that the photogenerated carriers have contributions originating from the donor-acceptor

Table 4.2: *Rise and decay time for blue and IR light pulse*

Time constant	**Blue**	**IR**
Rise time τ_R	0.16 ms	$\sim$ 1 ms
Decay time τ_d	0.72 ms	1.45 ms

CTC. Also at low carrier concentration, the average mobility gets reduced by a power law behavior [93] of n where $\mu \propto n^{(T/T_0)-1}$, T_0 is related to the width of the Gaussian density of states. In this case the density of occupied states is very deep with high activation energy which in effect implies that the slow carriers take longer time to reach to the counter electrode and also explains the slower rise of $I_{ph}(t)$ observed in case of IR light pulse.

The device switching response is also sensitive to the background CW illumination. The CW white background typically results in device operation at higher charge carrier concentration. Under this condition, a drop in transient photocurrent magnitude is observed, at the same time response time decreases. The excess photogenerated carrier at steady state (space charge limited regime) reduces the exciton dissociation rate due to reduced built-in voltage and also increases the bimolecular recombination term. Hence in presence of a CW white background light source (same as that of a probe intensity), $I_{ph}(t)$ drops significantly. Under white background light, τ becomes lesser ($\sim$ 0.72 ms) than that of a device under dark background ($\sim$ 1.45 ms) as shown in the figure 4.7. The trap density of states under CW light follow a dynamic equilibrium condition, i.e. the trapping and detrapping rates are almost balanced. Hence $dm(\varepsilon)/dt$ of equation 4.8 upon photo illumination is less. McNeill *et. al.* have also shown that increasing CW background light can reduce the decay time constant [193]. This indicates that the slow release of trapped charge carriers after switching off the pulsed illumination is very small;

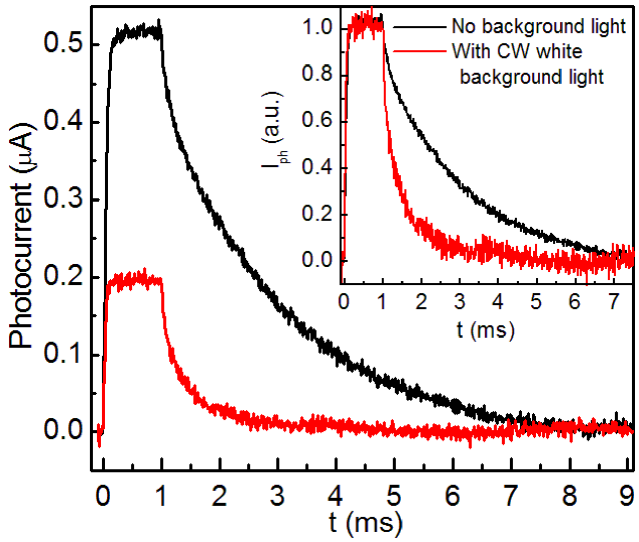

Figure 4.7: *Red LED (650 nm, ∼ 1 mW/cm^2) is used as a pulsed (1 ms) light source along with a white LED as background light source. Transient measurement was carried out with and without background light. Inset: normalized response for transient photocurrent under dark as well as CW white background illumination.*

they are completely filled due to CW background light.

These factors pertaining to background light are also important in determining the utility of the photodetector, especially in the NIR regime. The results from all the measurements have been consistent with electrical transport models based on trap dominated mechanisms.

4.4 Summary

Low band gap polymer PCPDTBT coupled with PCBM to form BHJ devices exhibit a wide spectral response. Appreciable photocurrent is observed at the absorption tail states which extend to communication wavelength regime. The trap assisted electrical transport results in a slow extraction of charge carrier which leads to a long-lived response in the $I_{ph}(t)$ measurements. The responsivity and

response time constants of these devices in the photodetector mode can be improved by operating the device in reverse bias (photoconducting mode). It may be possible to further optimize the device by an appropriate donor-acceptor composition and appropriate annealing conditions which can further modify the distribution of the defect density and the energetics.

SECTION 5

Electric field induced instability of conducting liquid and its application to Organic Optoelectronic devices

5.1 Introduction

Electrohydrodynamic instability of a conducting liquid surface in a strong electric field (EF) has been of considerable scientific interest with the earliest report dating back to 1917. Experiments on mercury surface under EF were studied by Tonk [209] to address issues related to surface distortion and the net pressure along with the liquid motion. Subsequently, EF-induced instability of conducting liquid has been studied in the context of vacuum discharge, charge emission and breakdown voltages. The conducting liquid system in EF can be accurately dealt with in terms of the interplay of three competing forces; electrostatic force, surface tension and hydrostatic pressure. The latter two terms act as the restoring force while the electrostatic pressure provides the destabilizing interaction. At low field strength, the surface tension and hydrostatic pressure dominate resulting in equilibrium shapes, and beyond a critical voltage the electrostatic pressure takes over resulting in continuous deformation. The induced charge accumulates on the surface shielding the bulk in conducting liquid films under a homogenous field, unlike the case of

dielectric-viscous films where the EF induced instability manifests in form of locally ordered pillars on the surface having hexagonal symmetry [210]. The dynamics and evolution of pattern formation essentially results from the competing effects of the destabilizing electrostatic pressure $P_0 \sim E_0^2/8\pi$ due to the imposed external field E_0 and the stabilizing Laplace-pressure at the dielectric-air interface. The induced charges developed by the interaction of the EF on the conducting liquid surface modify the growth of surface fluctuations. Stability analysis examined by the response to a surface perturbation of the metallic liquid surface points towards a linear and a non-linear stage in the deformation [211, 212].

Another related electromechanical phenomenon is electrowetting (EW) where the contact angle [213] is a function of the electrostatic conditions. For example, in case of the charged drop in contact with the bottom electrode, the EF at any point away from the contact line depends on the radius (R) of the droplet, distance (d) between two electrodes and the angle with respect to the z-axis. In this charged droplet case, EF and the charge density near the three-phase contact line diverges. The EW feature is given by Lippmann-Young's equation [214–216], where the contact angle of the drop decreases under the EF to minimize the surface energy [217, 218] leading to increased wetting of the liquid drop and can be observed to counter the drop extension (along z-axis) in the lower V regime, especially for the charged drop case. At high field regime, the contact angle tends to saturate and the vertical z-extension rapidly dominates over EW. The EW related dimensional changes in the present set of results is relatively insignificant compared to the drop-height variations and can be viewed as a minor correction factor.

These phenomena at small length scales can be viewed from the perspective of a method with a potential for reliable delivery and control of nanoliter-scale volumes of viscous fluids in a relatively facile manner. The deformation of conducting

liquid surfaces using low temperature metal-alloys offers a close look at the phenomena. This opens up options for controlled contact formation with fundamental implications in studying electrical transport in soft systems and can be applicable in printable electronics [219].

5.2 Theory: Field induced instability

The surface of thin liquid films is morphologically unstable under the competing action of surface tension and dispersive van der Walls force between films and substrates. Applying a strong EF some of the mode starts dominating over others and leads to instability. The effect of EF is modeled as shown in the figure 5.1. Height of the hump y is much smaller than the R. So from simple geometry

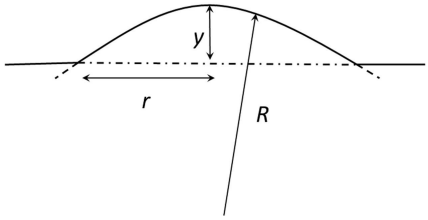

Figure 5.1: *Shape of hump assumed in the liquid surface with a radius of curvature R at the vertex of the hump, y is the height of the vertex and r is the effective radius of the hump taken as the radius of the small circle cut from the y=0 plane.*

$$yR = \frac{1}{2}(r^2 + y^2) \tag{5.1}$$

Assuming a constant EF E_0 and the enhanced field at the vertex of the hump E, the total pressure on the liquid surface is calculated. There are three components of downward pressure as well: (1) atmospheric pressure A, (2) pressure arising from the surface tension $2\gamma/R$ where γ is the surface tension and (3) electrostatic

pressure due to enhanced EF at the vertex $E^2/8\pi$. So, the net upward pressure is given by the equation 5.2

$$P = (E^2 - E_0^2)/8\pi - \rho g y - 2\gamma/R \tag{5.2}$$

If P is positive then surface tends to deform; if P is negative liquid surface tends to flatten out. The enhance field at the vertex depends on the geometry of the surface and approximately it takes the form as shown in the equation 5.3.

$$E = E_0(1 + 2y/r) \tag{5.3}$$

From the equations 5.1, 5.2 and 5.3 the net pressure is

$$P = yE_0^2/\pi\Big[\frac{y+r}{r^2} - \frac{4\pi\gamma/E_0^2}{y^2+r^2} - \frac{\rho\pi g}{E_0^2}\Big] \tag{5.4}$$

Total pressure could be positive or negative depending on the value inside the bracket. However y is much smaller than r and hence the equation 5.4 can be modified where $1/r$<or $>(4\pi\gamma/E_0^2)/r^2+\pi\rho g/E_0^2$, or in terms of EF as E_0^2 <or $>4\pi\gamma/r+\pi\rho g r$. The minimum value E_m of E_0 which will cause instability and the corresponding value r_m of r are seen to be $E_m = 2\pi^{1/2}(\rho g T^{1/4})$, $r_m = 2(\gamma/\rho g^{1/2})$. For a mercury surface the numerical values are 56,700 Vcm^{-1} for E_m and 0.367 cm for r_m. On a large free surface subject to a given E_0 which is greater than E_m only those distortions will grow whose radii lie within the limits indicated. In the low field regime ($<E_m$) no distortion of the surface arises, but above that field strength the distortion increases progressively under the net unbalanced pressure P. In particular it can easily be shown that for $r = r_m$ the bracket in equation 5.4 becomes [1-$(E_m/E_0)^4$]/$2A$ where $A = 8\pi T/E_0^2$. As the $(E_m/E_0)^4$ term represent

the gravitational force, when $E_0^4 \gg E_m^4$ gravitational term can be neglected. The field at which surface distortion starts growing and surface becomes instable can be written as $E_0{>}3E_m$. As the hump develops, the liquid starts flowing into from its immediate neighborhood. On an average, this flow extends over a distance comparable with r. If the area associated with the flow is a, the volume of the liquid flowing into is ar. It is possible to solve analytically to find out the velocity $\dot{y}$. The corresponding momentum is thus $\rho ar\dot{y}$. Its rate of increase is equal to the force acting on the surface i.e. $aP{=}\rho ad(r\dot{y})/dt$. Substituting this to equation 5.4, the equation of motion can be written as

$$\frac{d(r\dot{y})}{dt} = B^2 y\Big(\frac{r+y}{r^2} - \frac{A/2}{r^2+y^2} - \frac{\rho\pi g}{E_0^2}\Big) \tag{5.5}$$

where $B^2 = E_0^2/\pi\rho$. The solution of the equation 5.5 gives the evolution of the hump. However solution of the equation 5.5 is possible only when the relation between r and y is known.

5.2.1 Deformation of droplet vertex

The inherent high surface energy of metallic liquids such as Hg, Ga, In-Sn, and In-Bi-Pb-Sn alloys prevents the formation of a planar surface and tends to form spherical contour radius $R \gg \xi$ (where ξ is the surface perturbation), and $R = [3V_0/2\pi(1-\cos\theta_0)]^{1/3}$ where V_0 is the volume of the drop ($\sim$2 to 4 μl) and θ ($\sim$120° to 90°) is the contact angle [Fig. 5.2]. Studies were carried on charged-drop where it was directly in contact with the bottom electrode. Other experiment was on induced charge-drop where a dielectric layer was coated to insulate the drop from the bottom electrode. Upon applying an external bias, the EF at the drop vortex is enhanced due to induced surface charge density. For low E_0, liquid surface

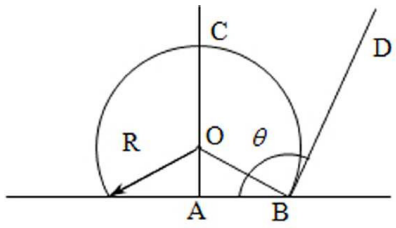

Figure 5.2: *Model of a spherical droplet (of radius R) of volume V_0 on a conducting electrode with contact angle θ_0.*

can be assumed to be stable and the resulting surface profiles can be determined analytically from the field distribution and the energy balance conditions. The hemispherical surface-induced charge density in a uniform axial field [220] is shown in equation 5.6.

$$\sigma = \Big(\frac{1}{4\pi}\Big)\frac{\partial\phi}{\partial r}\Big|_{r=R} = \Big[\frac{3E_0}{4\pi}\cos\theta\Big] \tag{5.6}$$

This gets modified under low bias to an experimentally verifiable prolate-spheroid ($c \geq$a = b) type charge distribution [Fig. 5.3] accompanied by the minor modifications in the scalar potential as shown in the equation 5.7. The charge density near the contact line tends to zero and EF is minimum.

$$\phi = -E_0 z\Big[1 - \frac{\tanh^{-1}\sqrt{(c^2-a^2)/(\xi^2+c^2)} - \sqrt{(c^2-a^2)/(\xi^2+c^2)}}{\tanh^{-1}\sqrt{(1-a^2/c^2)} - \sqrt{(1-a^2/c^2)}}\Big] \tag{5.7}$$

For a charged droplet, EF on the droplet surface is modified by the proximity of top electrode and EF can be estimated by image method. EF at any point on the drop surface (away from the contact line) is given by the equation 5.8

$$\begin{aligned}\vec{E} = \Big[\Big(\frac{Q}{4\pi\epsilon_0 R^2}\Big)^2 + \Big(\frac{Q}{4\pi\epsilon_0(4d^2+R^2-4dR\cos\theta)}\Big)^2 \\ + 2\Big(\frac{Q}{4\pi\epsilon_0}\Big)\frac{cos(\theta+\varphi)}{R^2(4d^2+R^2-4dR\cos\theta)}\Big]^{\frac{1}{2}}\end{aligned} \tag{5.8}$$

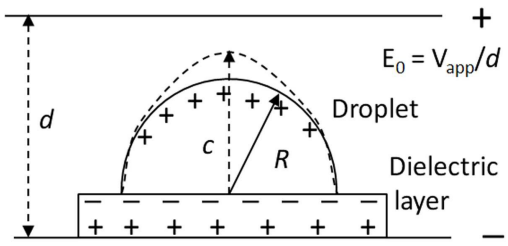

Figure 5.3: *Hemispherical droplet on a dielectric layer under electric filed E_0. Solid semicircle represents original shape of the droplet without any external field whereas dotted line represents prolate-spheroid shape under electric field.*

Where 'Q' is the total charge on the droplet surface, 'R' is the radius of the droplet 'd' is the distance between two electrode, $\varphi = \tan^{-1}[R\sin\theta/(2dR\cos\theta)]$. However due to electrostatic pressure, the droplet size changes to prolate shape as mentioned earlier. Approaching towards the contact line due to higher radius of curvature, charge density increases and hence EF increases (non-zero EF even at angle 90°) as shown in the figure 5.4.

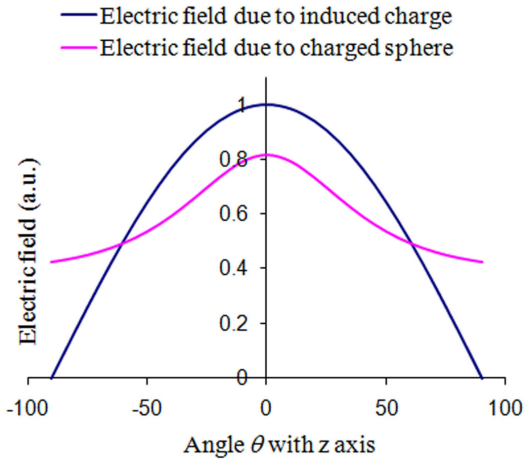

Figure 5.4: *Electric field profile on the droplet surface when droplet is on a conducting surface (charged droplet) and on a dielectric surface (induced charge).*

In this low-bias range, the surface energy contribution scales with the electrostatic energy maintaining the shape of the drop, with the dimensions gradually

varying with the strength of the field. As the bias is increased further, the electrostatic pressure increases, $P \geq P_0$, at $E \geq E_c$ (where E_c is the critical EF), the instability sets in leading to an irreversible surface deformation. In the instability regime, the recursive interdependency of the distorted surface and the non-uniform field distribution along with the associated dynamics leads to the complexity of the problem. However, the critical field, $E_c \sim (g\gamma\rho)^{1/2}$ [221] which is experimentally verifiable, can be predicted from a linear stability analysis.

5.2.2 Electrowetting

For a drop of volume V_0 and contact angle θ_0 radius of the drop can be estimated as in figure 5.2. Applying voltage V contact angle changes to θ_V and radius R changes accordingly as shown in equation 5.9.

$$\frac{dR}{d\theta} = -\frac{R\sin\theta}{3(1-\cos\theta)} \tag{5.9}$$

Change in height of the droplet is given by the equation 5.10.

$$\frac{dh}{d\theta} = \frac{\partial}{\partial\theta}\Big[R(1-\cos\theta)\Big] = \frac{2}{3}R\sin\theta \tag{5.10}$$

Solving this equation we get change in height (equation 5.11).

$$\Delta h = \Big(\frac{3V_0}{2\pi}\Big)^{\frac{1}{3}}\Big[(1-\cos\theta_0)^{\frac{2}{3}} - (1-\cos\theta_V)^{\frac{2}{3}}\Big] \tag{5.11}$$

EW on a conducting surface happens due to charge transfer from electrode to liquid (for a particular combination of electrode and electrolyte which gives rise to polarization at the interface) leading to charge and dipole redistribution at the

interface and hence decrease in interfacial surface tension. However the alloy in this case is a conducting liquid, hence the charge separation at the interface is negligible as the capacitance due to electric double layer (EDL) formation is quite low. Small changes in contact angle occur at very low voltage; whereas at higher voltage, contact angle gets saturated and EF induced deformation dominates over EW. Change in height due to change in contact angle is almost linear for small change [Fig. 5.5].

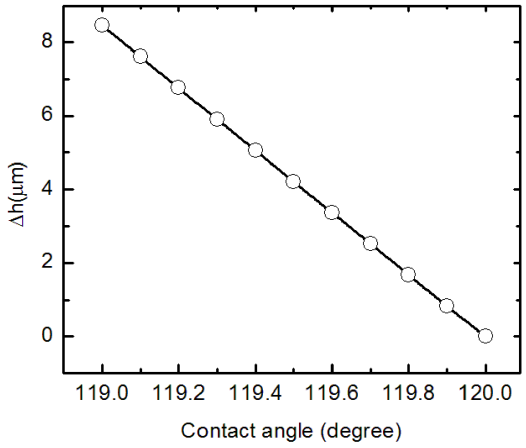

Figure 5.5: *Change in height due to change in contact angle ($\Delta\theta$ = 1°). Model droplet of volume 2 μl and initial contact angle θ_0 = 120°*

5.3 Materials and Methods

The quaternary alloy drops (eutectic mixture of Bi 49%, In 21%, Pb 18%, Sn 12% with a melting temperature 58 °C) of a desired dimension, 1 mm^2 - 10 mm^2 were deposited on the temperature controlled (65 °C) substrate using a dispenser consisting of heater-wire wrapped glass-capillary tubes. Similar experiment was also done on In-Ga alloy with a ratio of 0.24:0.76 which is a liquid at room temperature. In the experimental arrangement, the drop is isolated from the bottom electrode

using a polymer-dielectric layer of 1 - 2μm thickness as shown in the Figure5.6. 100 V to 1 KV was applied in steps of 5 V between two electrodes with Keithley High Voltage Supply (Model 248) keeping the inter-electrodes distance constant. The

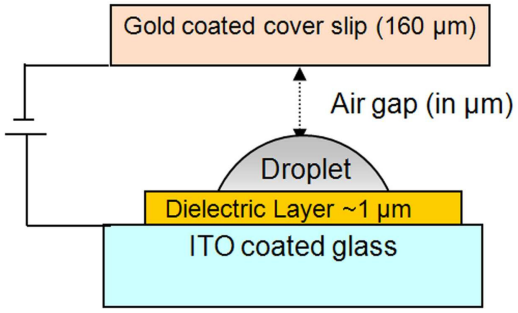

Figure 5.6: *Schematic of experimental set up for EF induced drop deformation. The top-contactor surface could directly be a conducting layer as indicated in the figure or a dielectric-coated conducting layer. At least one dielectric layer (top or bottom) is necessary to prevent current flow through the drop upon contact.*

constant voltage experiments where the EF was varied by controlling the distance between two electrodes in steps of 1 μm using a THORLABS Stepper Motor Controller was also carried out. Both the experiments were done for charged droplet as well where conducting droplet is in direct contact with one of the electrode. The EF variation with the decreasing inter-electrode spacing is shown in the figure 5.7.

5.4 Measurements & Results

The separation between two electrodes was maintained at a constant distance and the bias voltage was varied to induce instability. Extension rate of the drop was monitored using a CCD camera operating at 30 frames per sec mounted on a 50X objective lens. The images of the drop were analyzed using Motic-Image 2.0 software to obtain the drop dimensions and profiles. A priory estimate of E_c was used

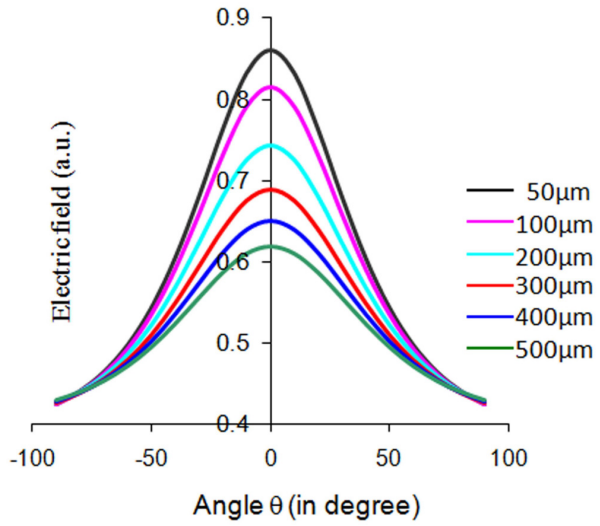

Figure 5.7: *Electric field strength variation with the inter-electrode spacing keeping the applied voltage constant. Flied strength increases sharply at the vertex with the decreasing inter-electrode spacing*

in positioning the top contactor electrode. For ex.: the experimental value for $E_c \sim$ 3.8 V/μm was observed to match the estimate, for a 3 mm diameter alloy drop and 150 μm air gap (contactor - alloy drop vortex distance). The drop extension as functions of voltage bias with a constant inter-electrode separation-distance (d) as well a function of d at constant voltage was measured and is shown in figure 5.8 & 5.9. The extension dependence can be considered as linear in the low bias range which gets progressively nonlinear as the bias is increased. The low voltage linear region provides an extension rate in the range of 50 nm/V - 100 nm/V [Fig. 5.8]. In the case there the voltage bias is held constant and the separation d is a variable, the extension profile obtained is shown in figure 5.9. Extension changes in the range of 50 nm/μm is observed at large d, and in for smaller air-gap separation the profile changes are more rapid and is in the range of 600 nm/μm to 700 nm/μm as indicated in Figure 5.9. These observations indicate the control and

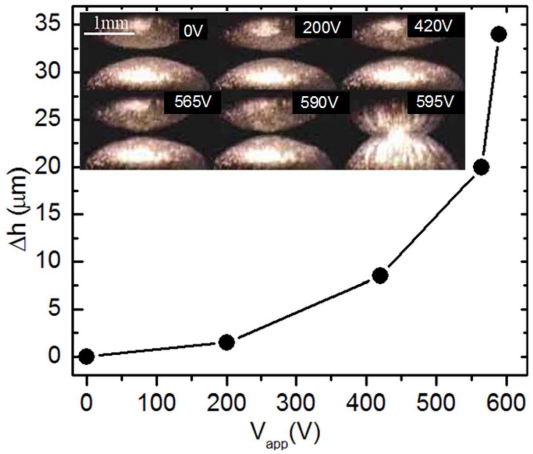

Figure 5.8: *Drop-height variation with respect to the voltage ($\leq V_c$). Inset: Optical image of alloy drop on dielectric layer coated ITO plate. Gold-coated cover slip forms top electrode (facing down) separated by initial air-gap of 50 μm. The images indicate the side-view of the drop along with its reflection off the Au coated top-contactor.*

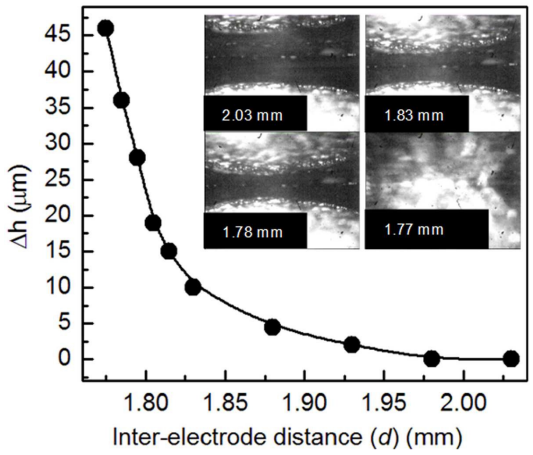

Figure 5.9: *Change in the drop-height as a function of inter-electrode separation distance (air gap d), V_{app} = 400 V. Inset: Optical image of the drop extension for different air gap at constant voltage.*

the sensitivity of the process for possible applications. The process of bridging the contactor is specific to the top contactor boundary condition. In cases where the top-contactor facing the drop is the bias-electrode and where the layer beneath the drop is the dielectric layer, the drop-electrode merger goes through an oscillatory

process below a critical separation distance with the contactor. This feature can be qualitatively understood in terms of discharge of the drop upon contact and the restoration of the drop shape, with the period of oscillation varying inversely as a function of separation distance. Inertial factors arising from adhesive interaction and surface modifications further alter this oscillatory process. It is noted that the drop upon contacting with the counter top-electrode can undergo further modification depending on the contactor surface conditions. A gradual irreversible increase of the contact area under EF [Fig. 5.10] is observed after making contact and can be understood in terms of the EW [222]. The alloy when gradually cooled after

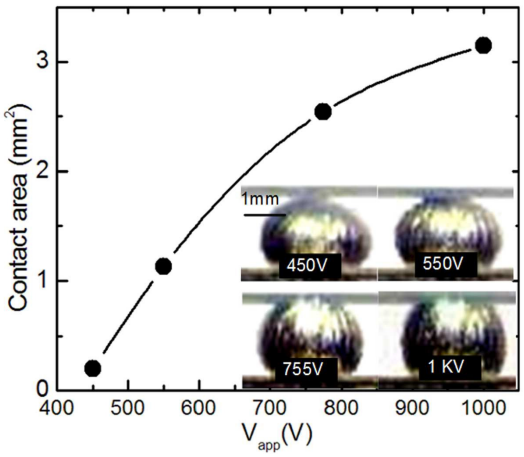

Figure 5.10: *Contact-area as a function of the applied voltage. Inset: Optical images of the drop profile upon contacting the top surface and the evolution of the contact area as a function of voltage.*

establishing contact under the bias (above a threshold-value) appeared to maintain its deformed shape. Cooling rapidly at EF = 0 or below a threshold value results in a finite gap between the contactor and the drop-vertex and this feature may be a useful procedure to generate nanogaps [223]. The retention of the drop-shape by this field sculpting procedure is also observed to depend on the flexural rigidity of the substrate and contactor, with thinner substrates (such as cover-glass) prov-

ing to be a better platform to implement this procedure. Optical micrographs do not reveal any particular stress/cracks related features on the cooled alloy surface introduced by the procedure.

Another interesting observation was made for an induced charge droplet experiment. The experiment was carried out with a gold coated top electrode facing towards the droplet. Upon increasing voltage droplet starts deforming to a certain extend and then start oscillating with a characteristic frequency. The oscillation frequency depends on the droplet size as well as the applied field strength. The electrostatic pressure depends on the induced charge on the alloy surface. However after making a contact with the top contactor charge gets reduced. If the adhesion between gold surface and alloy surface is not good enough, due to gravitational force droplet vertex relaxes back to its initial shape and starts acquiring induced charge again and the whole process keeps repeating. Time constant associated with the charging and discharging of the droplet is quite small as the self capacitance of the droplet ($\kappa\epsilon_0 R$) is very small ($\sim$ pF) and resistance is also small ($\sim \Omega$ mainly due to contact resistance). Oscillation frequency solely depends on the mechanical time constant of the system (droplet size, EF, viscosity, surface tension). According to Tonks-Frenkel instability, a height ξ of a surface perturbation grows exponentially (Equation 5.12).

$$\frac{d\xi}{dt} = \alpha\xi \tag{5.12}$$

Oscillation time period depends on two time scales, growth time of the surface perturbation and the relaxation of the droplet after discharge occurs, provided the contact area is very small prior to discharging of the droplet and the adhesion energy to the top surface is less. So total time period will be given by $\tau = \tau_1 + \tau_2$

where $\tau_i = 1/\alpha_i$. α_1 is the growth constant and α_2 is the decay (relaxation) constant where α_1 depends on EF but α_2 is independent of EF. α_1 increases with the EF and hence the frequency of oscillation (of the order of few Hz) increases with the applied field. However, beyond a certain field strength alloy droplet makes a permanent contact with the gold surface and oscillation stops.

5.5 Application in organic/molecular electronics

Methodology of depositing the electrodes has been utilized in our laboratory. The knowledge of the field dependent drop profile along with the positioning tools is used as a method to develop soft electrode contacts onto polymer/organic/molecular layers in devices with patterned substrates. We fabricated and characterized polymer based solar cells with alloy cathodes. Polymer light emitting diodes were also fabricated and their performance is comparable to conventional device fabrication process with low work-function cathode materials.

5.5.1 Polymer solar cells and Light emitting diodes

Polymer based light emitting diodes (PLEDs) [179, 224] and photovoltaic cells have drawn considerable attention. The metal cathodes in electroluminescent (EL) polymer for LEDs are normally thermally-evaporated low-work-function metals [180]. A recent report reveals that Ag-paste can be printed on top of active layers as a cathode and the resulting PLEDs have a comparable device performance to those with Ba, Ca, or PFNR2/Ag (prepared by thermal deposition) cathodes. The Ag-paste cathode [135] which consists of Ag in a binder is expected to suffer from numerous issues related to the inhomogeneity, chemical stability, mechanical integrity under prolonged operating conditions, rapid ageing etc. The present case

of EF assisted alloy printing method which enables fabrication of the devices on plastic (PET, PMMA) substrates also ensures the stability of the device and plays a role as an encapsulant layer by preventing moisture and oxygen diffusion. A set of two dozen solar cells and LEDs were fabricated using our laboratory protocol to evaluate the utility of the process. The results from the polymer solar cells using the alloy-electrodes is presented here. The cathode-deposition process was specifically used to address the dependency of fill factor (FF) to both the interfacial features and bulk-limiting factors in efficient P3HT-PCBM based solar cells. FF is a sensitive parameter, which depends on both the bulk material property and the quality of the cathode-polymer interface [89]. In conventional deposition technique, we observe that slow evaporation rate provides a conformal coating of the metal on the polymer with the interface quality suitable for good collection efficiency leading to a better FF. It was observed that the parameters in the procedure for melting the alloy, depositing it using EF and freezing it subsequently also leads to characteristic polymer-alloy interface morphology. In general, in the melt phase the electrode forms an intimate contact, which can be preserved upon decreasing the temperature gradually, leading to optimized polymer/cathode interface. Low melting point (58°C eutectic) alloy was employed as the cathode material for a highly efficient polymer/fullerene solar cell and the performance was comparable to a conventional cell with Ca-cathode.

5.5.1.1 Polymer solar cells fabrication & measurements

ITO coated glass substrates are cleaned and etched to fabricate organic photovoltaic devices. PEDOT:PSS ($\sim$ 80 nm thickness) was spin coated from the aqueous solution on the ITO coated glass substrate and annealed at 120 °C for 30 minute. Optically active polymer Poly (3-hexylthiophene) (P3HT) and poly[6,6-phenyl-C_{61}-

butyric acid methyl ester] (PCBM) (1:1 ratio by weight) dissolved in Tetrahydrofuran (THF) (20 mg/ml concentration) was spin coated (∼100 nm thickness) in N_2 environment in the glove box on pre-deposited PEDOT/PSS film and annealed at 80°C for 20 minute. The liquid alloy cathode material was then deposited on the polymer blend film using the EF induced deformation of the liquid droplet at 65°C. The alloy drop - device was insulated by dielectric layers ensuring the absence of any current-flow through the device during the contact process. After the contact formation, droplet was cooled gradually (keeping EF ON) to avoid crack or fracture. The performance parameters of J_{SC} ∼2 mA/cm^2, V_{OC} ∼0.45 V and FF ∼48 % fill factor (with 50 mW/cm^2 Xenon lamp illumination) were achievable [Fig. 5.11]. The alloy droplet also acts as an encapsulation for these devices; hence these devices were more stable compared to devices where Al or Ca/Al cathode was thermally deposited. The EF dependence of the alloy-polymer contact area

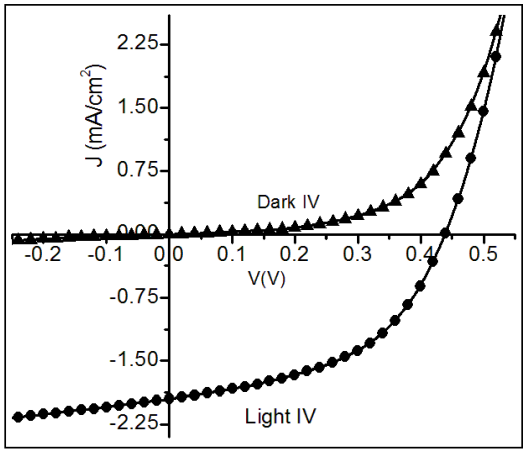

Figure 5.11: *I-V of P3HT:PCBM blend based polymer solar cell using the metal alloy drop as the cathode (contact area 0.2 mm^2), using Xe white light source (∼ 50 mW/cm^2)*

can be utilized to arrive at an appropriate dimension (∼ 0.2 mm^2 in the present case).

One of the efficiency limiting parameter in BHJ solar cells is the fill factor. A dominant factor which results in the reduced fill factor is due to imbalance in the charge transport (electrons and holes) in the BHJ layer. The mismatch of drift length ratio of electrons and holes in the MEH-PPV:PCBM blend gives rise to reduced fill factor. Another factor observed in our laboratory earlier arises from the polymer/electrode interface properties [89]. The polymer/cathode interface lowers the FF even though the drift length for electrons and holes are comparable as in P3HT:PCBM blend devices. The conventional physical vapor deposition of aluminum (Al) electrode at a slow deposition rate results in conformal coating whereas fast Al deposition leads to void space between polymer and electrode. Higher fill factor was observed for conformal Al coating. The presence of low melting point alloy and the EF induced contact formation provides us the opportunity to vary the quality of the electrode layer in a facile manner. A sub-optimized condition of cooling of the alloy melt-phase prior to establishing the contact with the polymer surface results in reduced fill factor [Fig. 5.12(a)]. Optical images from a device having fill factor 25% and 38% is shown in the figure 5.13. It was observed that alloy in melt phase forms better interface with the polymer compared to solid phase [Fig. 5.12(b)]. The in-situ measurement of the BHJ-PSCs with deformable cathodes confirmed the importance of the electrode/polymer interface in deciding the FF magnitude.

5.5.1.2 Polymer Light Emitting Diodes

The structure of PLEDs comprises of multi-layer deposition in the form of electrode/ Emissive layer (EML)/ Cathode. ITO coated glass substrates were used as bottom electrodes. ITO substrates were cleaned with IPA/Acetone solution, ethanolamine/H_2O (1:10) solution followed by RCA cleaning process (H_2O, Am-

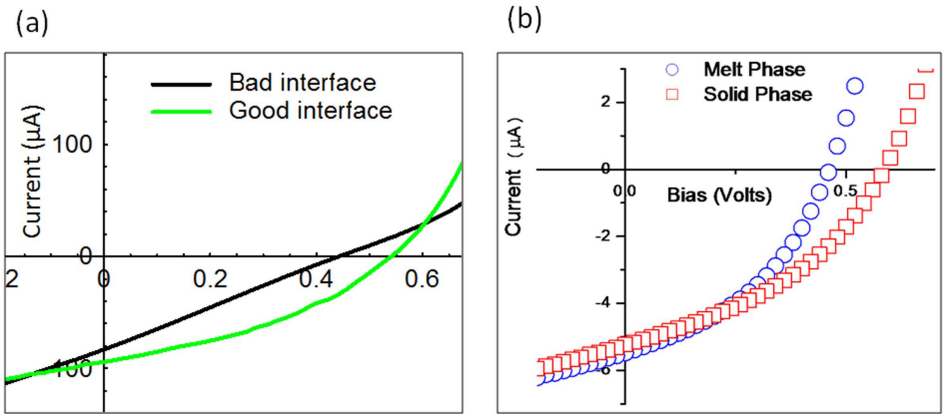

Figure 5.12: *(a) I-V of P3HT:PCBM blend based polymer solar cell using the metal alloy drop as the cathode material. Rapid cooling of alloy cathodes results in bad interface. (b) I-V measurement of P3HT:PCBM device with alloy as cathode material in solid phase and melt phase. Figure is adopted from the reference [89].*

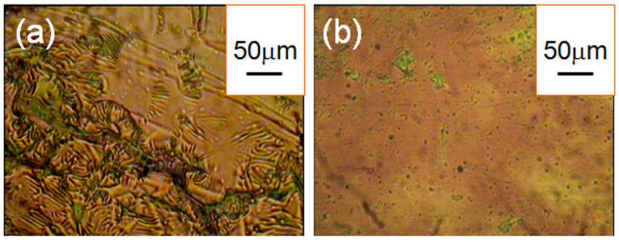

Figure 5.13: *Optical images (500X magnification) of ITO/P3HT:PCBM/alloy device with (a) rapid cooling of alloy, fill factor 25%. (b) slow cooling of alloy, Fill factor 38%.*

monium solution and H_2O_2 in 5:1:1 ratio). A thin layer of PEDOT:PSS was spin coated on top of it and was kept for curing for 1 hour at 120 °C. MEH-PPV was synthesized from precursor and PAG. 16 mg of precursor was dissolved into 1.6 ml chloroform. 2 mg of PAG was dissolved into chloroform and added to precursor solution. Devices were then fabricated by spin coating in dry nitrogen environment and exposed to UV light for 15 minute and kept for curing for 1 hour at 80°C. Al and Ca/Al were deposited on the top layer of polymer film by physical vapor deposition at high vacuum (1.8×10^{-5} mbar) whereas fusible alloy was deposited by

drop cast on the MEH-PPV film. Drop size varies from 0.5 mm to 3 mm diameter and of 200 to 500 μm thick.

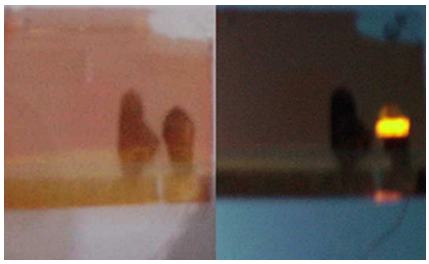

Figure 5.14: *MEH-PPV based light emitting diode.*

It has been observed that polymer alloy interface is more ohmic in nature, where as polymer Al interface is more Schottky type. From semi-log graph knee voltage for Al is 1.4 V shown in the figure 5.15(a), but for alloy cathode, current starts flowing through the device even if at much lower voltages. Typical device performance shows that at 0.1 V, current flowing through the device with alloy cathode is 1 μA. For Al electrode at 1.4 V current flows through the device is 0.74 μA. LED with alloy electrode starts glowing when 1 mA current passes through the device and voltage is around 4.5 V. I-V curves for Al and alloy has been studied. For Al cathode, current increases more exponentially, where as for alloy cathode increase in current is more space charge limited. That means electron injection from alloy cathode is proportional to the square of voltage and does not suffer from any barrier height. I-V and Log (I) vs. V also have been checked for Ca/Al and alloy cathode. Alloy cathode performance is quite similar to that of Ca/Al in semi-log plot, but from I-V data, it is seen that for Ca/Al electrode current increased more exponentially than alloy cathode although knee voltage is quite similar to that of alloy material. However calcium electrode is not air stable. Electroluminescence is shown in [Fig. 5.15(b)]. MEH-PPV shows characteristic electroluminescence peak at 590 nm and 620 nm.

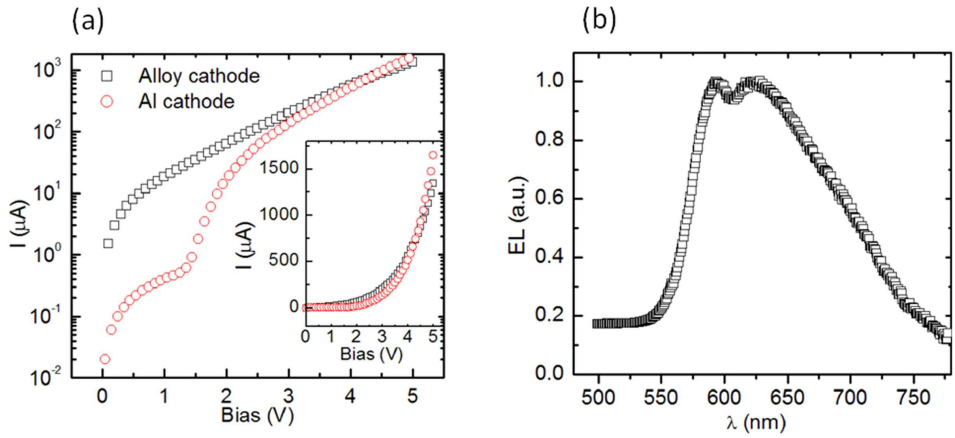

Figure 5.15: *(a) I-V curve of MEH-PPV polymer based LED with alloy and Al as cathode materials is shown in semi log plot. Inset: the I-V curve of the same sample. (b) EL spectrum of a MEH-PPV based light emitting diode at 4.5 V bias and 1 mA current.*

Devices fabricated using alloy as cathode materials are air stable. High yield and high reproducibility make this technique versatile for low temperature electrode deposition. Control over active area is useful to study the effect of active area on device performance. Repetitive melting and solidification of alloy contact does not change the polymer/alloy interface chemically or morphologically. Hence a stable response is observed even after several cycles of heating and cooling of the alloy materials.

5.6 Summary

Deformation of conducting droplet has been studied from two different perspectives. The growth of a droplet under EF follows an exponential behavior in low field regime, whereas growth is very fast at high field regime. The growth of the conducting droplet under EF can be controlled either by voltage sweep or by varying inter-electrode separation. The physical process of controlled deformation in

a metal alloy, which can be preserved by cooling, is utilized in polymeric/organic electronics in precise way. Specific advantages of this procedure are the possibility of directly coating the metal electrode without elaborate lithography procedures and also avoiding the requirements for physical masks and vacuum conditions. This can open up a new, complete vacuum free technique for soft contact formation on polymeric/organic film without damaging much. The performances of these devices are comparable to those of conventional electrode deposited devices. The alloy used here is very much air stable and works as an encapsulation for the devices.*

*Based on these studies, paper has been published in *Proc. R. Soc. A*, **465**, 1799, (2009).

SECTION 6

Summary and future direction

The development of polymer solar cell is growing very fast although the efficiency is yet to reach a milestone of 10% to realize devices which are commercially feasible. One of the efficiency limiting factors is the electrical transport through the disorder bicontinuous network of a BHJ solar cell. In this report we have studied some of the possible mechanism of transport dynamics and its effect on device performances. Different types of experiments such as; intensity modulated photocurrent measurement, photocurrent fluctuation analysis and the transient photocurrent measurement have been carried out to probe the carrier dynamics under certain conditions. We also highlight the possibilities of polymer based detector especially at NIR regime which can be used in optical telecommunication system.

Intensity modulated photocurrent measurements were carried out on bulk heterojunction polymer solar cells to extract the device parameters. A unique set of features from the results in the BHJ devices is exhibited in form a universal behavior in terms of the modulation frequency dependence of the photocurrent, which is not present in other families of solar cells such as; dye sensitized solar cells, bilayer solar cells or any inorganic solar cells. We have correlated the device efficiency to the photocurrent feature observed in the IMPS. Morphology effect on the device performance is also reflected in the modulated photocurrent spectrum especially at low frequency regime. Morphology can be controlled by processing of the device such as; changing the annealing condition, changing the D-A ratio

or using more rigid polymer to have higher crystallinity. Temperature dependent study is also carried out to understand the effect of trap filling and detrapping of charge carriers. The charge extraction resistance [$R_s \propto epx(\Delta/k_BT)$] at the polymer electrode interface is dependent on temperature and there exist a barrier (Δ) of 20-30 meV. Bimolecular recombination is strongly coupled with the carrier concentration. In low efficient devices, where exciton dissociation is reduced by the trapped carriers, show very low photocurrent magnitude especially at low frequency range. This result is consistent with the modulated photocurrent with higher intensity of light. AC impedance measurements were carried out on same sample with CW background light as well as in dark. The frequency dependence capacitance is observed to be higher with CW background light. More interestingly the frequency dependent loss factor also shows an anomalous behavior under white light illumination with minima at 5 kHz range.

Transport through disordered network can also be studied from the photocurrent fluctuation analysis. We have observed characteristic fluctuations of the short circuit current in BHJ solar cells. The PSD spectrum of such device exhibits a 1/f type behavior and is accompanied by a characteristic peak frequency in the 10 to 100 kHz range. The trap state dominated transport through the bulk is expected to be the origin of such fluctuations. We verified the fact with the kinetic Monte Carlo simulation that the fluctuation in the photocurrent is related to the transport of charge carrier through hopping with a characteristic waiting time in each site depending on the positional disorder and energetic disorder. At low temperature as well as at low intensity of light, photocurrent fluctuation gets reduced. We also see the co-existence of flicker noise in the low frequency regime (< 1 kHz) with an exponent of ~ 1.5. We probe the degradation of the sample devices under atmospheric condition. The characteristic peak frequency in the PSD spectrum shifts

towards the lower frequency regime. Noise power spectrum could be a valuable tool to understand and provides a deeper insight into the microscopic events occurring in the device. Detailed analysis of noise power spectrum under different experimental conditions should be able to provide and improve our understanding of the degradation mechanisms of the device.

Low bandgap polymers are widely used in polymer solar cells. These polymers could be good materials for photodetectors. Defects states in these polymer devices play a critical role in determining switching characteristics at NIR spectral region relevant to communication wavelength. We carried out detailed studies of the bandwidth limiting factors of the long-lived transient photocurrent as a function of temperature and wavelengths. Responsivity and spectral sensitivity have been tested under atmospheric condition and a significant response ($\sim$ 80 mA/W) is observed at 800 nm wavelength. Transient measurements were carried out at different temperature range. The dominant transport mechanism of the photogenerated carriers takes variable range hopping form at low temperature and nearest neighbor hopping at high temperature. A general trend of a slower response to wavelength corresponding to the band-tail region compared to the high-absorption region is observed. The dynamics of trapping and detrapping of charge carriers in a BHJ device is essentially a function of reverse bias voltage, light intensity and CW background light.

The final section of the thesis deals with the fabrication process of BHJ devices with low temperature processed cathodes. We have used a novel technique to deposit cathode materials on soft polymer films. This technique is based on the fact that under electric field any soft conducting material (low melting point alloy, M.P. 58 °C) gets deformed in a precise way. Three competitive force; hydrostatic pressure, surface tension and electrostatic pressure determine the dynamics

of deformation of a conducting droplet under electric field. At low field regime, the growth is linear with the bias voltage before it gets destabilized under high field. The linear regime of the droplet deformation under electric field is made use of soft contact deposition on polymer film. We have used this vacuum free deposition technique to fabricate polymer based solar cells as well as polymer based LEDs. The efficiency of these devices are comparable to that of the conventionally fabricated devices. These devices also exhibit reasonable air stability.

APPENDIX I

Matlab code for IMPS

```
R1=200000
R2=5000
C1=0.000000038
F=R1/(R1+R2)
a=0.0016
b=F*R2*C1+a
K1=0.000000028
K2=0.00009
m=b*K1
n=K2*b+K1
o=K2+b
sys=tf(-F*[a,1],[m,n,o,1]);
bode(sys);
[mag,ph,fre]= bode(sys);
dlmwrite('myfile.txt',mag, 'delimiter', '\t', 'precision', 6,'newline','pc');
hold on
```

APPENDIX II

Matlab code for FFT

Spectral power density from autocorrelation function

The power spectral density (PSD) describes how the power or variance of a time series is distributed with frequency. Mathematically, it is defines as the Fourier transform of the autocorrelation function. The autocorrelation function can be used for the following purposes (i) to detect non-randomness in data (ii) to identify an appropriate time series model if the data is not random. Given measurements x_1, x_2, ..., x_N at time t_1, t_2, ..., t_N, the lag k autocorrelation function is defined as

$$r_k = \frac{\Sigma_i (x_i - x_{mean})(x_{i+k} - x_{mean})}{\Sigma_i (x_i - x_{mean})^2} \tag{II.1}$$

Here $i = 1, 2, ...$ N. The PSD is given as:

$$S(f) = \int_{-\infty}^{\infty} r_k e^{-2\pi i f k} dk \tag{II.2}$$

Matlab code for FFT and frequency maxima histogram plot

% *Reading of data files*

N=input('how many files ');

% *Sampling rate*

Fs =250000;

m=0;

```
% Calculate frequency steps
f=(0:1024)*Fs/2048;
p=input('enter name of file ','s');
k=1;
for i=1:N
fid = fopen(p, 'r');
c = dlmread(p,',',5);
d=c(:,2);
wordcount=size(p,2);
wordcount=wordcount-4;
% Each data files splited into 11 data set
for j=1:11
e=d(1+m:2048+m);
% FFT of time series data
pxx=fft(e,2048)/2048/250000;
pxxz=1e18*(abs(pxx(10:1024)).^ 2);
% Find out frequency max
freqm=find(pxxz>=max(pxxz));
freqmax(k)=freqm(1,1)
k=k+1;
m=m+2048;
end
m=0;
if i<10
p(wordcount-1)=num2str(0);
p(wordcount)=num2str(i);
```

```
else
p(wordcount-1:wordcount)=num2str(i);
end
end
% Histogram plot
counts = hist(freqmax*30.517578*4,f);
save('histo.txt','counts','-ASCII');
h=dlmread('histo.txt');
k=1;
for i=1.0:50.0:1000.0
count=0;
for j=1:50
count = count + h(j+i-1);
end
y(k)=count;
k=k+1;
end
y=y';
plot(y);
save('data.txt','y','-ASCII');
fclose('all');
```

References

[1] de Winter, F. and Swenson, R. B. A WAKE-UP CALL, *Solar Today* **March/April** (2006).

[2] Green, M. A., Emery, K., King, D. L., Hishikawa, Y. and Warta, W. Solar cell efficiency tables (version 28), *Progress in Photovoltaics: Research and Applications* **14**, 455 (2006).

[3] *Solar Market Research and Analysis.* 2011, Solarbuzz. URL: http://www.solarbuzz.com/facts-and-figures/retail-price-environment/module-prices.

[4] Kallmann, H. and Pope, M. Photovoltaic Effect in Organic Crystals, *The J. of Chem. Phys.* **30**, 585 (1959).

[5] Alvarado, S. F., Seidler, P. F., Lidzey, D. G. and Bradley, D. D. C. Direct Determination of the Exciton Binding Energy of Conjugated Polymers Using a Scanning Tunneling Microscope, *Phys. Rev. Lett.* **81**, 1082 (1998).

[6] Scheidler, M., Lemmer, U., Kersting, R., Karg, S., Riess, W., Cleve, B., Mahrt, R. F., Kurz, H., Bässler, H., Göbel, E. O. and Thomas, P. Monte Carlo study of picosecond exciton relaxation and dissociation in poly(phenylenevinylene), *Phys. Rev. B* **54**, 5536 (1996).

[7] Campbell, I. H., Hagler, T. W., Smith, D. L. and Ferraris, J. P. Direct Measurement of Conjugated Polymer Electronic Excitation Energies Using Metal/Polymer/Metal Structures, *Phys. Rev. Lett.* **76**, 1900 (1996).

[8] Tang, C. W. Two-layer organic photovoltaic cell, *Appl. Phys. Lett.* **48** (1986).

[9] Yu, G., Gao, J., Hummelen, J. C., Wudl, F. and Heeger, A. J. Polymer Photovoltaic Cells: Enhanced Efficiencies via a Network of Internal Donor-Acceptor Heterojunctions, *Science* **270**, 1789 (1995).

[10] Padinger, F., Rittberger, R. S. and S., S. N. Effects of Postproduction Treatment on Plastic Solar Cells, *Adv. Funct. Mater.* **13**, 85 (2003).

[11] Reyes-Reyes, M., Kim, K. and Carroll, D. L. High-efficiency photovoltaic devices based on annealed poly(3-hexylthiophene) and 1-(3-methoxycarbonyl)-propyl-1- phenyl-(6,6)C_{61} blends, *Appl. Phys. Lett.* **87**, 083506 (2005).

[12] Li, G., Shrotriya, V., Huang, J., Yao, Y., Moriatry, T. and Emery, K.and Yang, Y. High-efficiency solution processable polymer photovoltaic cells by self-organization of polymer blends, *Nature Mater.* **4**, 864 (2005).

[13] Yu, G., Pakbaz, K. and Heeger, A. J. Semiconducting polymer diodes: Large size, low cost photodetectors with excellent visible-ultraviolet sensitivity, *Appl. Phys. Lett.* **64** (1994).

[14] Yu, G., Wang, J., McElvain, J. and Heeger, A. J. Large-area, full-color image sensors made with semiconducting polymers, *Adv. Mater.* **10** (1998).

[15] Drury, C. J., Mutsaers, C. M. J., Hart, C. M., Matters, M. and De Leeuw, D. M. Low-cost all-polymer integrated circuits, *Appl. Phys. Lett.* **73**, 108 (1998).

[16] Aoki, Y., Fujita, S., Haramizu, S., Akagi, K. and Shirakawa, H. Current progress in synthesis of polyacetylene films, *Synthetic Metals* **84**, 307 (1997).

[17] Ambegaokar, V., Halperin, B. I. and Langer, J. S. Hopping Conductivity in Disordered Systems, *Phys. Rev. B* **4**, 2612 (1971).

[18] Mott, N. F. and Davis, E. A. *Electronic processes in Non-crystalline Materials*. (Oxford:Clarendon Press) 2nd Ed., (1979).

[19] Miller, A. and Abrahams, E. Impurity conduction at low concentrations, *Phys. Rev.* **120**, 745 (1960).

[20] Belova, I. M. On the Theory of Tunnelling in Disordered Semiconductors, *physica status solidi (b)* **73**, 409 (1976).

[21] Merazga, A. and Herbane, M. Time photocurrent response and the density of localised states in disordered semiconductors, *Solid State Communications* **145**, 316 (2008).

[22] Hartenstein, B. and Bässler, H. Transport energy for hopping in a Gaussian density of states distribution, *J. of Non-Crystalline Solids* **190**, 112 (1995).

[23] Arkhipov, V. I., Heremans, P., Emelianova, E. V. and Adriaenssens, G. J. Space-charge-limited currents in materials with Gaussian energy distributions of localized states, *Appl. Phys. Lett.* **79**, 4154 (2001).

[24] Paasch, G. and Scheinert, S. Charge carrier density of organics with Gaussian density of states: Analytical approximation for the Gauss–Fermi integral, *J. of Appl. Phys.* **107**, 104501 (2010).

[25] Tiwari, S. and Greenham, N. Charge mobility measurement techniques in organic semiconductors, *Optical and Quantum Electronics* **41**, 69 (2009).

[26] Scher, H. and Montroll, E. W. Anomalous transit-time dispersion in amorphous solids, *Phys. Rev. B* **12**, 2455 (1975).

[27] Scharfe, M. E. Transient photoconductivity in vitreous As_2Se_3, *Phys. Rev. B* **2**, 5025 (1970).

[28] Bos, F. C. and Burland, D. M. Hole transport in polyvinylcarbazole: The vital importance of excitation-light intensity, *Phys. Rev. Lett.* **58**, 152 (1987).

[29] Pfister, G. and Griffiths, C. H. Temperature dependence of transient hole hopping transport in disordered organic solids: Carbazole polymers, *Phys. Rev. Lett.* **40**, 659 (1978).

[30] Borsenberger, P. M., Pautmeier, L. T. and Bässler, H. Nondispersive-to-dispersive charge-transport transition in disordered molecular solids, *Phys. Rev. B* **46**, 12145 (1992).

[31] Borsenberger, P. M. and Bässler, H. Tail broadening of photocurrent transients in molecularly doped polymers, *Journal of Applied Physics* **75**, 967 (1994).

[32] Hertel, D. and Bassler, H. Photoconduction in amorphous organic solids, *Chem. Phys. Chem.* **9**, 666 (2008).

[33] Monroe, D. Hopping in Exponential Band Tails, *Phys. Rev. Lett.* **54**, 146 (1985).

[34] Pai, D. M. Transient Photoconductivity in Poly(N-vinylcarbazole), *J. of Chem. Phys.* **52**, 2285 (1970).

[35] Hall, R. B. The Poole - Frenkel Effect, *Thin Solid Film* **8**, 263 (1971).

[36] Pasveer, W. F., Cottaar, J., Tanase, C., Coehoorn, R., Bobbert, P. A., Blom, P. W. M., De Leeuw, M. and Michels, M. A. J. Unified description of charge-carrier mobilities in disordered semiconducting polymers, *Phys. Rev. Lett.* **94**, 1 (2005).

[37] Tanase, C., Blom, P. W. M. and De Leeuw, D. M. Origin of the enhanced space-charge-limited current in poly(p-phenylene vinylene), *Phys. Rev. B - Condensed Matter and Materials Physics* **70**, 1 (2004).

[38] Liang, Y., Xu, Z., Xia, J., Tsai, S.-T., Wu, Y., Li, G., Ray, C. and Yu, L. For the Bright Future - Bulk Heterojunction Polymer Solar Cells with Power Conversion Efficiency of 7.4%, *Adv. Mater.* **22**, E135 (2010).

[39] *Solarmer Energy hits 7.9% efficiency with plastic organic photovoltaic solar cell breaks record.* Alternative Energy Info. December 6, 2009. URL: http://www.alt-energy.info/solar-power/solarmer-energy-hits-7-9-efficiency-with-plastic-organic-photovoltaic-solar-cell-breaks-record/.

[40] *Mitsubishi OPV achieves 8.5 % efficiency.* 18 Apr 2011, Plastic electronics. http://www.plusplasticelectronics.com/energy/mitsubishi-opv-achieves-8-5-per-cent-efficiency-29626.aspx.

[41] Servaites, J. D., Ratner, M. A. and Marks, T. J. Practical efficiency limits in organic photovoltaic cells: Functional dependence of fill factor and external quantum efficiency, *Appl. Phys. Lett.* **95**, 163302 (2009).

[42] Kumar, A., Li, G., Hong, Z. and Yang, Y. High efficiency polymer solar cells with vertically modulated nanoscale morphology, *Nanotechnology* **20**.

[43] Coffey, D. C. and Ginger, D. S. Time-resolved electrostatic force microscopy of polymer solar cells, *Nature Mater.* **5**, 735 (2006).

[44] Knupfer, M. Exciton binding energies in organic semiconductors, *Appl. Phys. A: Mater. Science & Processing* **77**, 623 (2003).

[45] Koster, L. J. A., Mihailetchi, V. D. and Blom, P. W. M. Ultimate efficiency of polymer/fullerene bulk heterojunction solar cells, *Appl. Phys. Lett.* **88**, 093511 (2006).

[46] Beljonne, D., Shuai, Z., Pourtois, G. and Bredas, J. L. Spin-Orbit Coupling and Intersystem Crossing in Conjugated Polymers: A Configuration Interaction Description, *The J. of Phys. Chem. A* **105**, 3899 (2001).

[47] Rothe, C., Guentner, R., Scherf, U. and Monkman, A. P. Trap influenced properties of the delayed luminescence in thin solid films of the conjugated polymer Poly (9,9-di(ethylhexyl)fluorene), *The J. of Chem. Phys.* **115**, 9557 (2001).

[48] Reufer, M., Lagoudakis, P. G., Walter, M. J., Lupton, J. M., Feldmann, J. and Scherf, U. Evidence for temperature-independent triplet diffusion in a ladder-type conjugated polymer, *Phys. Rev. B* **74**, 241201 (2006).

[49] Brabec, C., Winder, C., Sariciftci, N., Hummelen, J., Dhanabalan, A., van Hal, P. and Janssen, R. A Low-Bandgap Semiconducting Polymer for Photovoltaic Devices and Infrared Emitting Diodes, *Adv. Funct. Mater.* **12**, 709 (2002).

[50] Brabec, C. J., Sariciftci, N. S. and Hummelen, J. C. Plastic Solar Cells, *Adv. Funct. Mater.* **11**, 15 (2001).

[51] Koster, L. J. A., Smits, E. C. P., Mihailetchi, V. D. and Blom, P. W. M. Device model for the operation of polymer/fullerene bulk heterojunction solar cells, *Phys. Rev. B* **72**, 085205 (2005).

[52] Hwang, I.-W., Soci, C., Moses, D., Zhu, Z., Waller, D., Gaudiana, R., Brabec, C. J. and Heeger, A. J. Ultrafast Electron Transfer and Decay Dynamics in a Small Band Gap Bulk Heterojunction Material, *Adv. Mater.* **19**, 2307 (2007).

[53] Onsager, L. Initial Recombination of Ions, *Phys. Rev.* **54**, 554 (1938).

[54] Braun, C. L. Electric field assisted dissociation of charge transfer states as a mechanism of photocarrier production, *The J. of Chem. Phys.* **80**, 4157 (1984).

[55] Koster, L. J. A., Mihailetchi, V. D. and Blom, P. W. M. Bimolecular recombination in polymer/fullerene bulk heterojunction solar cells, *Appl. Phys. Lett.* **88**, 052104 (2006).

[56] Mihailetchi, V. D., Koster, L. J. A., Hummelen, J. C. and Blom, P. W. M. Photocurrent Generation in Polymer-Fullerene Bulk Heterojunctions, *Phys. Rev. Lett.* **93**, 216601 (2004).

[57] Barker, J. A., Ramsdale, C. M. and Greenham, N. C. Modeling the current-voltage characteristics of bilayer polymer photovoltaic devices, *Phys. Rev. B* **67**, 075205 (2003).

[58] Mihailetchi, V. D., Wildeman, J. and Blom, P. W. M. Space-Charge Limited Photocurrent, *Phys. Rev. Lett.* **94**, 126602 (2005).

[59] Tessler, N. and Rappaport, N. Excitation density dependence of photocurrent efficiency in low mobility semiconductors, *J. of Appl. Phys.* **96**, 1083 (2004).

[60] Sze, S. M. *Physics of Semiconductor Devices*. Wiley, New York, (1981).

[61] Potscavage, W. J. J., Yoo, S. and Kippelen, B. Origin of the open-circuit voltage in multilayer heterojunction organic solar cells, *Appl. Phys. Lett.* **93**, 193308 (2008).

[62] Cheyns, D., Poortmans, J., Heremans, P., Deibel, C., Verlaak, S., Rand, B. P. and Genoe, J. Analytical model for the open-circuit voltage and its associated resistance in organic planar heterojunction solar cells, *Phys. Rev. B* **77**, 165332 (2008).

[63] Koster, L. J. A., Mihailetchi, V. D., Ramaker, R. and Blom, P. W. M. Light intensity dependence of open-circuit voltage of polymer:fullerene solar cells, *Appl. Phys. Lett.* **86**, 123509 (2005).

[64] Vandewal, K., Gadisa, A., Oosterbaan, W. D., Bertho, S., Banishoeib, F., Van Severen, I., Lutsen, L., Cleij, T. J., Vanderzande, D. and Manca, J. V. The Relation Between Open-Circuit Voltage and the Onset of Photocurrent Generation by Charge-Transfer Absorption in Polymer:Fullerene Bulk Heterojunction Solar Cells, *Adv. Funct. Mater.* **18**, 2064 (2008).

[65] Wang, D. H., Lee, H. K., Choi, D.-G., Park, J. H. and Park, O. O. Solution-processable polymer solar cells from a poly(3-hexylthiophene)/[6,6]-phenyl C_{61}-butyric acidmethyl ester concentration graded bilayers, *Appl. Phys. Lett.* **95**, 043505 (2009).

[66] Kaur, M., Gopal, A., Davis, R. M. and Heflin, J. R. Concentration gradient P3OT/PCBM photovoltaic devices fabricated by thermal interdiffusion of separately spin-cast organic layers, *Sol. Energy Mater. & Solar Cells* **93**, 1779 (2009).

[67] Mor, G. K., Varghese, O. K., Paulose, M., Shankar, K. and Grimes, C. A. A review on highly ordered, vertically oriented TiO2 nanotube arrays: Fabrication, material properties, and solar energy applications, *Sol. Energy Mater. & Solar Cells* **90**, 2011 (2006).

[68] Gowrishankar, V., Miller, N., McGehee, M. D., Misner, M. J., Ryu, D. Y., Russell, T. P., Drockenmuller, E. and Hawker, C. J. Fabrication of densely packed, well-ordered, high-aspect-ratio silicon nanopillars over large areas using block copolymer lithography, *Thin Solid Films* **513**, 289 (2006).

[69] Coakley, K. M. and McGehee, M. D. Photovoltaic cells made from conjugated polymers infiltrated into mesoporous titania, *Appl. Phys. Lett.* **83**, 3380 (2003).

[70] Kuo, C. Y., Tang, W. C., Gau, C., Guo, T. F. and Jeng, D. Z. Ordered bulk heterojunction solar cells with vertically aligned TiO[sub 2] nanorods embedded in a conjugated polymer, *Appl. Phys. Lett.* **93**, 033307 (2008).

[71] Yodyingyong, S., Zhou, X., Zhang, Q., Triampo, D., Xi, J., Park, K., Limketkai, B. and Cao, G. Enhanced Photovoltaic Performance of Nanostructured Hybrid Solar Cell Using Highly Oriented TiO2 Nanotubes, *The J. of Phys. Chem. C* **114**, 21851 (2010).

[72] Chang, C.-H., Huang, T.-K., Lin, Y.-T., Lin, Y.-Y., Chen, C.-W., Chu, T.-H. and Su, W.-F. Improved charge separation and transport efficiency in poly(3-hexylthiophene)-TiO2 nanorod bulk heterojunction solar cells, *J. Mater. Chem.* **18**, 2201–2207 (2008).

[73] Kim, J. Y., Kim, S. H., Lee, H.-H., Lee, K., Ma, W., Gong, X. and Heeger, A. J. New Architecture for High-Efficiency Polymer Photovoltaic Cells Using

Solution-Based Titanium Oxide as an Optical Spacer, *Adv. Mater.* **18**, 572 (2006).

[74] Lee, K., Kim, J. Y., Park, S. H., Kim, S. H., Cho, S. and Heeger, A. J. Air-Stable Polymer Electronic Devices, *Adv. Mater.* **19**, 2445 (2007).

[75] Campoy-Quiles, M., Ferenczi, T., Agostinelli, T., Etchegoin, P. G., Kim, Y., Anthopoulos, T. D., Stavrinou, P. N., Bradley, D. D. C. and Nelson, J. Morphology evolution via self-organization and lateral and vertical diffusion in polymer:fullerene solar cell blends, *Nature Mater.* **7**, 158 (2008).

[76] Peet, J., Kim, J. Y., Coates, N. E., Ma, W. L., Moses, D., Heeeger, A. J. and Bazana, G. C. Efficiency enhancement in low-bandgap polymer solar cells by processing with alkane dithiols, *Nature Mater.* **6**, 497 (2007).

[77] Wienk, M. M., Struijk, M. P. and Janssen, R. A. J. Low band gap polymer bulk heterojunction solar cells, *Chem. Phys. Lett.* **422**, 488 (2006).

[78] Hou, J., Chen, H.-Y., Zhang, S., Chen, R. I., Yang, Y., Wu, Y. and Li, G. Synthesis of a Low Band Gap Polymer and Its Application in Highly Efficient Polymer Solar Cells, *J. of the Am. Chem. Soc.* **131**(43), 15586 (2009).

[79] Forberich, K., Dennler, G., Scharber, M. C., Hingerl, K., Fromherz, T. and Brabec, C. J. Performance improvement of organic solar cells with moth eye anti-reflection coating, *Thin Solid Films* **516**, 7167 (2008).

[80] Luk, W. C., Yeung, K. M., Tam, K. C., Ng, K. L., Kwok, K. C., Kwong, C. Y., Ng, A. M. C. and Djurisic, A. B. Enhanced conversion efficiency of polymeric photovoltaic cell by nanostructured antireflection coating, *Organic Electronics* **12**, 557 (2011).

[81] Zhou, W., Tao, M., Chen, L. and Yang, H. Microstructured surface design for omnidirectional antireflection coatings on solar cells, *J. of Appl. Phys.* **102**, 103105 (2007).

[82] Zimmermann, B., Glatthaar, M., Niggemann, M., Riede, K. M., Ziegler, T. and Gombert, A. Organic solar cells with inverted layer sequence incorporating optical spacers - simulation and experiment. volume 6197, 61970G. SPIE, (2006).

[83] Andersen, P. D., Skrhj, J. C., Andreasen, J. W. and Krebs, F. C. Investigation of optical spacer layers from solution based precursors for polymer solar cells using X-ray reflectometry, *Opt. Mater.* **31**, 1007 (2009).

[84] Datta, D., Iyer, S. S. K. and Kumar, S. Role of exciton blocking layers as optical spacer in CuPc/C60 based organic solar cells. in *Photovoltaic Specialists Conference (PVSC), 2010 35th IEEE*, 000508, (2010).

[85] Min, C., Li, J., Veronis, G., Lee, J.-Y., Fan, S. and Peumans, P. Enhancement of optical absorption in thin-film organic solar cells through the excitation of plasmonic modes in metallic gratings, *Appl. Phys. Lett.* **96**, 133302 (2010).

[86] Diukman, I., Tzabari, L., Berkovitch, N., Tessler, N. and Orenstein, M. Controlling absorption enhancement in organic photovoltaic cells by patterning Au nano disks within the active layer, *Opt. Express* **19**, A64 (2011).

[87] Abass, A., Shen, H., Bienstman, P. and Maes, B. Angle insensitive enhancement of organic solar cells using metallic gratings, *J. of Appl. Phys.* **109**, 023111 (2011).

[88] Shaw, P., Ruseckas, A. and Samuel, I. Exciton diffusion Measurements in Poly(3-hexylthiophene), *Adv. Mater.* **20**, 3516 (2008).

[89] Gupta, D., Bag, M. and Narayan, K. S. Correlating reduced fill factor in polymer solar cells to contact effects, *Appl. Phys. Lett.* **92**, 093301 (2008).

[90] Mihailetchi, V. D., Van Duren, J. K. J., Blom, P. W. M., Hummelen, J. C., Janssen, R. A. J., Kroon, J. M., Rispens, M. T., Verhees, W. J. H. and Wienk, M. M. Electron transport in a methanofullerene, *Adv. Funct. Mater.* **13**, 43 (2003).

[91] Blom, P. W. M., de Jong, M. J. M. and van Munster, M. G. Electric-field and temperature dependence of the hole mobility in poly(p-phenylene vinylene), *Phys. Rev. B* **55**, R656 (1997).

[92] Geens, W., Shaheen, S. E., Brabec, C. J., Poortmans, J. and Sariciftci, N. S. Field-effect mobility measurements of conjugated polymer/fullerene photovoltaic blends. volume 544, 516, (2000).

[93] Tanase, C., Meijer, E. J., Blom, P. W. M. and de Leeuw, D. M. Unification of the Hole Transport in Polymeric Field-Effect Transistors and Light-Emitting Diodes, *Phys. Rev. Lett.* **91**, 216601 (2003).

[94] Melzer, C., Koop, E. J., Mihailetchi, V. D. and Blom, P. W. M. Hole transport in poly(phenylene vinylene)/methanofullerene bulk-heterojunction solar cells, *Adv. Funct. Mater.* **14**, 865 (2004).

[95] Frohne, H., Shaheen, S. E., Brabec, C. J., Muller, D. C., Sariciftci, N. S. and Meerholz, K. Influence of the anodic work function on the performance of organic solar cells, *Chem. Phys. Chem.* **3**, 795 (2002).

[96] Brabec, C. J., Cravino, A., Meissner, D., Serdar Sariciftci, N., Fromherz, T., Rispens, M. T., Sanchez, L. and Hummelen, J. C. Origin of the open circuit voltage of plastic solar cells, *Adv. Funt. Mater.* **11**, 374 (2001).

[97] Yan, H., Chen, Z., Zheng, Y., Newman, C., Quinn, J. R., Dötz, F., Kastler, M. and Facchetti, A. A high-mobility electron-transporting polymer for printed transistors, *Nature* **457**, 679 (2009).

[98] Cunningham, P. D. and Hayden, L. M. Carrier Dynamics Resulting from Above and Below Gap Excitation of P3HT and P3HT/PCBM Investigated by Optical-Pump Terahertz-Probe Spectroscopy, *The J. of Phys. Chem. C* **112**, 7928 (2008).

[99] Ukai, S., Ito, H., Marumoto, K. and Kuroda, S. Electrical Conduction of Regioregular and Regiorandom Poly(3-hexylthiophene) Doped with Iodine, *J. of the Phys. Society of Japan* **74**, 3314 (2005).

[100] Prosa, T. J., Winokur, M. J., Moulton, J., Smith, P. and Heeger, A. J. X-ray structural studies of poly(3-alkylthiophenes): An example of an inverse comb, *Macromolecules* **25**, 4364 (1992).

[101] Kline, J. R., McGehee, M. D. and Toney, M. F. Highly oriented crystals at the buried interface in polythiophene thin-film transistors, *Nature Mater.* **5**, 222 (2006).

[102] Brinkmann, M. and Rannou, P. Effect of Molecular Weight on the Structure and Morphology of Oriented Thin Films of Regioregular Poly(3-hexylthiophene) Grown by Directional Epitaxial Solidification, *Adv.Funct. Mater.* **17**, 101 (2007).

[103] Mühlbacher, D., Scharber, M., Morana, M., Zhu, Z., Waller, D., Gaudiana, R. and Brabec, C. High Photovoltaic Performance of a Low-Bandgap Polymer, *Adv. Mater.* **18**, 2884 (2006).

[104] Blouin, N., Michaud, A. and Leclerc, M. A Low-Bandgap Poly(2,7-Carbazole) Derivative for Use in High-Performance Solar Cells, *Adv. Mater.* **19**, 2295 (2007).

[105] Manca, J. V., Munters, T., Martens, T., Beelen, Z., Goris, L., D'Haen, J., D'Olieslaeger, M., Lutsen, L., Vanderzande, D., Schepper, L. D., Haenen, K., Nesladek, M., Geens, W., Poortmans, J. and Andriessen, R. State-of-the-art MDMO-PPV:PCBM bulk heterojunction organic solar cells: materials, nanomorphology, and electro-optical properties. volume 4801, 15. SPIE, (2003).

[106] Deng, X., Zheng, L., Yang, C., Li, Y., Yu, G. and Cao, Y. Polymer Photovoltaic Devices Fabricated with Blend MEHPPV and Organic Small Molecules, *The J. of Phys. Chem. B* **108**, 3451 (2004).

[107] Ramsdale, C. M. and Greenham, N. C. The optical constants of emitter and electrode materials in polymer light-emitting diodes, *J. Phys. D: Appl. Phys.* **36**, L29 (2003).

[108] Kim, Y., Cook, S., Choulis, S. A., Nelson, J., Durrant, J. R. and Bradley, D. D. C. Organic Photovoltaic Devices Based on Blends of Regioregular Poly(3-hexylthiophene) and Poly(9,9-dioctylfluorene-co-benzothiadiazole), *Chemistry of Mater.* **16**(23), 4812 (2004).

[109] López, A. M., Mateo-Alonso, A. and Prato, M. Materials chemistry of fullerene C60 derivatives, *J. Mater. Chem.* **21**, 1305 (2011).

[110] Cook, S., Ohkita, H., Kim, Y., Benson-Smith, J. J., Bradley, D. D. C. and Durrant, J. R. A photophysical study of PCBM thin films, *Chem. Phys. Lett.* **445**, 276 (2007).

[111] Boland, P., Lee, K. and Namkoong, G. Device optimization in PCPDTBT:PCBM plastic solar cells, *Sol. Energy Mater. & Solar Cells* **94**, 915 (2010).

[112] Caironi, M., Newman, C., Moore, J. R., Natali, D., Yan, H., Facchetti, A. and Sirringhaus, H. Efficient charge injection from a high work function metal in high mobility n-type polymer field-effect transistors, *Appl. Phys. Lett.* **96**, 183303 (2010).

[113] Szendrei, K., Jarzab, D., Chen, Z., Facchetti, A. and Loi, M. A. Ambipolar all-polymer bulk heterojunction field-effect transistors, *J. Mater. Chem.* **20**, 1317 (2010).

[114] Klein, A., Körber, C., Wachau, A., Säuberlich, F., Gassenbauer, Y., Harvey, S. P., Proffit, D. E. and Mason, T. O. Transparent Conducting Oxides for Photovoltaics: Manipulation of Fermi Level, Work Function and Energy Band Alignment, *Materials* **3**, 4892 (2010).

[115] Delahoy, A. E. and Guo, S. *Transparent Conducting Oxides for Photovoltaics*, 716. John Wiley & Sons, Ltd (2010).

[116] Wager, J. F. Transparent Electronics, *Science* **300**, 1245 (2003).

[117] Salaneck, W. R.and Lüglund, M., Fahlmann, M., Greczynski, G. and Kugler, T. The electronic structure of polymer-metal interfaces studied by ultraviolet photoelectron spectroscopy, *Mater. Sci. Eng. R* **34**, 121 (2001).

[118] Ishii, H., Sugiyama, K., Ito, E. and Seki, K. Energy Level Alignment and Interfacial Electronic Structures at Organic/Metal and Organic/Organic Interfaces, *Adv. Mater.* **11**, 605 (1999).

[119] Kim, S. Y., Lee, J.-L., Kim, K.-B. and Tak, Y.-H. Effect of ultraviolet–ozone treatment of indium–tin–oxide on electrical properties of organic light emitting diodes, *J. of Appl. Phys.* **95**, 2560 (2004).

[120] T., H., Zhang, F., Xu, Z., Zhao, S., Yue, X. and Yuan, G. Effect of UV-ozone treatment on ITO and post-annealing on the performance of organic solar cells, *Synthetic Metals* **159**, 754 (2009).

[121] Groenendaal, L., Jonas, F., Freitag, D., Pielartzik, H. and Reynolds, J. R. Poly(3,4-ethylenedioxythiophene) and its derivatives: past, present, and future, *Adv. Mater.* **12**, 481 (2000).

[122] Louwet, F., Groenendaal, L., Dhaen, J., Manca, J., Van Luppen, J., Verdonck, E. and Leenders, L. PEDOT/PSS: Synthesis, characterization, properties and applications, *Synthetic Metals* **135**, 115 (2003).

[123] Huang, J., Miller, P. F., Wilson, J. S., De Mello, A. J., De Mello, J. C. and Bradley, D. D. C. Investigation of the effects of doping and post-deposition treatments on the conductivity, morphology, and work function of poly(3,4-ethylenedioxythiophene)/poly(styrenesulfonate) films, *Adv. Funct. Mater.* **15**, 290 (2005).

[124] Kim, J. S., Granström, M., Friend, R. H., Johansson, N., Salaneck, W. R., Daik, R., Feast, W. J. and Cacialli, F. Indium-tin oxide treatments for single- and double-layer polymeric light-emitting diodes: The relation between the

anode physical, chemical, and morphological properties and the device performance, *J. of App. Phys.* **84**, 6859 (1998).

[125] Kim, J.-H., Huh, S.-Y., Kim, T.-i. and Lee, H. H. Thin pentacene interlayer for polymer bulk-heterojunction solar cell, *Appl. Phys. Lett.* **93**, 143305 (2008).

[126] Reinhard, M., Hanisch, J., Zhang, Z., Ahlswede, E., Colsmann, A. and Lemmer, U. Inverted organic solar cells comprising a solution-processed cesium fluoride interlayer, *Appl. Phys. Lett.* **98**, 053303 (2011).

[127] Oheda, H. Phase-shift analysis of modulated photocurrent: Its application to the determination of the energetic distribution of gap states, *J. of Appl. Phys.* **52**, 6693 (1981).

[128] Kounavis, P. Analysis of the modulated photocurrent experiment, *Phys. Rev. B* **64**, 045204 (2001).

[129] F-Santiago, F., Bisquert, J., Palomeres, E., Haque, S. A. and Durrant, J. R. Impedance spectroscopy study of dye-sensitized solar cells with undoped spiro-OMeTAD as hole conductor, *J. of Appl. Phys.* **100**, 034510 (2006).

[130] Schlichthörl, G., Huang, S. Y., Sprague, J. and Frank, A. J. Band Edge Movement and Recombination Kinetics in Dye-Sensitized Nanocrystalline TiO_2 Solar Cells: A Study by Intensity Modulated Photovoltage Spectroscopy, *J. Phys. Chem. B* **101**, 8141 (1997).

[131] Vanmaekelberghet, D., van de Lagemaat, J. and Schropp, R. E. I. Observation and explanation of quantum efficiencies exceeding unity in amorphous silicon solar cells, *Sol. Energy Mater. & Solar Cells* **41-42**, 537 (1996).

[132] Mora-Seró, I., Luo, Y. Garcia-Belmontea, G., Bisquerta, J., Muñoz, D., Vozb, C., Puigdollersb, J. and Alcubillab, R. Recombination rates in heterojunction silicon solar cells analyzed by impedance spectroscopy at forward bias and under illumination, *Sol. Energy Mater. & Solar Cells* **92**, 505 (2008).

[133] Orestein, J. and Kastner, M. Photocurrent Transient Spectroscopy: Measurement of the Density of Localized States in a -As_2Se_3, *Phys. Rev. Lett.* **46**, 1421 (1981).

[134] Agostinelli, T., Caironi, M.and Natali, D., Sampietro, M., Arca, M., Devillanova, F. and Ferrero, V. Trapping effects on the frequency response of dithiolene-based planar photodetectors, *Synthetic Metals* **157**, 984 (2007).

[135] Zeng, W., Wu, H., Zhang, C., Huang, F., Peng, J., Yang, W. and Cho, Y. Polymer light-emitting diods with cathodes printed from conducting Ag paste, *Adv. Mater.* **19**, 810 (2007).

[136] Clarke, T. M., Jamieson, F. C. and Durrant, J. R. Transient Absorption Studies of Bimolecular Recombination Dynamics in Polythiophene/Fullerene Blend Films, *J. Phys. Chem. C* **113**, 20934 (2009).

[137] McNeill, C. R., Abrusci, A., Hwang, I., Ruderer, M. A. and Mller-Buschbaum, P. a, n. G. N. C. Photophysics and Photocurrent Generation in Polythiophene/Polyfluorene Copolymer Blends, *Adv. Funct. Mater.* **19**, 3103 (2009).

[138] Ma, W., Yang, C., Gong, X., Lee, K. and Heeger, A. J. Thermally Stable, Efficient Polymer Solar Cells with Nanoscale Control of the Interpenetrating Network Morphology, *Adv. Funct. Mater.* **15**, 1617 (2005).

[139] van Bavel, S. S., Sourty, E., de With, G. and Loos, J. Three-Dimensional Nanoscale Organization of Bulk Heterojunction Polymer Solar Cells, *Nano Lett.* **9**, 507 (2009).

[140] Sariciftci, N. S., Smilowitz, L., Heeger, A. J. and Wudl, F. Photoinduced Electron Transfer from a Conducting Polymer to Buckminsterfullerene, *Science* **258**, 1474 (1992).

[141] Cremer, J., Baüerle, P., Wienk, M. M. and Janssen, A. J. R. High Open-Circuit Voltage Poly(ethynylene bithienylene):Fullerene Solar Cells, *Chem. Mater.* **18**, 5832 (2006).

[142] Cook, S., Katoh, R. and Furube, A. Ultrafast Studies of Charge Generation in PCBM:P3HT Blend Films following Excitation of the Fullerene PCBM, *The J. of Phys. Chem. C* **113**, 2547 (2009).

[143] Westerling, M., Vijila, C., Österbacka, R. and Stubb, H. Optical studies of excited-state relaxation in poly(9,9-dihexylfluorene-co-benzothiadiazole), *Phys. Rev. B* **67**, 195201 (2003).

[144] Westerling, M., Vijila, C., Österbacka, R. and Stubb, H. Bimolecular recombination in regiorandom poly(3-hexylthiophene), *Chem. Phys.* **286**, 315 (2003).

[145] Epshtein, O., Eichen, Y., Ehrenfreund, E., Wohlgenannt, M. and Vardeny, Z. V. Linear and Nonlinear Photoexcitation Dynamics in π-Conjugated Polymers, *Phys. Rev. Lett.* **90**, 046804 (2003).

[146] Mazhari, B. An improved solar cell circuit model for organic solar cells, *Sol. Energy Mater. & Solar Cells* **90**, 1021 (2006).

[147] Yoo, S., Domercq, B. and Kippelen, B. Intensity-dependent equivalent circuit parameters of organic solar cells based on pentacene and C_{60}, *J. Appl. Phys.* **97**, 103706 (2005).

[148] Bruder, F. and Brenn, R. Spinodal decomposition in thin films of a polymer blend, *Phys. Rev. Lett.* **69**, 624 (1992).

[149] Fabregat-Santiago, F., Garcia-Belmonte, G., Mora-Sero, I. and Bisquert, J. Characterization of nanostructured hybrid and organic solar cells by impedance spectroscopy, *Phys. Chem. Chem. Phys.* (2011).

[150] Han, L., Koide, N., Chiba, Y. and Mitate, T. Modeling of an equivalent circuit for dye-sensitized solar cells, *Appl. Phys. Lett.* **84**, 2433 (2004).

[151] Kuwabara, T., Kawahara, Y., Yamaguchi, T. and Takahashi, K. Characterization of Inverted-Type Organic Solar Cells with a ZnO Layer as the Electron Collection Electrode by ac Impedance Spectroscopy, *ACS Appl. Mater. & Interfaces* **1**, 2107 (2009).

[152] Jaiswal, M. and Menon, R. Equivalent circuit for an organic field-effect transistor from impedance measurements under dc bias, *Appl. Phys. Lett.* **88**, 123504 (2006).

[153] Hsiao, C.-C., Hsiao, A.-E. and Chen, S.-A. Design of Hole Blocking Layer with Electron Transport Channels for High Performance Polymer Light-Emitting Diodes, *Adv. Mater.* **20**, 1982 (2008).

[154] Glatthaar, M., Mingirulli, N., Zimmermann, B., Ziegler, T., Kern, R., Niggemann, M., Hinsch, A. and Gombert, A. Impedance spectroscopy on organic bulk-heterojunction solar cells, *phys. status solidi (a)* **202**, R125 (2005).

[155] Garcia-Belmonte, G., Munar, A., Barea, E. M., Bisquert, J., Ugarte, I. and Pacios, R. Charge carrier mobility and lifetime of organic bulk heterojunctions analyzed by impedance spectroscopy, *Organic Electronics* **9**(5), 847 (2008).

[156] Gross, B. On the Theory of Dielectric Loss, *Phys. Rev.* **59**, 748 (1941).

[157] Bisquert, J., Garcia-Belmonte, G., Munar, A., Sessolo, M., Soriano, A. and Bolink, H. J. Band unpinning and photovoltaic model for P3HT:PCBM organic bulk heterojunctions under illumination, *Chem. Phys. Lett.* **465**, 57 (2008).

[158] Bisquert, J. Beyond the quasistatic approximation: Impedance and capacitance of an exponential distribution of traps, *Phys. Rev. B* **77**, 235203 (2008).

[159] Jones, B. K. Low-Frequency Noise Spectroscopy, *IEEE Trans. on Electon Devices* **41**, 2188 (1994).

[160] Jones, B. K. Electrical noise as a mesure of quality and reliability in electronic devices, *Advances in Electronics and Electron Physics* **87**, 201 (1993).

[161] Vandamme, L. Noise as a diagnostic tool for quality and reliability of electronic devices, *Electron Devices, IEEE Transactions on* **41**, 2176 (1994).

[162] Balandin, A., Wang, K. L., Seizhenko, A. and Baddyopadhyay, S. The Fundametal 1/f Noise and the Hooge Parameter in Semiconductor Quantum Wires, *IEEE Trans. on Electon Devices* **46**, 1240 (1999).

[163] Ke, L., Li, W. and Chau, S. J. 1/f Noise analysis of ZnO nanowire and thin film, *2nd IEEE International Nanoelectronic Conference* **INEC 2008**, 1133 (2008).

[164] Deen, M. J., Marinov, O., Yu, J., Holdcroft, S. and Woods, W. Low-Frequency Noise in Polymer Transistor, *IEEE Trans. on Electon Devices* **48**, 1688 (2001).

[165] Hung, K. K., Ko, P. K., Hu, C. and Cheng, Y. C. A unified model for the flicker noise in metal-oxide-semiconductor field-effect transistors, *Electron Devices, IEEE Transactions on* **37**, 654 (1990).

[166] Vandamme, L. K. J., Alabedra, R. and Zommiti, M. 1/f noise as a reliability estimation for solar cells, *Solid-State Electronics* **26**, 671 (1983).

[167] Galante, N. and Tagliaferro, A. Photoinduced current noise in a-Si:H solar cells, *Il Nuovo Cimento D* **13**, 795 (1991).

[168] Jayaweera, P. V. V., Perera, A. G. U. and Tennakone, K. Why Gratzels cell works so well, *Inorganica Chimica Acta* **361**, 707 (2008).

[169] Norrman, K., Gevorgyan, S. A. and Krebs, F. C. Water-Induced Degradation of Polymer Solar Cells Studied by $H_2^{18}O$ Labeling, *ACS Appl. Mater. & Interfaces* **1**, 102 (2009).

[170] Jørgensen, M., Norrman, K. and Krebs, F. C. Stability/degradation of polymer solar cells, *Sol. Energy Mater. & Solar Cells* **92**, 686 (2008).

[171] Neugebauer, H., Brabec, C. J., Hummelen, J. C. and Sariciftci, N. S. Stability and photodegradation mechanisms of conjugated polymer/fullerene plastic solar cells, *Sol. Energy Mater. & Solar Cells* **61**, 35 (2000).

[172] Nyquist, H. Thermal Agitation of Electric Charge in Conductors, *Phys. Rev.* **32**, 110 (1928).

[173] Novikov, S. V., Dunlap, D. H., Kenkre, V. M., Parris, P. E. and Vannikov, A. V. Essential Role of Correlations in Governing Charge Transport in Disordered Organic Materials, *Phys. Rev. Lett.* **81**, 4472 (1998).

[174] Movaghar, B., Grünewald, M., Ries, B., Bässler, H. and Würtz, D. Diffusion and relaxation of energy in disordered organic and inorganic materials, *Phys. Rev. B* **33**, 5545–5554 (1986).

[175] Atwani, O., Baristiran, C., Erden, A. and Sonmez, G. A stable, low band gap electroactive polymer: Poly(4,7-dithien-2-yl-2,1,3-benzothiadiazole), *Synthetic Metals* **158**, 83 (2008).

[176] Fu, C., Liao, J., Luo, W., Li, R. and Chen, X. Emission of 1.53 μm originating from the lattice site of Er^{3+} ions incorporated in TiO_2 nanocrystals, *Opt. Lett.* **33**(9), 953 (2008).

[177] Ribeiro, S. J. L., Messaddeq, Y., Goncalves, R. R., Ferrari, M., Montagna, M. and Aegerter, M. A. Low optical loss planar waveguides prepared in an organic–inorganic hybrid system, *Appl. Phys. Lett.* **77**(22), 3502 (2000).

[178]

[179] Burroughes, J. H., Bradley, D. D. C., Brown, A. R., Marks, R. N., Mackay, K., Friend, R. H., Burns, P. L. and Holmes, A. B. Light-emiting diodes based on conjugated polymers, *Nature* **347**, 539 (1990).

[180] Braun, D. and Heeger, A. J. Visible light emission from semiconducting polymer diodes, *App. Phys. Lett.* **58**, 1982 (1991).

[181] Capelli, R., Toffanin, S., Generali, G., Usta, H., Facchetti, A. and Muccini, M. Organic light-emitting transistors with an efficiency that outperforms the equivalent light-emitting diodes, *Nature Mater.* .

[182] Feldmeier, E. J., Schidleja, M., Melzer, C. and von Seggern, H. A Color-Tuneable Organic Light-Emitting Transistor, *Adv. Mater.* **22**, 3568 (2010).

[183] Kozlov, V. G., Bulovic, V., Burrows, P. E. and Forrest, S. R. Laser action in organic semiconductor waveguide and double-heterostructure devices, *Nature* **389**, 362 (1997).

[184] Vannahme, C., Klinkhammer, S., Christiansen, M. B., Kolew, A., Kristensen, A., Lemmer, U. and Mappes, T. All-polymer organic semiconductor laser chips:?Parallel fabrication and encapsulation, *Opt. Express* **18**, 24881 (2010).

[185] Argyros, A., van Eijkelenborg, M. A., Large, M. C. and Bassett, I. M. Hollow-core microstructured polymer optical fiber, *Opt. Lett.* **31**, 172–174 (2006).

[186] Kuriki, K., Koike, Y. and Okamoto, Y. Plastic Optical Fiber Lasers and Amplifiers Containing Lanthanide Complexes, *Chem. Rev.* **102**, 2347 (2002).

[187] Schilinsky, P., Waldauf, C. and Brabec, C. J. Recombination and loss analysis in polythiophene based bulk heterojunction photodetectors, *Appl. Phys. Lett.* **81**, 3885 (2002).

[188] Chen, E.-C., Chang, C.-Y., Shieh, J.-T., Tseng, S.-R., Meng, H.-F., Hsu, C.-S. and Horng, S.-F. Polymer photodetector with voltage-adjustable photocurrent spectrum, *Appl. Phys. Lette.* **96**, 043507 (2010).

[189] Nalwa, K. S., Cai, Y., Thoeming, A. L., Shinar, J., Shinar, R. and Chaudhary, S. Polythiophene-Fullerene Based Photodetectors: Tuning of Spectral

Response and Application in Photoluminescence Based (Bio)Chemical Sensors, *Adv. Mater.* **22**, 4157 (2010).

[190] Gong, X., Tong, M., Xia, Y., Cai, W., Moon, J. S., Cao, Y., Yu, G., Shieh, C.-L., Nilsson, B. and Heeger, A. J. High-Detectivity Polymer Photodetectors with Spectral Response from 300 nm to 1450 nm, *Science* **325**, 1665 (2009).

[191] Schilinsky, P., Waldauf, C., Hauch, J. and Brabec, C. J. Polymer photovoltaic detectors: progress and recent developments, *Thin Solid Films* **451-452**, 105 (2004).

[192] Coates, N. E., Hwang, I.-W., Peet, J., Bazan, G. C., Moses, D. and Heeger, A. J. 1,8-octanedithiol as a processing additive for bulk heterojunction materials: Enhanced photoconductive response, *Appl. Phys. Lett.* **93**, 072105 (2008).

[193] McNeill, R. C., Hwang, I. and Greenham, N. C. Photocurrent transients in all-polymer solar cells: Trapping and detrapping effects, *J. of Appl. Phys.* **106**, 024507 (2009).

[194] Li, K., Shen, Y., Majumdar, N., Hu, C., Gupta, M. C. and Campbell, J. C. Determination of free polaron lifetime in organic bulk heterojunction solar cells by transient time analysis, *J. of Appl. Phys.* **108**, 084511 (2010).

[195] Garcia-Belmonte, G., Boix, P. P., Bisquert, J., Sessolo, M. and Bolink, H. J. Simultaneous determination of carrier lifetime and electron density-of-states in P3HT:PCBM organic solar cells under illumination by impedance spectroscopy, *Sol. Energy Mater. & Solar Cells* **94**, 366 (2010).

[196] Clarke, T. M., Ballantyne, A. M., Nelson, J., Bradley, D. D. C. and Durrant, J. R. Free Energy Control of Charge Photogeneration in Polythiophene/Fullerene Solar Cells: The Influence of Thermal Annealing on P3HT/PCBM Blends, *Adv. Funct. Mater.* **18**, 4029 (2008).

[197] Lee, J., Vandewal, K., Yost, S. R., Bahlke, M. E., Goris, L., Baldo, M. A., Manca, J. V. and Voorhis, T. V. Charge Transfer State Versus Hot Exciton Dissociation in PolymerFullerene Blended Solar Cells, *J. of the Am. Chem. Soc.* **132**, 11878 (2010).

[198] Mozer, A. J., Dennler, G., Sariciftci, N. S., Westerling, M., Pivrikas, A., Österbacka, R. and Juška, G. Time-dependent mobility and recombination of the photoinduced charge carriers in conjugated polymer/fullerene bulk heterojunction solar cells, *Phys. Rev. B* **72**, 035217 (2005).

[199] Shuttle, C. G., O'Regan, B., Ballantyne, A. M., Nelson, J., Bradley, D. D. C., de Mello, J. and Durrant, J. R. Experimental determination of the rate law for charge carrier decay in a polythiophene: Fullerene solar cell, *Appl. Phys. Lett.* **92**, 093311 (2008).

[200] Shuttle, C. G., Maurano, A., Hamilton, R., O'Regan, B., de Mello, J. C. and Durrant, J. R. Charge extraction analysis of charge carrier densities in a polythiophene/fullerene solar cell: Analysis of the origin of the device dark current, *Appl. Phys. Lett.* **93**, 183501 (2008).

[201] Ryu, M. S., Cha, H. J. and Jang, J. Improvement of operation lifetime for conjugated polymer:fullerene organic solar cells by introducing a UV absorbing film, *Sol. Energy Mater. & Solar Cells* **94**, 152 (2010).

[202] Youn, J. H., Lee, Y. I., Moon, H. T., Ryu, M. S., Kim, J. and Jang, J. Trap energy level of P3HT: PCBM-71 bulk heterojunction solar cells with PICTS (photo-induced current transient spectroscopy), *Current Appl. Phys.* **10**, S525 (2010).

[203] Marlor, G. A. Field Formulation of Rate Processes in Photoconductors, *Phys. Rev.* **159**, 540 (1967).

[204] Murayama, K., Nomura, Y. and Fujisaki, T. Hopping transport at localized band tail states in amorphous hydrogenated silicon, *physica status solidi (a)* **207**, 561 (2010).

[205] Chopra, K. L. and Bahl, S. K. Structural, Electrical, and Optical Properties of Amorphous Germanium Films, *Phys. Rev. B* **1**, 2545 (1970).

[206] Bourbie, D. Field-induced crossover from phonon to field assisted hopping conductivity in organic materials, *Appl. Phys. Lett.* **98**, 012104 (2011).

[207] Rubinger, R. M., Ribeiro, G. M., de Oliveira, A. G., Albuquerque, H. A., da Silva, R. L., Rubinger, C. P. L., Rodrigues, W. N. and Moreira, M. V. B. Temperature-dependent activation energy and variable range hopping in semi-insulating GaAs, *Semicond. Sci. Technol.* **21**, 1681 (2006).

[208] Jamieson, F. C., Agostinelli, T., Azimi, H., Nelson, J. and Durrant, J. R. Field-Independent Charge Photogeneration in PCPDTBT/PC70BM Solar Cells, *The J. of Phys. Chem. Lett.* **1**, 3306 (2010).

[209] Tonks, L. Theory of liquid surface rupture by a uniform electric field, *Phys. Rev.* **127**, 562 (1935).

[210] Arun, N., Sharma, A., Shenoy, B. and Narayan, K. S. Electric-field-controlled surface instability in soft elastic films, *Adv. Mater.* **18**, 660 (2006).

[211] Nevrovskii, V. A. and Rakhovskii, V. I. Electrode melting and metal-drop formation in high electric fields, *IEEE Trans. Electr. Insul.* **25**, 359 (1990).

[212] Zubarev, N. V. and Zubareva, O. V. Dynamics of the free surface of a conducting liquid in a near-critical electric field, *Tech. Phycs.* **46**, 806 (2001).

[213] Lin, J. L., Lee, G. B., Chang, Y. H. and Lien, K. Y. Model description of contact angles in electrowetting on dielectric layers, *Langmuir* **22**, 484 (2006).

[214] Young, T. N. An essay on the cohesion of fluids, *Phil. Trans. R. Soc.* **95**, 65 (1805).

[215] O'Bockris, J. and Reddy, A. K. N. *Modern electrochemistry: and introduction to an interdisciplinary area*. NY: Plenum, New York, (1973).

[216] Moon, H., Cho, S. K., Garrell, R. L. and Kimb, C. J. Low Voltage electrowetting-on-dielectric., *J. Appl. Phys.* **92**, 4080 (2002).

[217] Mogele, F. and Baret, J. Electrowetting from basic to applications, *J. Phys. Condens. Matter.* **17**, R705 (2005).

[218] Walker, S. W. and Shapiro, B. Modeling the fluid dynamics of electrowetting on dielectrics (EWOD), *J. Microelectromech. Syst.* **15**, 986 (2006).

[219] Park, J. U. High resolution electrohydrodynamic jet printing, *Nature Mater.* **6**, 782 (2007).

[220] Landau, L., Lifshitz, E. M. and Pitaevskii, L. P. *Electrodynamics of continuous media*. Pergamon Press, Oxford, (1984).

[221] Zubarev, N. V. Exact solution for the steady state surface profile of the liquid metal in an external electric field, *Tech. Phys. Lett.* **25**, 920 (1999).

[222] Vilan, A. and Cahen, D. area-tunable micromirror based on electrowetting actuation of liquid-metal droplets, *Appl. Phys. Lett.* **89**, 201107 (2006).

[223] Choi, J., Lee, K. and Janes, D. B. Nanometer scale gap made by conventional microscale fabrication: step junction, *Nano Lett.* **4**, 1699 (2004).

[224] Forrest, S. R. The path to ubiquitous and low cost organic electronic appliances on plastic, *Nature* **428**, 911 (2004).

Addendum

List of corrections

- Equation 5.3 is taken from the reference 209.
- Equation 5.7 is taken from the reference 220, page 27.
- Equation 5.8, 5.9, 5.10 are derived by the author.
- Page 53, Table 2.1, unit of a is time (in second)
- Page 114, T should be replaced by γ.
- Page 116, Fig 5.2, θ should be replaced by θ_0.